Universidade de Lisboa
Faculdade de Ciências
Departamento de Física

Study of the jet trigger in p+Pb collisions with the ATLAS detector

Alexandre Nuno Pereira Lopes

Dissertação de Mestrado
Mestrado em Física
Física Nulcear e Partículas

2014

Universidade de Lisboa
Faculdade de Ciências
Departamento de Física

Study of the jet trigger in p+Pb collisions with the ATLAS detector

Alexandre Nuno Pereira Lopes

Dissertação de Mestrado
Mestrado em Física
Física Nuclear e Partículas

Dissertação orientada por Professora Doutora Amélia Maio
Co-orientada por Doutora Helena Santos

2014

Non puoi insegnare qualcosa ad un uomo.
Lo puoi solo aiutare a scoprirla dentro di sé.
Galileo Galilei

Abstract

p+Pb collisions are a crucial component for understanding phenomena in ultra-relativistic Pb+Pb collisions. That kind of collisions can provide baseline measurements which are essential to the understanding of final state phenomena produced in the hot and dense medium of the quark gluon plasma, such as jet quenching.

ATLAS is one of the particle physics detectors at the LHC and was used to record these type of asymmetric collisions. The ATLAS Trigger and Data Acquisition is the main component in selecting interesting events to record for posterior analysis. In this dissertation the ATLAS Jet Trigger system is studied in p+Pb collisions at $\sqrt{s_{NN}} = 5.02$ TeV. The results utilize data collected by ATLAS detector during the 2013 p+Pb run, corresponding to a total integrated luminosity of 30 nb^{-1}.

The results are obtained using fully reconstructed jets with the anti-k_T algorithm with per-event background subtraction procedure. The jet trigger dependence on centrality, pseudorapidity and transverse energy of the jet are studied. It is observed that, despite the centrality class of the collision, the trigger is efficient and robust in selecting the required objects.

Resumo

Colisões protão-chumbo constituem uma componente crucial para o estudo de fenómenos que ocorrem em colisões ultra-relativistas de chumbo-chumbo. Aquele tipo de colisões permite realizar medidas de referência para a compreensão de fenómenos produzidos no meio quente e denso do plasma de quarks e gluões, tais como a supressão jactos.

ATLAS é um dos detectores de física de partículas no LHC e foi usado para gravar dados deste tipo de colisões assimétricas. O trigger e o sistema de aquisição de dados de ATLAS são o principal componente na selecção de eventos para posterior análise. Nesta dissertacção o trigger de jactos de ATLAS é estudado num ambiente de colisões p+Pb a $\sqrt{s_{NN}} = 5.02$ TeV. Os resultados aqui apresentados utilizam dados colectados pelo detector ATLAS no LHC e correspondem a uma luminosidade integrada total de 30 nb^{-1}.

Os resultados são obtidos usando jactos totalmente reconstruídos pelo algoritmo anti-k_T com subtracção de fundo em cada evento. É estudado o desempenho do trigger e a sua dependência na centralidade da colisão e energia transversa e pseudorapidez do jacto. Observa-se que o sistema de trigger de jactos em colisões p+Pb, independentemnte da centralidade da colisão, é robusto e eficiente a seleccionar os objectos que são requeridos.

Contents

List of Figures

List of Tables

Introduction

The subject of this dissertation is on the performance of the ATLAS Jet Trigger system in a proton-nucleus collision environment. The importance of a p+A program at the Large Hadron Collider (LHC) is strictly related to the Heavy Ion program. It provides baseline measurements for Pb+Pb collisions, being essential to explain and interpret some of the results. The proton-nucleus collisions offers also very interesting investigations in several domains of High Energy Particle Physics, such as the saturation of the parton density function at low Bjorken-x.

The p+Pb inelastic cross section at $\sqrt{s_{NN}} = 5.02$ TeV was estimated to be 2 Barns. The LHC would provide a maximum instantaneous luminosity of 4.5×10^{27} $\mathrm{cm}^{-2}\mathrm{s}^{-1}$, which corresponds to an event rate of $\mathrm{O}(10^4)$ Hz. The trigger and data acquisition system is crucial in order to reduce the event rate to $\mathrm{O}(10^2)$ Hz for storage. This system has to be efficient in rejecting background events and at the same time select those interesting and rare events which will allow the study of physics of these asymmetric collisions.

In the first chapter is given a physics overview of the Standard Model of particle physics along with the hadron-hadron collision processes that are intrinsic to the production of jets. Some nucleus-nucleus collisions observables and results are also outlined in this chapter. Chapter 2 describes the experimental setup of the LHC and presents an overview of the ATLAS detector with special emphasis on the calorimeter. In chapter 3 the trigger and data acquisition systems are discussed in general and with some detail the jet trigger system along the three different trigger stages: Level 1, Level 2 and the Event Filter. Chapter 4 describes the analysis of the performance of the jet trigger system in p+Pb collisions. A summary is given at the end of the dissertation with the most significant results. The kinematical variables used in this dissertation are defined in Appendix A.

Chapter 1

Physics at the LHC

1.1 The Standard Model of Particle Physics

The Standard Model of Particle Physics (SM) describes matter with the most elementary particles and explains how they interact among them. It characterizes the strong, electromagnetic and weak interactions between those particles at that fundamental level. The theory of gravity is not described by the SM.

The Standard Model classifies the fundamental particles of matter in groups of one-half spin fermions and integer spin bosons. With a total of 12 fermions categorised further into two groups of six particles, called leptons and quarks, the ordinary matter is described. These two groups are separated based on the electric charges and the forces through which they interact with each other. Fig. 1.1 represents these fundamental particles along with the bosons that mediate the interactions between them in the Standard Model framework. One can divide this table into three generations of fermions. The first column corresponds to the particles of the first generation. The second generation is shown in the column two and the third in column three. Protons and neutrons are made of particles from the first generation. The other generations of elementary particles compose other kind of particles with a relatively short-life span. As to why there are three generations of particles, no one knows the answer. Each of this 12 fermions have an opposite partner with equal mass which are the respective anti-particles. These anti-particles defer from their partners in all the quantum numbers, with exception for the spin, being the opposite of its partner.

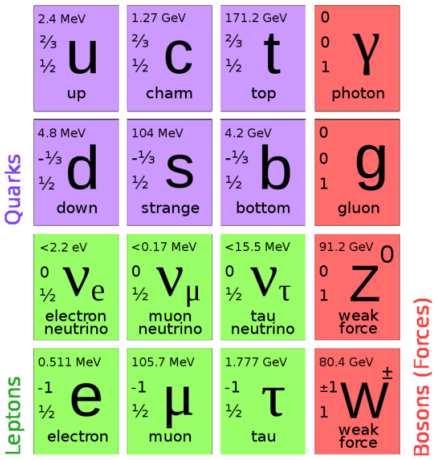

FIGURE 1.1: List of fermions and the respective bosons which mediate the interactions between them.

The gauge bosons are shown in the fourth column and are the mediators of the three forces. The photon is the mediator of the electromagnetic force and mediates the interaction of particles with electric charge. The Z and the W bosons are the mediators of the weak force through which one can explain the decay of all the short-lived particles. The gluon is the particle that mediates the strong interactions between particles that carry colour charge. The interaction range varies from each of the three forces. The electromagnetic force has infinitum range, while the other two forces have their interaction range smaller than 10^{-15} m. The gluon is the only boson of the mediators which can interact, not only with quarks, but specially with other gluons. Hadrons are composed of partons (quarks and gluons). Bound states of three quarks form baryons, such as the proton or the neutron, while combinations of a quark and an anti-quark yield meson particles, such as pions. While leptons carry integral electric charges, quarks carry fractional charges.

Colour confinement prevents the detection of single isolated quarks and gluons in nature. When a quark is ejected from a hadron in a high energy collision, the energy of the gluon connecting the two particles increases to the point where it breaks and spontaneously creates a quark-antiquark pair. The new emitted hadron then may radiate gluons, creating a collimated spray of particles commonly referred to as a jet.

In hadron-hadron collision two interaction types can be distinguished, soft and hard interactions. A soft interaction happens when the scatter between the two

hadrons results on two outgoing particles with low transverse momentum[1] and with a small deviation angle. On the other hand, a hard scattering event is a process which probes very short distances within the hadrons. In this process partons are scattered at wide angles after passing very close to each other, and two or more high transverse momentum outgoing partons are produced. These partons hadronize and are observed as jets in the detector. Fig. 1.2 represents a typical hard scattering interaction between two incoming partons. Other soft interactions also play a role in the collision. The incoming partons may start of a sequence of branching (a process similar to Bremsstrahlung), which produces an initial state radiation shower. This branching also can happen after the hard scattering thus producing final state radiation. The partons not involved in the hard interaction scatter with small angles respectively with small transverse momentum. These partons are associated to the underlying event. Multiple interactions can contribute to the underlying event, usually this is identified as *pile-up* which is a feature that happens when two or more collisions happen in the same event. Minimum bias events are characterized by having only soft scattering collisions, thus producing only low transverse momentum particles.

The clear understanding of the soft processes is important for the correct measurement of the high transverse momentum hard scattering partons. The presence of the soft interactions and final hadronization of all colour connected constituents of the events, prevent us from observing a direct and exact measurement of the transverse momentum of the outgoing partons from the hard scatter. What is accessible for measurement is a collimated spray of particles, the jet, along with the collision background.[2]

1.2 Heavy Ion collisions

The goal of colliding heavy nuclei at the LHC is to recreate the state of matter that is thought to have happened a few microseconds after the Big Bang. At this time, the temperature of the Universe was so large that quarks and gluons moved freely in a state of matter called Quark Gluon Plasma(QGP). As the Universe cooled down, the quarks and gluons became bound to the nucleons by the strong

[1] Transverse momentum is the particle's momentum relative to the transverse plane of the collision's axis.

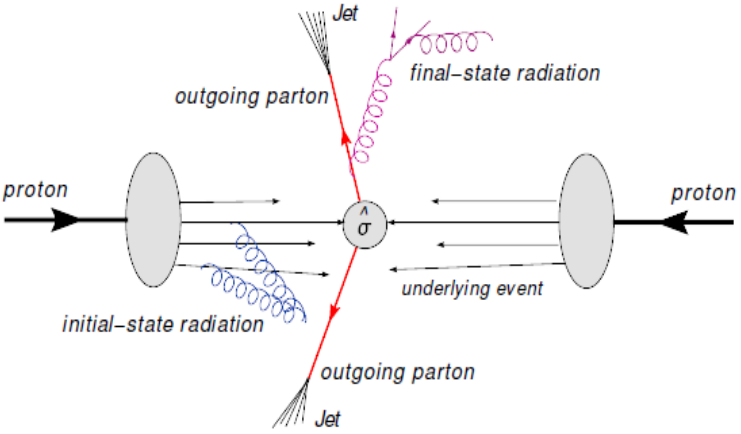

FIGURE 1.2: Jet production in a hard scattering event[1].

force. The heavy ion collisions aim to study that state of matter which is characterized by high temperatures and densities. However, atomic nuclei are spatially extended objects when compared to the proton, which in this case is considered to be *point-like*. An important feature of the nucleus-nucleus collisions is the impact parameter, b, the distance between the geometric centre of the two nuclei measured in the transverse plane of the collisions direction.

1.3 Proton-nucleus collisions

Proton-nucleus (p+A) collisions have a crucial importance in Heavy Ion Collisions. They serve as benchmark to interpret some of the main features of A+A collisions, such as jet suppression. The p+A physics are also of interest by their own allowing the study of nuclear Parton Distribution Functions (nPDF). Namely, gluon saturation[3] and shadowing[4], among others.

1.3.1 p+A as benchmark for Heavy Ion collisions

Proton-nucleus collisions (p+A) are a crucial component of the heavy-ion program. They serve as benchmark to nucleus-nucleus collisions (A+A) to disentangle initial state effects in the nucleus, which are observed in p+A and also happen in A+A (e.g. gluon saturation), from the hot and dense state of matter produced in A+A collisions. p+p collisions are used to study the interaction between partons in vacuum. p+A collisions are used to study the parton interaction within a nuclear environment. A+A collisions are used to study the interaction between partons in the Quark Gluon Plasma state of matter. The usual procedure is to study ratios of observables between the nucleus-nucleus or proton-nucleus and p+p cross sections scaled by the number of binary nucleon-nucleon collisions, N_{coll}. The purpose is to distinguish cold nuclear matter effects that happen in both p+A and peripheral A+A collisions, from the ones produced in central A+A collisions, in which the QGP is expected to occur. These ratios constitute the so-called nuclear modification factor, R_{AA}, a measurement of how the medium can modify the scaling between p+p collisions and p+A or A+A collisions. R_{XX} is defined as:

$$R_{XX}(p_T, \eta) = \frac{1}{\langle N_{coll}^{XX} \rangle} \frac{d^2N^{XX}/dp_T d\eta}{d^2N^{pp}/dp_T d\eta} \tag{1.1}$$

where XX is the collision type one is studying, and can be A+A, p+A or d+A collisions. d+Au collisions at the Relativistic Heavy Ion Collider (RHIC) were used as benchmark in Au+Au collisions and have shown evidences of the jet quenching hypothesis, caused by the QGP, as a genuine final state effect. In central nucleus-nucleus collisions a deficit of high transverse momentum hadrons is observed while this effect is absent in the transverse momentum spectra of the inclusive hadron production in d+Au collisions [5]. To characterize the effects of cold nuclear matter, one has to have a precise knowledge of the PDF both the proton and the heavy nucleus. While in the proton case the PDFs are constrained by a large number of data from HERA and the Tevatron, in the nuclear case this is not true. Much less extensive experimental data on nuclear deep inelastic scattering (DIS) are available in the perturbative region ($Q^2 \geq 1$ GeV^2) and only for Bjorken-x (x) > 0.01 [6]. The LHC assesses completely unexplored regions of the phase space of the nuclear PDF (x < 0.01). And so, for a contribution

to the understanding of the hot partonic matter produced in Pb+Pb collisions, one should also study p+Pb collisions in order to remove the uncertainties of the nuclear PDF.

With the LHC, the TeV scale is achieved for the first time. This unexplored kinematical regime translates into a untapped reach of Bjorken-x and virtuality Q^2 in several orders of magnitude, which allows the study of the nuclear PDF at lower x values.

1.3.2 Centrality

The centrality of a collision can be perceived as a measure of the topology of a collision. In contrast with p+p collisions, when colliding two heavier nuclei one can have distinct events, depending on the impact parameter b of the two nuclei. The objective of estimating the centrality variable is to identify those events and to each one attribute the correspondent centrality class. A simulation model of a collision between two gold nuclei viewed in its transverse and longitudinal plane is depicted in Fig. 1.3(a) and Fig. 1.3(b). For large b collisions it is expected a low number of binary collisions between the nucleons which leads to a low number of particles in the event, while for small b collisions it is expected high number of collisions and the resulting larger number of particles. The number of particles in an event is associated with underlying event at the detector level. Figs. 1.3(d) and 1.3(c) show a simulation of a p+Pb collision.

The characterization of the centrality variable in A+A or p+A collisions is performed considering the Glauber Monte Carlo model [7] which is inspired in the Glauber model[9]. The Glauber Monte Carlo model considers the nucleus as group of uncorrelated nucleons taking into account the density distributions of the nuclei. The collision model considers a random impact parameter b and assumes that the nuclei follow a straight line until the collision. The interaction probabilities between the nucleons of each nuclei is performed using the relative distance between them. This collision model considers as main inputs the nuclear charge densities following a Fermi distribution and the energy dependence of the inelastic nucleon-nucleon cross section. The nucleon-nucleon cross-section is assumed to be equal to the proton-proton inelastic cross-section.

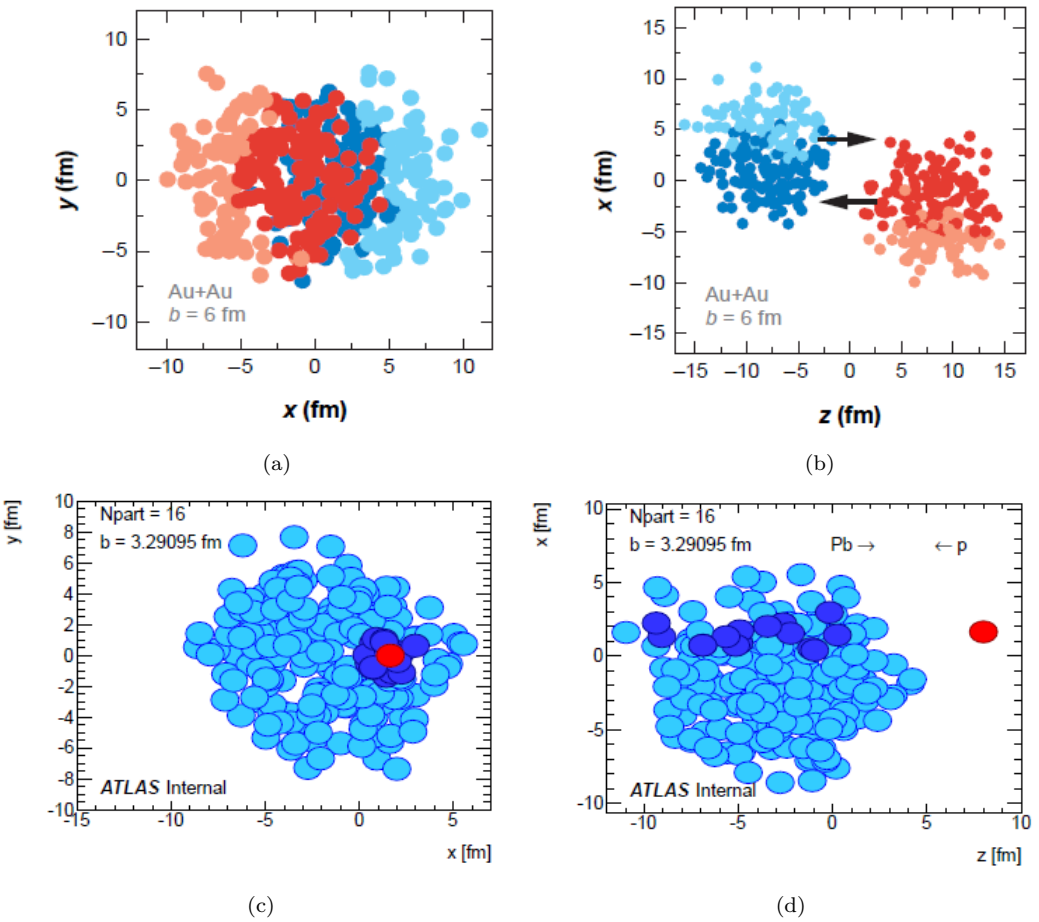

FIGURE 1.3: A Glauber Monte Carlo model of a Au+Au collision event is shown in Fig. 1.3(a) in a transverse view and in Fig. 1.3(b) in a longitudinal view [7]. Fig. 1.3(c) and 1.3(d) show a model of a p+Pb collision event[8].

A "participant" is a nucleon which interacts at least once in a given collision. The number of participants (N_{part}) is the total number of nucleons which interact in a collision, while the number of binary collisions (N_{coll}) is the number of interactions that all nucleons in a given nucleus experience. In nucleus-nucleus (A+A) collisions there are proportional relations between both N_{part} and N_{coll} and the impact parameter, and between the parameters N_{part} and N_{coll} as well as the number of produced particles (multiplicity). In p+A collisions the relation between N_{part} and N_{coll} and the impact parameter is not so straightforward.

With the Glauber Monte Carlo model one can get N_{part} and N_{coll} distributions by simulating many nucleus-nucleus collisions with different impact parameters. Once these distributions are obtained, they are fitted to the experimental data. A measured distribution (e.g., dN_{evt}/dN_{ch} or $\sum E_T^{Evt}$) is mapped to a distribution (N_{part} or N_{coll}) obtained from the Monte Carlo Glauber simulation by defining

'centrality classes' in both measured and simulated distributions. Fig. 1.4 shows an illustrative representation of the correlation between the distributions of N_{part} and the number of charged particles (N_{ch}). The mean values from the same centrality class in the two distributions allows one to separate the different centrality classes. Usually the distributions are divided in percentiles, such that each percentile is a fraction of the total inelastic cross-section. The 'centrality class' of an event is classified between 0 to 100%.

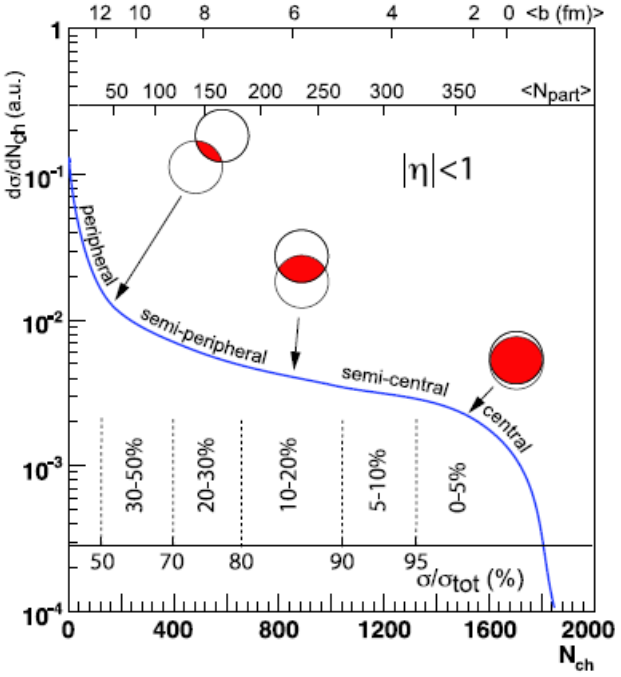

FIGURE 1.4: Correlation between the distributions of the number of participants in a binary collision (N_{part}) and the number of charged particles in a Minimum Bias sample (N_{ch}) are shown. Percentiles of the distribution are also applied in this distribution with no criteria[10].

1.3.3 Jet production

Jets are most often produced in pairs, well-balanced in azimuth and transverse energy (E_T), at leading order and in absence of energy loss. They are the dominant contributor to the total jet production cross-section of hard-scattering events. However, if the hard scatter occurs in the Quark Gluon Plasma (QGP) medium as the one produced in ultra-relativistic heavy ion collisions, the partons lose energy

while traversing the medium, by interactions or induced gluon radiation. This phenomenon is commonly referred to as jet quenching.

One of the many ways to study the jet quenching is the study of dijet asymmetry distributions between the most leading E_T jets in an event, in separate centrality classes. This result shows that while in peripheral collisions the asymmetry distributions are well balanced in E_T, in central collisions the same distributions show no balance between the transverse energy of those jets. More information regarding this topic can be seen at [11].

R_{CP} measurements is also another study to analyse the jet quenching hypothesis. It is defined as the ratio of the differential yields in some centrality class collision to the most peripheral ones, both normalized to the corresponding numbers of binary collisions. The R_{CP} between central and peripheral collisions is defined as:

$$R_{CP}(p_T, y) = \frac{\langle N_{coll}^{Peripheral} \rangle}{\langle N_{coll}^{Central} \rangle} \frac{d^2N^{Central}(p_T, y)/dp_T dy}{d^2N^{Peripheral}(p_T, y)/dp_T dy} \tag{1.2}$$

The jet yield is found to be suppressed by approximately a factor of two in the 0-10% centrality class relative to peripheral collisions. R_{CP} varies smoothly with centrality as characterized by the number of participating nucleons. The observed suppression is only weakly dependent on transverse momentum[12].

1.3.3.1 Jets in p+A collisions

The jet production in p+Pb collisions is found to be also dependent on centrality and rapidity[13]. In this reference results of central-to-peripheral ratios, R_{CP}, as a function of the jet transverse momenta, for different slices of jet rapidity, are presented. Results of this measurement indicate a strong, centrality-dependent reduction on the yield of jets in central collisions relative to that in peripheral collisions. This reduction becomes more pronounced with jet p_T and at more forward (downstream proton) rapidities, as presented in Fig.1.5

The goal of this dissertation is to study the ATLAS jet trigger in this environment, that is dependent on variables such as the centrality class of the collision, the rapidity and transverse energy of the jet, among others.

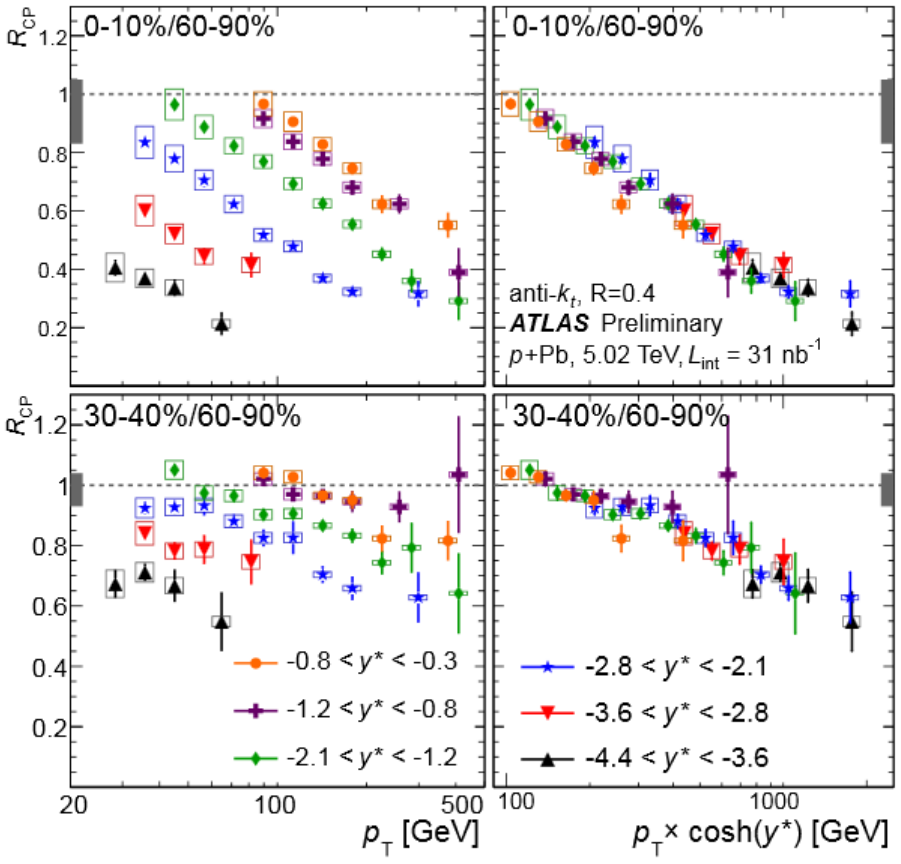

FIGURE 1.5: R_{CP} for R=0.4 jets in p+Pb collisions at $\sqrt{s_{NN}} = 5.02$ TeV. Each panel shows the R_{CP} in jets in multiple rapidity bins at a fixed centrality interval. The top row show the R_{CP} for 0-10%/60-90% and the bottom row show the R_{CP} for 30-40%/60-90%. In the left column, the R_{CP} is plotted against jet p_T. In the right column, the R_{CP} is plotted against the quantity $p_T \times \cosh(y*)$ where $y*$, the rapidity measured in the center of mass frame, is the midpoint of the rapidity bin. Error bars on data points represent statistical uncertainties, boxes represent systematic uncertainties, and the shaded box on the R_{CP}=1 dotted line indicates the systematic uncertainty on N_{coll} for that centrality interval[14].

Chapter 2

Experimental Setup

The European Organization for Nuclear Research (CERN) is a scientific research facility located near Geneva, Switzerland. At CERN exists an accelerator complex in which several experiments were built to study the basic constituents of matter.

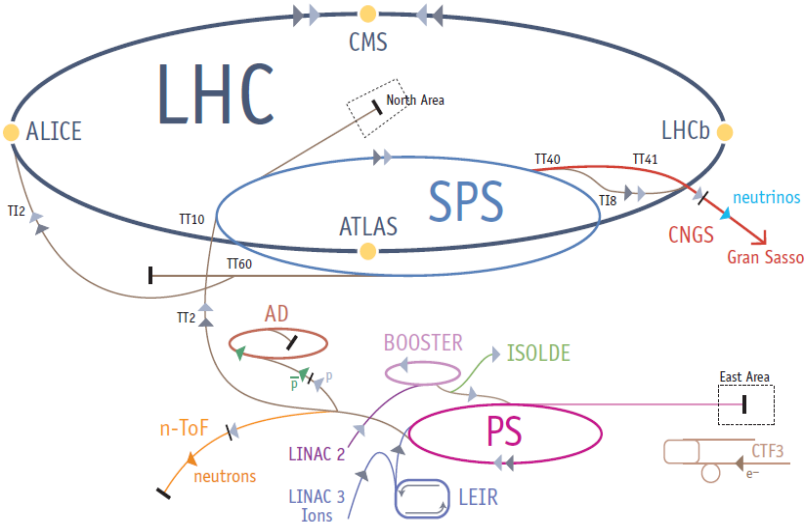

FIGURE 2.1: Schematics of the accelerator complex at CERN. Several accelerators are used to achieve higher beam energies. The proton beam acceleration chain can be seen by following the light blue arrows from Linac2. While the ^{208}Pb beam chain is depict in the dark blue arrows starting in Linac3.

The accelerator complex consists on a chain of accelerator machines, linear and circular accelerators, where the next machine brings the particle beam to a higher energy. The last element of this chain is the Large Hadron Collider (LHC), with a

circumference of 26.7 km. ATLAS, CMS, LHCb and ALICE experiments are found in the LHC ring. In these experiments the beams are forced to collide with each other. Other experiments are carried in relatively smaller accelerator machines using beams of lower energies, such as ISOLDE and COMPASS experiments. A schematics of the accelerator complex is shown in Fig. 2.1.

2.1 The Large Hadron Collider

The basic structure of matter can be described by the Standard Model of Particle Physics[15]. However this is an incomplete model. The LHC was built and designed to provide with some answers that this model doesn't consider, such as the existence of dark matter and dark energy in the universe, test the super-symmetry model, hot quark matter, among others. These subjects are studied by making proton-proton or lead-lead collisions in the LHC.

The LHC machine structure [16] consists of two parallel beam pipes where protons and/or ^{208}Pb nuclei circulate in opposite directions. The beam pipes cross at four specific points, called interaction points (IPs). In each point the beam constituents are made to collide and the experiments which are centered around the IPs are used to record the results of the collisions. In order to diminish random collisions with air molecules, the beam pipes are kept at ultra-high vacuum conditions reaching an average of 10^{-13} atm.

The counter-rotating beams are contained within a single magnetic structure. The particles orbits are controlled by 1232 magnetic dipoles and the focus of the beam constituents in the transverse plane is maintained by 392 quadrupole magnets using an alternating field. These are superconducting magnets that operate at 1.9 K. The LHC holds 8 radiofrequency (RF) cavities per beam. These are responsible for the acceleration of the beam to the largest energy and guarantee high luminosity at the interaction points.

Before reaching the LHC, protons follow a certain accelerator chain that is depicted in Fig. 2.1. Protons are obtained by stripping the electrons from hydrogen atoms and can be accelerated to an energy of 50 MeV in the linear accelerator Linac2. Later, protons are injected to the Proton Synchrotron Booster (Booster) where they are accelerated up to 1.4 GeV. Energies of 25 GeV are then reached

at the Proton Synchrotron (PS). At the Super Proton Synchrotron (SPS) protons are accelerated to 450 GeV. Finally, in the LHC energies of 4 TeV can be reached.

Regarding the ^{208}Pb ions, these are produced from an heated sample that is primarily ionized by an electron current. This ionization can reach the state of Pb^{29+}. An additional ionization is reached by impinging the Pb ions on a carbon foil. The stripped ions are fed to the Low Energy Ion Ring (LEIR). The ions are injected to the PS with an energy of 72 MeV/u where the beam is accelerated to 5.9 GeV/u. Only after passing a second foil, in order to achieve a complete stripping, the beam is injected to the SPS. The beam is sent to the LHC with an energy of 177 GeV/u where it is accelerated to 1.38 TeV/u. This scheme of injection is also shown in Fig. 2.1.

A beam might circulate about 10 hours in the LHC. The hadrons circulate in the ring in bunches due to the RF acceleration. In this type of accelerators the ions can be accelerated only when they pass a cavity and the RF field has a certain orientation. In the LHC, the proton beams are made of 2808 bunches, each bunch contain 10^{11} protons.

The size of the bunches varies within the ring, being reduced around the interaction point in order to increase the probability of collision at each of the four interaction points.

2.2 ATLAS

2.3 Detector Overview

ATLAS [17] is a multi-purpose particle detector that is located at the Interaction Point 1 (IP 1) of the LHC. It is 25 m high, 44 m long and weighs approximately 7000 tonnes. The detector was designed to identify and measure all the products of the collisions of the beam particles. Its main purpose is to verify the Standard Model (SM) and probe for physics beyond the SM. ATLAS is able to study p+p, Pb+Pb and p+Pb collisions.

The ATLAS detector is organized in layers surrounding the interaction point. From the inside to the outside, it consists of the following subdetectors: the Inner

Detector, the Magnet System, the Electromagnetic and Hadronic calorimeters and the Muon Spectrometer, which in their turn are composed of more sub-detectors. A schematic view of the complete layout of the ATLAS detector can be found in Fig. 2.2. The Electromagnetic, Hadronic calorimeters and the Muon Spectrometer are divided into barrel and end-cap detectors. In the barrel the detectors are arranged in concentric cylinders, around the beam axis, while the end-cap detectors are imprinted in disks perpendicular to beam axis located at the ends of the barrel. The variables used to map and limit the detector are the (η,ϕ) coordinate system and are defined in App.A along with some other used variables.

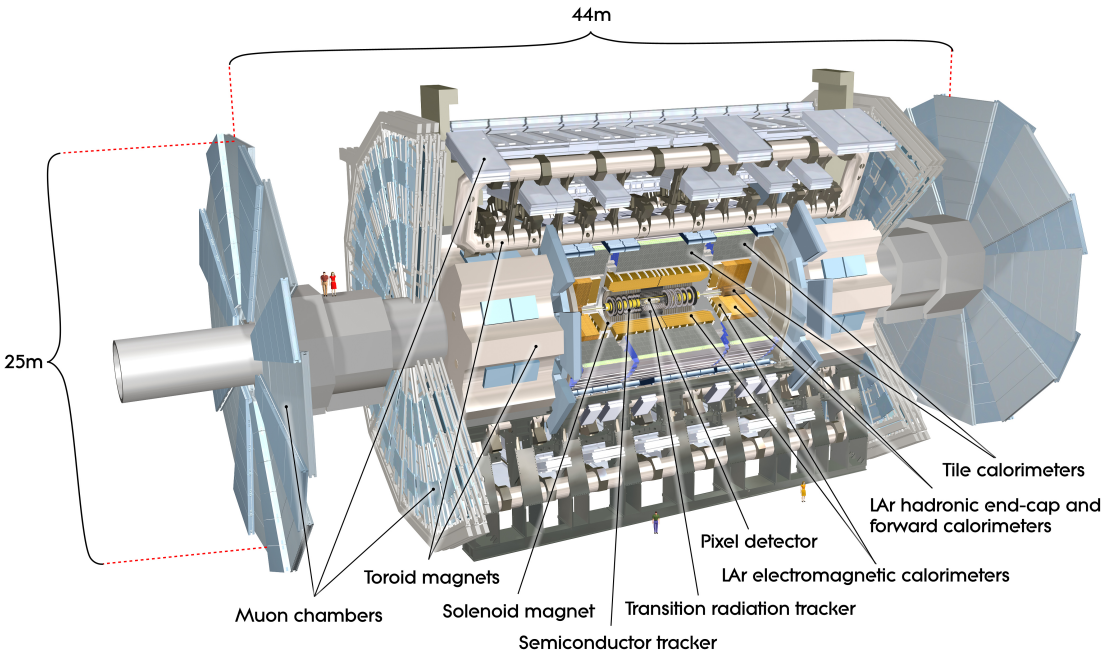

FIGURE 2.2: Overview of the ATLAS detector where the main sub-detector systems are identified.[17]

Another important parts of the ATLAS detector are the software and hardware components to digest the millions of events per second. Nowadays such a high rate of events that is delivered by the LHC is impossible to record completely. The trigger and the data acquisition systems aim to select potential interesting events to save, according to the physics one is interested in.

In the following sections the different components of the ATLAS detector will be briefly introduced with exception for the calorimeters, which due to the relevance for this dissertation are extensively exposed.

2.4 The Inner Detector

The Inner Detector (ID) is the first detector system that surrounds the high-radiation area near the IP. The ID is composed of a set of subdetectors: the Pixel Tracker, the Semiconductor Tracker (SCT) and the Transition Radiation Tracker (TRT). A schematic view of the ID is shown in Fig 2.3.

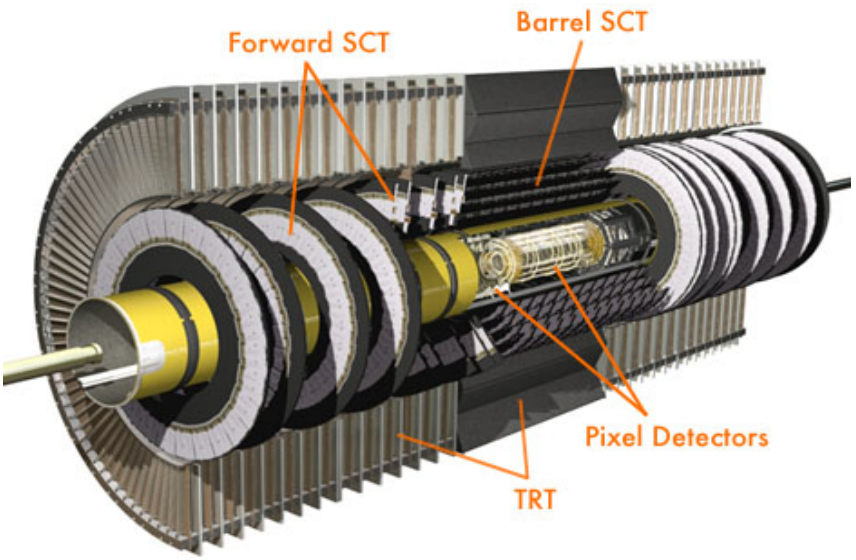

FIGURE 2.3: Overview of the Inner Detector and its detection subsystems: the Pixel Tracker, the Semiconductor Tracker (SCT) and the Transition Radiation Tracker (TRT)[17]

The purpose of the ID is to accurately identify and reconstruct the trajectories of charged particles, combining high-resolution detectors near the IP with tracking elements at a larger radii. The detector subsystems are all immersed in a 2 T nominal magnetic field provided by the Central Solenoid Magnet. This allows to measure with excellent resolution the momentum of the charged particles. Precision vertex reconstructions are also achieved with the ID.

Due to its working environment, i.e., high radiation area, the detector takes advantage of fast and radiation-hard electronics and sensors.

The next paragraphs summarize each of the sub-detectors that compose the ID.

The **Pixel Tracker** is the first layer of the ATLAS detector. It is a radiation hard semiconductor detector that measures all tracks within a $|\eta| < 2.5$ region. It uses 80 million silicon pixel sensors to provide high granularity in the barrel region, each pixel sensor with a $50 \times 400\,\mu m^2$ area. The vertexing layer is the closest to the interaction point, and provides precision measurements over the full acceptance. The Pixel Tracker is crucial to identify and reconstruct the primary and secondary vertices, due to its proximity to the interaction point and highly segmentation, allowing a flavor-tag analysis (e.g. identifying B-Hadrons).

The **Semiconductor Tracker** is a silicon micro-strip detector that is placed at a larger radii than the Pixel Tracker enclosing it. It also contributes to the measurements of momentum, impact parameter and vertex position.

The **Transition Radiation Tracker** is the outermost subdetection system of the ID. It is composed of gaseous straw tube detectors. The barrel TRT straws are parallel to the beam direction, while all end-cap tracking elements are located in planes perpendicular to the beam direction. Each straw is filled with a gas mixture with 70 % of xenon. The straws are within a matrix of polypropylene fibres. When a charged particle passes through the polypropylene photons are produced. These ionize the gas in the straw tubes and the collected signal is then read out. This detector not only provides high resolution momentum measurements but also identifies electrons based on the photon signature when traversing the drift tube.

2.5 Calorimetry

Calorimeters are used to measure accurately the position, time[1] and energy of particles by their absorption. Calorimeters are used in high energy physics to measure the energy of all hadronic and electromagnetic interacting particles. They can account for missing transverse energy and also provide fast and efficient trigger output. Some of the most important features include energy resolution, position resolution, signal speed, Gaussian response signals and a good known relationship between the energy and signal. The energy resolution improves with energy which

[1] A time measurement relative to the LHC clock can be measured for some ATLAS detector components

is proportional to $1/\sqrt{E}$ in a calorimeter, in contrast with a magnetic spectrometer which has the momentum resolution proportional to p.

Calorimeters are designed according to the interaction processes and the expected particle energy. Different interaction processes may occur for electromagnetic and hadronic particles at a given energy. In the case of electrons, positrons and photons, the energy loss is dominated by electromagnetic interactions. In the case of strong-interacting particles the energy loss processes are substantially more complex than the electromagnetic case. The reason lies in the larger variety of strong processes that may occur at the particle level and with the interacting nucleus and also electromagnetic interactions. Moreover, not all the energy loss caused by strong processes can be measured as it will be discussed.

When a high energy particle interact with the calorimeter material it will create additional particles through several processes, not necessarily in the same direction as the primary particle. In their turn these secondary particles create further particles. This process repeats itself until the last created particle has insufficient energy to create more particles. The entire process of production of particles constitutes a particle cascade or shower. This shower of particles develops until all particles are completely stopped. At this stage almost all the energy of the primary particle is deposited.

2.5.1 Electromagnetic Showers

An electromagnetic particle shower happens by several different processes. The dominant energy loss for photon in electromagnetic processes are the photoelectric effect (occurs with more probability at low energies), the Compton scattering (is more likely to occur in the keV to MeV energy scale) and the pair production (this process happens at energies larger than 1 MeV). The principal source of energy loss in electrons and positrons at 100 MeV is bremsstrahlung when the electrons interact with the electric fields of the atomic nuclei of the calorimeters. This process generates many soft photons that are absorbed by Compton scattering or photoelectric effect, and a few energetic photons that will produce an electron-positron pairs. These soft particles in a shower carry most of the electromagnetic energy of the primary particle.

The electromagnetic cascade is characterized by the radiation length (X_0), the longitudinal spread and transverse spread. The radiation length can be perceived as the distance travelled in which an electron looses on average $1 - e^{-1}$ of its energy. In the case of a high energy photon, X_0 is the mean free path in which a electron-positron pair is produced with a probability of 7/9. The radiation length is proportional to the mass number and the atomic mass, $X_0 \propto A \times Z^{-2}$, thus calorimeters are designed with high Z materials such as lead, in order to minimize the shower length and absorb it completely. The radial spread is determined by the Molière radius (R_M), which is a function of X_0 and E_C. Roughly 90% of the energy is contained inside a cone of radius R_M around the shower's axis.

2.5.2 Hadronic Showers

Hadronic showers are more complex than the electromagnetic showers. Not only we have to account for the energy losses of the incoming hadron but also account for the energy loss with the nuclei whom the hadron interacted. Regarding the incoming particle, some high energy neutral hadrons may decay in to photons and charged hadrons suffer energy loss through ionization of the medium. This means that an hadronic shower usually contains electromagnetic component. On the other hand the interacting nuclei also accounts for energy loss by spallation reactions and the nuclear binding energy associated with that reactions. The detection efficiency of the hadronic calorimeter is, in general, worse than in the electromagnetic. Undetected energy losses can happen due to neutral particles such as neutrinos and slow neutrons; backscattered charged particles and muons that escape the hadronic calorimeter completely.

The hadronic shower contain an electromagnetic component which has a different shower development and overall calorimeter response. The non-compensation between the two components has to be accounted for. The non-electromagnetic component of the hadronic shower can either be not detected totally or often too slow to be within the detector time window. This will not only destroy the correlation between the primary particle energy and the detector response but also decrease the energy resolution, making it non-gaussian. Experimentally this non-compensation is determined by signal tests of e/π ratios at different energies and applying calibration parameters to the measured energy.

In hadronic showers, the nuclear absorption length λ_0 is the equivalent parameter of the radiation length X_0 in electromagnetic showers. λ_0 is the mean free path before an inelastic interaction occurs and is proportional to the inverse of the density of the material and the nuclear inelastic cross-section. Usually the absorption length is larger than the radiation length which requires hadronic calorimeters to be larger.

Fig. 2.4 shows different types of particles and their typical behaviors in interacting with the ATLAS detector, and more specifically their interaction with the calorimeters material as described in this section.

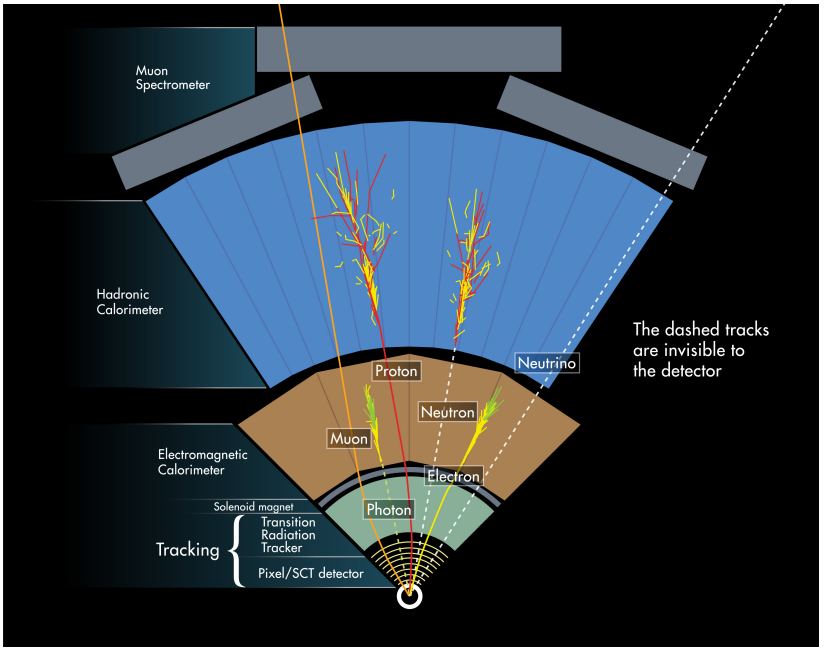

FIGURE 2.4: Particle detection in the hadronic and electromagnetic calorimeters of ATLAS. Showers produced by a photon and electron in the electromagnetic calorimeter and the hadronic showers induced by a proton and a neutron in hadronic calorimeter are shown [17].

2.5.3 ATLAS Calorimeters

The ATLAS detector is composed of two main sampling calorimeter systems: the Electromagnetic calorimeter and the Hadronic calorimeter. Both calorimeters have backward-forward symmetry and are grouped in two distinct parts: the barrel and two end-caps. The barrel part is concentric around the axis beam, and end-caps which are placed at both ends of the barrel and are perpendicular to the beam pipe. Fig 2.5 represents a schematics of the ATLAS calorimeters [17].

ATLAS electromagnetic and hadronic calorimeters were built with alternating stacks of absorption material layers followed by detection devices, which are commonly known as sampling calorimeters. Using different absorption materials, different particles can be measured such as photons, electrons and hadrons. Other particles, such as neutrinos and muons, deposit none or little energy loss in the calorimeters. In the case of neutrinos, their energy can be inferred from the missing transverse energy as these calorimeters are hermetic detectors. Sampling calorimeters, when compared to homogeneous calorimeters, which are characterized by a medium which is simultaneously active and passive, allow a better segmentation and cope better with radiation damage to the detector. On the other hand they have worse energy resolution and record only the part of the energy deposited in the active medium.

The segmentation of the calorimeter allows the determination of the 4-momentum vector of the particles. The signals collected in different cells allow a definition of the shower axis and thus the direction of the particle that traversed that medium. The material from which the calorimeter is made determines the different types of signals used.

The calorimeters were designed with two distinct technologies: liquid argon technology and tile scintillators. In the liquid argon technology a particle is detected by ionizing the cryogenic liquefied noble gas in the active medium and the absorber is composed of lead laminated with steel support plates. The tile scintillator technology uses steel plates as passive material and scintillating plastic tiles as its active medium. As the particle passes through the scintillating tile, light is produced and a wavelength shift fiber will re-emit the light with a longer wavelength (lower energy) and delivered to the photomultiplier module.

2.5.3.1 Electromagnetic Calorimeter

The electromagnetic calorimeter (EM) in ATLAS is composed of the electromagnetic barrel (EMB) component and two electromagnetic end-caps (EMEC) components. All of these components employ the liquid argon technology. The EMB has a sampling calorimeter in front of it, called the Pre-Sampler, which is used to improve the measurement of the lost energy by photons and electrons.

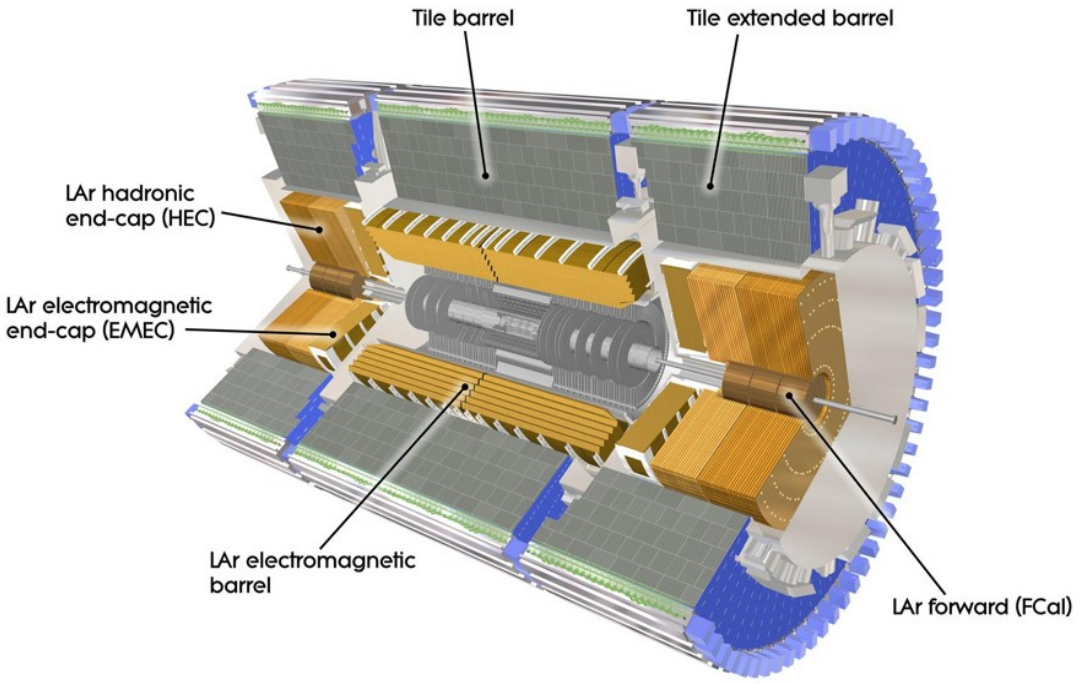

FIGURE 2.5: Overview of the ATLAS Calorimeters: Electromagnetic and Hadronic. The technologies used were Liquid Argon (LAr) and tile, these are also indicated for each calorimeter component[17].

The Electromagnetic calorimeter also provides high granularity and good hermicity due to its "accordion geometry" in the passive material, as can be seen in Fig. 2.6. This geometry is symmetric in ϕ and more importantly doesn't allow for any azimuthal cracks in the calorimeter.

The Electromagnetic Barrel surrounds the Central Solenoid Magnet and has a coverage of $|\eta| < 1.475$. It is composed of three concentric layers with different granularities in η and ϕ, having area cells of 0.025×0.0245. In the central region of $|\eta| < 2.5$ the EM calorimeter has three longitudinal sampling layers with different segmentations.

The EMEC are placed at each side of the barrel and covers $1.375 < |\eta| < 3.2$. Regarding the granularity, the EMEC are also highly segmented in η and ϕ, having area cells of 0.025×0.0245 in the $\eta \times \phi$ phase space.

The radiation length associated to the EM calorimeter has a minimum of 24 X_0 in the EMB and 26 X_0 in the EMEC. [18].

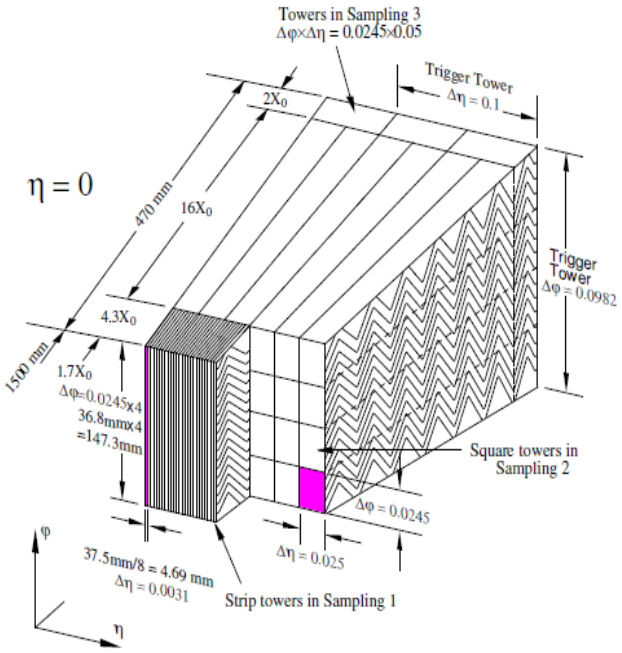

FIGURE 2.6: Perspective view of the EM calorimeter segmentation. The accordion geometry allows the calorimeter to not have azimuthal gaps, is ϕ-symmetric, and adding an highly segmentation to identify precisely the position of the particles that traverse the material, results in a great accuracy of energy measurements[17].

2.5.3.2 Hadronic Calorimeter

The Hadronic calorimeter is the the next detector system that surrounds the EM. It is divided in two subsystems; two hadronic end-caps (HEC) and the Tile Calorimeter (TILECAL) which in turn is divided in Hadronic Barrel (HB) and hadronic extended barrel (HEB). Between the hadronic barrel and hadronic extended barrel lies a crack of 68 cm in which are service pipes, Inner Detector supporting cables as well for the solenoid magnet and for the electromagnetic calorimeter.

The TILECAL uses polystyrene scintillating tiles technology and steel as active and passive mediums respectively. The tile planes are oriented perpendicularly to the beam axis and are radially staggered in depth as it can be seen in Fig 2.7. This geometry of modules provides an uniform signal response of the calorimeter and hermetic coverage.

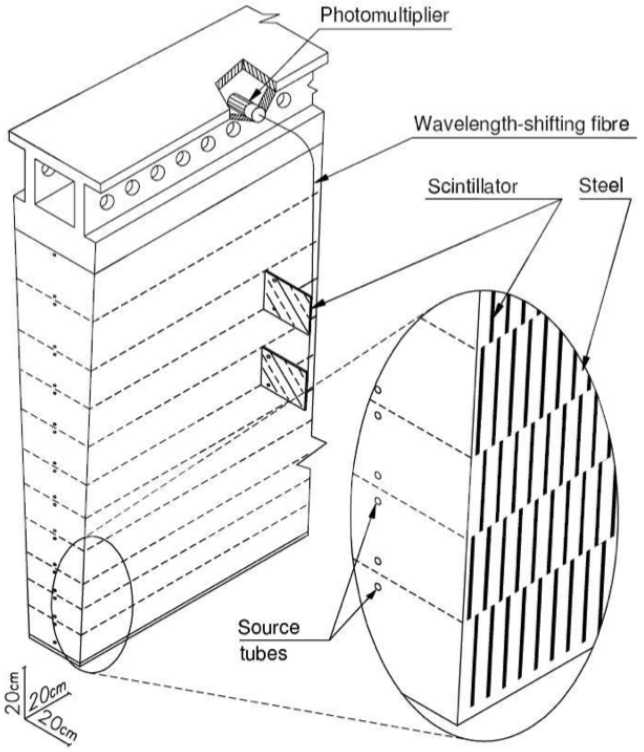

FIGURE 2.7: A tile calorimeter module composed of the steel absorbers, the scintillating tiles, the wavelength shift fibers and the photomultipliers[17].

TILECAL has three sampling layers in the longitudinal direction. The grouping of the tiles and photomultiplier tubes allows a segmentation in η and ϕ. The resultant granularity for these modules is 0.1×0.1 in the $\eta \times \phi$ plane. Also, the TILECAL has an interaction length minimum of $\lambda_I = 7.4$ in its η-central region.

2.5.3.3 Hadronic end-caps

The hadronic end-caps are symmetric in $\pm$ z and are located after the electromagnetic end-caps. The difference between these modules, the electromagnetic end cap and the hadronic end cap, lies in their sampling materials. The hadronic end cap is composed of liquid argon technology as the active medium and as a passive medium copper to increase the interaction length in comparison to the EM Liquid Argon system. The HEC share the cryostat plates with the EMEC and the forward calorimeter. Being composed of two independent wheels and these extend the η coverage $1.5 < |\eta| < 3.2$. However the segmentation is different for

different η ranges: for $|\eta| < 2.5$ is $\eta \times \phi = 0.1 \times 0.1$, while for $2.5 < |\eta| < 3.2$ it is $\eta \times \phi = 0.2 \times 0.2$.

2.5.3.4 Forward Calorimeter

The main purpose of the Forward Calorimeters (FCal) is to extend the acceptance of the detector in η and probe physics at forward pseudorapidity. The FCal range in η is $3.1 < |\eta| < 4.9$. This increase in $|\eta|$ allows for more more accurate missing transverse energy measurements. The FCal is also of great importance in Heavy Ion collisions, as it is the detector in which it is defined the centrality of the collision. The FCal are located between the beam pipe and the hadronic end caps, being z-symmetric (the axis in the direction of the collision axis). Each of them is segmented along the z axis in 3 sections; the closest to the interaction point is regarded has a sampling electromagnetic calorimeter, being composed of stacks of liquid argon and copper as the active medium and absorber respectively. In respect to its hadronic part, it is segmented longitudinally in 2 sections, the active mediums and passive mediums are liquid argon and tungsten made. The granularity in the $\eta \times \phi$ plane is 0.2×0.2. It has a high radiation level formed of low transverse energy particles with high energy. The detector was designed with a fast response to minimize the effect of pileup from either a previous bunch crossing or multiple hard scattering event.

2.5.4 Minimum Bias Trigger Scintillators

The Minimum Bias Trigger Scintillator (MBTS) is a calorimeter which is made of only active medium. Composed of two z-symmetric components, they are installed at the ends of the Inner Detector at $\pm\, 3.6\, m$, and cover a range from $2.09 < |\eta| < 3.84$. The main purpose of this detector is to select interesting events by requiring a minimum number of hits. It can be also used in offline analysis to reject out of time signals, considering the timing of the signal measurement relative to the LHC clock time.

2.5.5 Zero Degree Calorimeters

The Zero Degree Calorimeters (ZDC) are sampling calorimeters installed at $\pm 140\,m$, just beyond the beam pipe splits. They cover a range of $|\eta| > 8.3$. These detectors are mainly used in Heavy Ion Collision experiments. They can measure spectator neutrons in lead-lead collisions that are not deviated in the magnetic fields of the beams, as charged particles and nuclei. It can also be used to trigger interesting events by requiring a hit, and thus reject photonuclear collisions, beam gas and beam halo effects.

2.6 Muon Spectrometer

The Muon Spectrometer (MS) is the last detector that is surrounding the beam pipe. It is designed to detect muons that are created in the hard scatter. It can be used to identify the position, momentum and the signal of all the charged particles that are not absorbed by the hadronic calorimeters. A scheme of the Muon Spectrometer can be found in Fig. 2.8.

Interspaced with the Muon spectrometer are found three large Semiconductor Toroid Magnets (SCT Magnet), one at the barrel region and two at the respective end caps. In contrast with the Central Solenoid Magnet which has a constant magnetic field, the SCT Magnets haven't and the barrel toroid magnet ($|\eta| < 1$) can vary from 0.2 T to 2.5 T in its bore, while the end cap toroid magnets ($1.4 < |\eta| < 2.7$) the maximum value is 3.5 T. In the transition region between the barrel and end-caps ($1 < |\eta| < 1.4$), the magnetic field is generated by the two magnetic systems and has an average field of 1 T.

The Muon spectrometer has four types of detectors, two of them located in the barrel region: the Resistive Plate Chambers (RPC) and the Muon Drift Tubes (MDT) and two in each the end caps: the Thin Gap Chambers (TGC) and a system composed of the MDT and Cathode Strip Chambers (CSC). The RPC and TGC systems were designed to provide the Muon Spectrometer a fast response but less accurate position measurements, ideal to trigger muon objects. On the other hand, the MDT and the CSC have accurate tracking of the position, momentum and charge measurements.

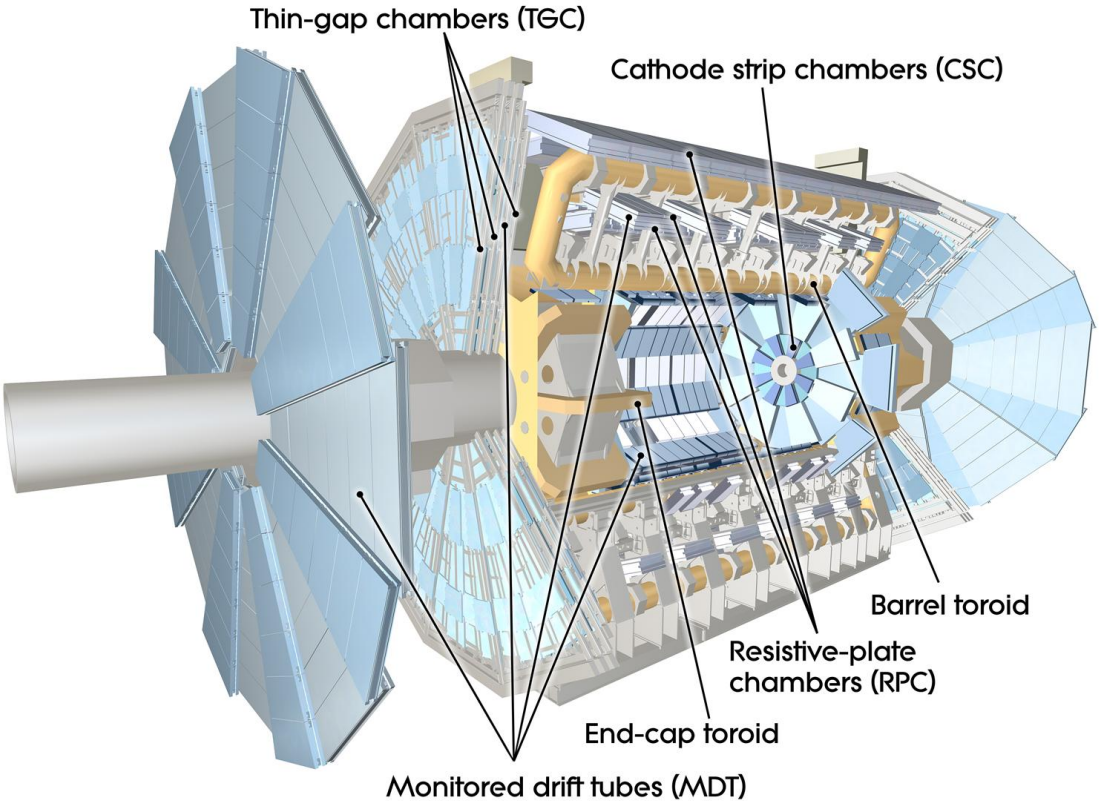

FIGURE 2.8: Overview of the Muon Spectrometer.[17]

Chapter 3

Jet Trigger System

An overview of the entire trigger and data acquisition system is presented in the first section. The following sections present with some detail the jet trigger system, finishing with the presentation of the jet trigger menu for the 2013 p+Pb run.

3.1 Overview of the Trigger and Data Acquisition systems

The Trigger and Data Acquisition system (TDAQ) [17] plays an important role in the ATLAS detector as it manages the processing of data streaming. With current technology it is impossible to record all events of a designed collision rate of 40 MHz, therefore the TDAQ system is required. This system was designed to reduce the input data rate to approximately 200 Hz which corresponds to approximately $300MB/s$ devoted to offline storage and processing of the data. With the development of new software and hardware components, the input data rate was increased to 400 Hz during the p+Pb data acquisition. In these few hundred Hertz the aim is to select interesting and rare events for offline analysis. This corresponds to a factor of 10^7 reduction of the data rate and with a latency of only a few seconds.

The ATLAS trigger system is comprised of three levels, each one adding more complexity to the previous. The Level 1 (L1) is the first level and is a hardware-based system that uses information from both electromagnetic and hadronic calorimeters and the muon spectrometer sub-detectors. The second and third levels of the ATLAS trigger system are known as Level 2 (L2) and Event Filter (EF). Both

subsystems are software based, and use not only information from the calorimeters and muon systems but also from the Inner Detector. Together, L2 and EF are known as the *High Level Trigger* (HLT).

The trigger system is responsible for the event selection that fulfils at least one of the thousands possible conditions (*triggers*) at each bunch crossing. There are triggers designed to identify electrons, muons, photons, jets, or select specific jets (e.g. jets with b-flavour tagging or specific B-physics decay modes). There are also triggers specialized in global event properties such as summed transverse energy ($\sum E_T$) and missing transverse energy (E_T^{miss}), the latter commonly associated with neutrinos.

A schematic diagram of the ATLAS trigger system is presented in Fig. 3.1

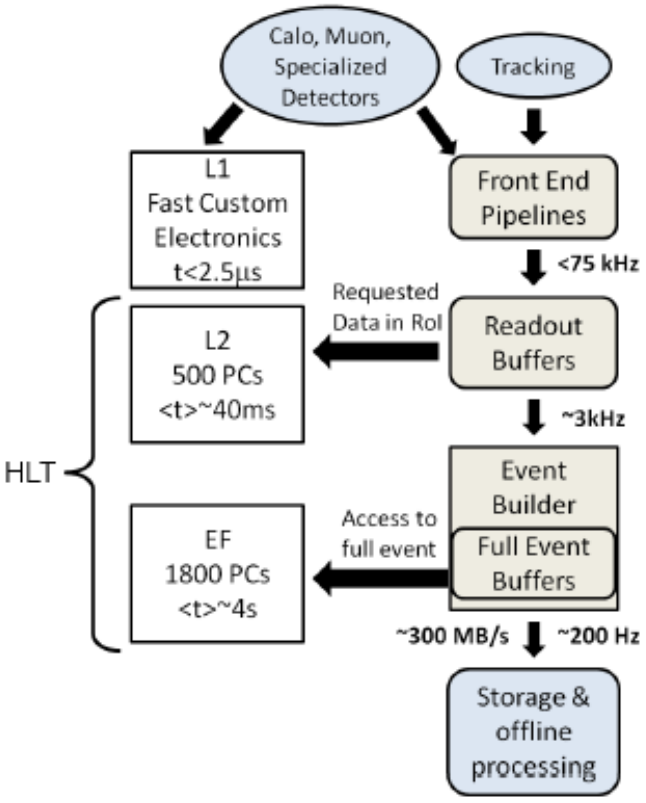

FIGURE 3.1: Schematic diagram of the ATLAS trigger system. The three trigger levels (L1, L2 and EF) aim to select and record a broad variety of rare physics events from a designed 40 MHz bunch crossing rate.[19]

The L1 Trigger is built with fast custom trigger electronics in order to get a latency of less than 2.5 μs, reducing the rate to a maximum of 75 kHz. From the information of the calorimeters and muon tracks the L1 trigger identifies and selects *Regions of Interest* (ROI) which are used in the next trigger levels.

The HLT is a commodity computing system connected by fast dedicated networks. After the L1 trigger selection, the data from each detector is transferred to a detector-dedicated Readout Buffer (ROB), which stores the event depending on the L2 decision. A set of ROBs are gathered in the Readout systems (ROS) and are connected to the HLT networks. The L2 trigger which is based on fast custom algorithms, process the data only within the ROIs from L1. The ROS send the data to L2 upon request, which is associated to detector elements inside each ROI. This results in a considerable reduction of the data processed and transferred to L2. The L2 has a latency of 40 ms and its designed rate is 3 kHz.

All events that pass the selection criteria at L2 are passed to the Event Builder which reads out the data from the entire detector assembling all the different parts of data from the ROBs. The full event data is processed by the last stage of the trigger system, the Event Filter. It consists of a farm of commodity processors that runs faster or modified versions of offline algorithms. The EF reduces the event rate to at most 400 Hz with an average processing time of a 4 seconds/event.

After processing the data at the EF, the events selected by the trigger system are written to data *streams* with dedicated trigger types. Usually data streams are separated in two types, physics data streams and calibration data streams.

Four primary physics streams were configured in the 2013 p+Pb run:

- *MinBias*: the Minimum Bias stream, which recorded minimum bias and high-multiplicity triggered events from various subsystems including the MBTS, ZDC, ID detectors, among others. The allocated bandwidth for this stream was 250 Hz.
- *HardProbes*: the HardProbes stream recorded events associated with electrons, photons, muons, jets and missing transverse energy and had an allocated bandwidth of 150 Hz.
- *UPC*: the ultra-peripheral collisions stream, which recorded events associated with photo-nuclear processes, characterized by a low track multiplicity. This stream had a dedicated bandwidth of 10 Hz.
- *MinBiasOverlay*: the Minimum Bias overlay stream, had a 5 Hz bandwidth. This stream recorded a sample of minimum bias events that would be later embedded with PYTHIA Monte Carlo samples.

- *Express Stream*: about 10% of the events are written into the Express Stream. The prompt offline reconstruction of this data provides calibration and Data Quality (DQ) information prior to the reconstruction of the four physics streams that were defined before.

This dissertation focuses on the performance of jet triggers, recorded on the stream HardProbes, using the MinBias stream. The chosen stream allows for an unbiased sample of events which no other primary physics stream can offer. Moreover, the jet trigger chains aren't defined in the MinBias stream but the trigger algorithms ran and the information of the event is recorded, thus one can emulate the trigger decision in order to study the jet triggers.

3.2 Trigger system configuration

The trigger system is configured by a trigger menu in which are defined trigger chains. These are composed of a sequence of conditions from the three trigger stages, that ultimately characterize the object triggered.

Each trigger chain has a specific rate, which is the number of times the object of interest is selected in a second. This rate has to be only a fraction of the maximum output rate of the EF and so prioritize the physics we are interested in recording. There are three ways of controlling the rates of a given trigger signature: by changing energy thresholds, applying different sets of selection cuts (e.g. isolated objects) or prescales.

Prescale factors can be applied to each level of the trigger. A prescale of 20 means that 1 in 20 events triggered will move to the next stage. Generally the rate depends on luminosity, therefore the prescale sets are automatically modified in each of the trigger levels to accommodate the change of luminosity, in order to maximize the bandwidth available and ensure a constant output rate.

To summarize, the trigger menu is developed according to the physics we are interested in recording. The prescales are automatically generated according to a set of rules that take into account the priority that each trigger chain has in the menu. The trigger chains can be categorized as: *primary triggers*, which select the events with the properties of the physics we are interested in and should not

be prescaled; *supporting triggers*, which serve as a support to the primary triggers (e.g. orthogonal triggers for efficiency measurements or prescaled triggers with of a lower E_T threshold); *Monitoring and Calibration triggers*, used to collect data used to evaluate the performance of the triggers and detectors.

3.3 Jet trigger overview

The ATLAS calorimeter trigger uses information from the hadronic and electromagnetic calorimeters to identify and select localized objects (e.g. electron/photon, tau and jet) and global transverse energy triggers. Due to the nature of this dissertation it will be only discussed the jet trigger system. Other trigger systems information can be found in Ref.[17, 18].

3.3.1 Level 1

The jet trigger is a subsystem of the ATLAS trigger, being the L1 trigger its first component. It reconstructs the jets using reduced granularity calorimeter information from both calorimeters, hadronic and electromagnetic. At L1 the energy in both calorimeters is calibrated only at the EM scale. The L1 decision is based on the information from analogue sums of calorimeter elements that define *trigger towers*. The trigger towers in each of the two ATLAS calorimeters are separate. The segmentation of the calorimeter is η dependent, therefore these trigger towers have different granularity in η. In the central region is approximately $\Delta\eta \times \Delta\phi = 0.1 \times 0.1$ for $|\eta| < 2.5$. In more forward regions the granularity is broader. In the $2.5 < |\eta| < 3.2$ the trigger tower size is $\Delta\eta \times \Delta\phi \equiv 0.2 \times 0.2$, while in the FCal ($3.2 < |\eta|, < 4.9$) there is no η segmentation and $\Delta\phi \equiv 0.4$. The jet and energy-sum processor uses 2×2 sums of trigger towers, called jet elements, to identify jet candidates. This means that there is a minimum resolution of 0.2×0.2 at η-central region, despite the smaller trigger tower size.

Jets Regions of Interest (ROI) are defined as $4 \times 4, 6 \times 6$ or 8×8 trigger tower windows with its position defined in an 2×2 trigger tower area of maximum energy. The summed transverse energy also have to exceed a predefined threshold imposed in the trigger menu. This information will be then processed to make a global L1 trigger decision.

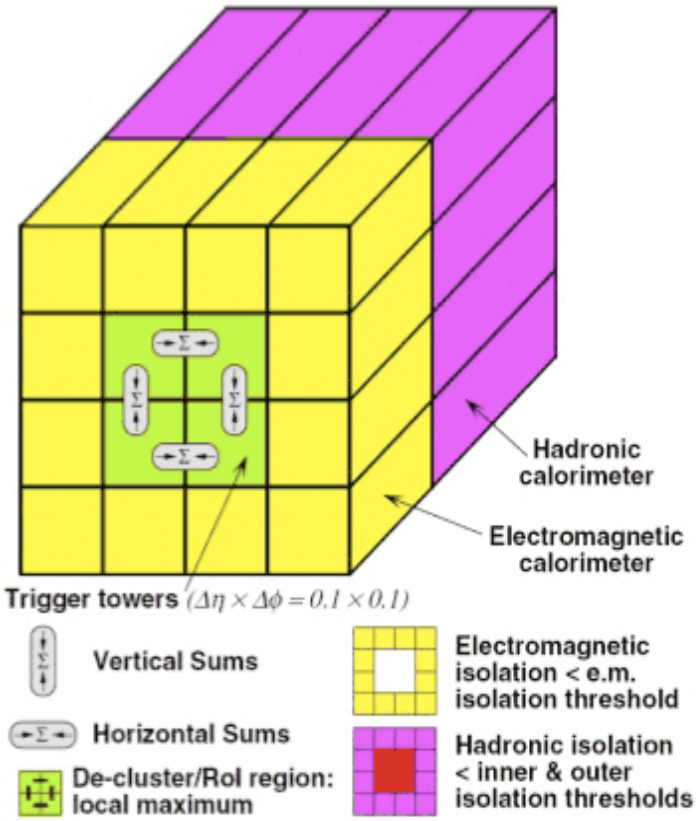

FIGURE 3.2: Sliding windows of the electron/photon and tau algorithms with its sums to be compared to programmable thresholds. The same procedure is used to identify L1 triggered jets with larger sliding window algorithms.[17]

Fig. 3.2 shows an example of a 4×4 sliding window, defined by 4×4 trigger towers. This sliding window is used to identify jet candidates and form global transverse energy sums.

3.3.2 Level 2

In the 2013 p+Pb run, the L1 output rates of the triggered jets were lower than the EF input rates. This allowed the L2 jet trigger to run in a pass-through mode, which means that although the L2 would run its algorithms, the event passed to the EF trigger stage despite the L2 decision. The menu for jet triggers is defined by a L1 jet trigger decision and/or a EF jet trigger decision chain, as we will see in due time. The information regarding the L2 jet trigger in this subsection will be only informative as it was not used in any time in this analysis.

In order to maintain a short period of the order of 40 ms processing per event, the L2 trigger jet system reconstructs and identifies candidate jets only within

the ROI defined in L1 and with a basic jet cone algorithm. The position and energy of each calorimeter cell within the ROI is read out and is used as input for the L2 cone-shaped jet reconstruction algorithm. This algorithm has a previously configured radius in the $\eta \times \phi$ space. It takes into account all the calorimeter cells within the region of interest to identify and reconstruct candidate jets using iteration processes. It is the algorithm that will define the position and total energy of the L2 candidate jet. The total energy is calibrated at the hadronic scale.

3.3.3 Event Filter

The EF trigger is the last stage of the trigger where an event is either rejected or recorded. This stage happens after the Event Builder stage and has access to the entire detector granularity. Due to the rate that the EF has to process, it is possible to process events with almost the same level of detail as in offline, which is the event processing after the recording procedure.

The EF is a process with three stages. These are the data preparation, followed by a jet reconstruction procedure and the hypothesis testing defined in the trigger menu. These stages are shown in Fig. 3.3

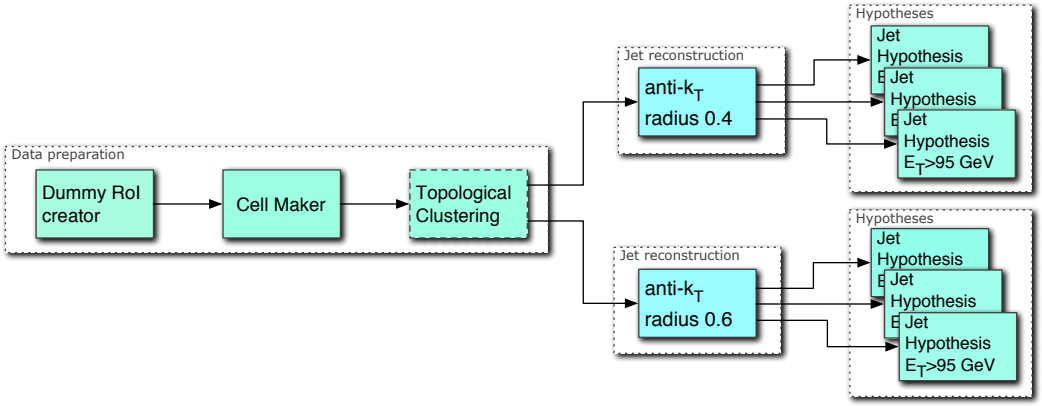

FIGURE 3.3: Schematic diagram of the Event Filter system modules. In the example are shown two physics signatures to select candidate jets with radius 0.4 and 0.6, on which will be tested several transverse energy conditions.

The data preparation module retrieves the data of all calorimeter cells into a previously created dummy ROI that considers the entire detector. The next stage comprise a clustering algorithm defined in the trigger configuration stage. In p+Pb

data-taking period, two algorithms were used in the stage of jet reconstruction, the anti-kt algorithm with and without underlying event subtraction, both with a R = 0.4 parameter. The reconstruction algorithm procedure is similar to the ones described in Appendix B.

The jets defined are ordered in transverse energy, which is the measured jet energy projected in the transverse plane of the collision axis, and stored in cache. An hypothesis algorithm runs over the jets and selects all the jets that match the defined criteria for every different threshold in a single inclusive jet trigger. This hypothesis algorithm takes as input parameters: the required jet multiplicity, pseudorapidity cuts, and the energy thresholds which the triggered jets must match. This means that not only single inclusive jet triggers can be defined but also multi-jet trigger signatures with asymmetric thresholds or some event topology.

3.4 Jet trigger menu for the 2013 p+Pb runs

The trigger menu is composed of *trigger chains*, their configurations and prescale factors. Each trigger chain usually has several requirements on the three levels of trigger decision, tighter thresholds to pass and different prescale values, among others. Some trigger chains run in *pass-through* mode at L1 or L2, in which independently of the trigger decision on that stage the event is recorded. The next paragraphs describe the nomenclature used to define the jet trigger menu, which is presented in Tab. 3.1.

Different classes of triggers compose the three trigger stages in the trigger menu. These classes can be:

- *Single object triggers* select events with at least one object of interest. In particular, an event with one or more jets of at least 20 GeV in transverse energy E_T, is defined as *j20* in the menu.
- *Multiple object triggers* select events with N characteristic objects of the same type. For example 3 jets above 20 GeV of transverse energy are defined as *3j20*.

- *Combined triggers* select events with several characteristic objects of different types. For example 1 jet of 20 GeV of E_T and a summed energy on both forward calorimeters above 90 GeV of transverse energy is defined as *j20_te90*.

- *Topological triggers* are used to select events based topological information from two or more objects. For example a η minimum distance of 4.0 units between two jets of at least 20 GeV of E_T is defined as *2j20_deta40*.

When referring to a particular level of a trigger, the level (L1, L2 or EF) appears as a prefix. Regarding the Minimum Bias Trigger Scintillator (MBTS) trigger, events can be triggered by `L1_MBTS_N` which requires that at least N hits were detected in one of the MBTS detector sides. In its turn `L1_MBTS_N_N` requires that N hits were detected on both sides of the MBTS detector. Another type of trigger used during the 2013 p+Pb run was the `L1_TE90` trigger. This trigger selects events with more than 90 GeV of E_T measured in both sides of the forward calorimeter.

The EF trigger stage allows the configuration of jet algorithm reconstruction: *a4hi* defines a jet reconstructed using the anti-kt algorithm of radius $R = 0.4$ with calorimeter towers as input signal and underlying event subtracted. *a4tchad* defines the use of the anti-kt algorithm using topological cell energy clusters as signal input with a radius of R=0.4. Both jet algorithms are calibrated at the hadronic energy scale. Notice that there is no *a4tchad* defined in the Tab. 3.1. By selecting the appropriate sets of data in which the *a4tchad* was configured in the menu, one can emulate the same Jet Trigger Menu for the *a4tchad*, and study it.

Moreover, forward jets are reconstructed in the $3.2 < |\eta| < 4.9$ region of the detector and their name convention is *fjxx* or *FJXX* when the jets are reconstructed at the HLT or the L1 trigger, respectively. *L1FJ0* describes an event with at least a L1 jet with a E_T above 0 GeV.

The EF trigger stage has the possibility of having η-space requirements within two reconstructed jets. *deta40* triggers events in which two or more jets are reconstructed with at least 4.0 units of pseudorapidity. *eta50* is the name code for considering all jets within the ATLAS calorimeter, and not only the ones reconstructed in the central region, $|\eta| < 3.2$. Finally, *EFFS*, is an acronym for Event

Filter Full Scan, which allows in the EF trigger stage a *full scan* approach considering the entire hadronic calorimeter as one ROI in which the jet algorithms will process the energy signals. In this way, the ROIs position defined at L1 are disregarded and the EF will reprocess the whole event regardless of the specific L1 jet that triggered it.

Group	Level 1	Level 2	Event Filter
1	L1_MBTS_1_1	L2_mbMbts_1_1	EF_j20_a4hi_EFFS_L2mbMbts
	L1_MBTS_1_1	L2_mbMbts_1_1	EF_j30_a4hi_EFFS_L2mbMbts
	L1_MBTS_1_1	L2_mbMbts_1_1	EF_j40_a4hi_EFFS_L2mbMbts
	L1_MBTS_1_1	L2_mbMbts_1_1	EF_j50_a4hi_EFFS_L2mbMbts
2	L1_J10	L2_L1J10_NoAlg	EF_j50_a4hi_EFFS_L1J10
	L1_J15	L2_L1J15_NoAlg	EF_j60_a4hi_EFFS_L1J15
	L1_J15	L2_L1J15_NoAlg	EF_j75_a4hi_EFFS_L1J15
	L1_J15	L2_L1J15_NoAlg	EF_j80_a4hi_EFFS_L1J15
	L1_J15	L2_L1J15_NoAlg	EF_j90_a4hi_EFFS_L1J15
3	L1_FJ0	L2_L1FJ0_NoAlg	EF_fj15_a4hi_EFFS_L1FJ0
4	L1_MBTS_1_1	L2_mbMbts_1_1	EF_2j20_a4hi_EFFS_L2mbMbts
	L1_TE90	L2_L1TE90_NoAlg	EF_2j10_a4hi_EFFS_L1TE90
	L1_MBTS_1_1	L2_mbMbts_1_1	EF_2j10_a4hi_deta40_L2mbMbts
	L1_MBTS_1_1	L2_mbMbts_1_1	EF_2j10_a4hi_eta50_deta40_L2mbMbts

TABLE 3.1: List of triggers performing jet selection and global event properties at each trigger level for the 2013 p+Pb run.

The single-inclusive, multi-jet and forward jet trigger chains used for the 2013 p+Pb runs are listed in Table 3.1. Trigger jets at EF seeded by a `L1_MBTS_1_1` trigger constitute the first group. In the second group a L1 jet with 10 or 15 GeV threshold is required. The third group consists of a forward jet trigger and the last group dijet triggers with different requirements.

The triggers in the first group are said to be seeded by an orthogonal trigger method while those in the second group are said to be seeded by a bootstrap method. For high transverse energy jets it is wise to select L1 triggered jet events in order to avoid consuming the bandwidth with events that have low E_T jets.

The L2 jet trigger ran in pass-through in this trigger configuration, and thus the encode name *NoAlg* appended next to some L2 trigger chains means that no algorithm was applied in that trigger stage. *L2mbMbts* describes a trigger with *L1_MBTS_1_1* prescales from both L1 and L2.

Chapter 4

Analysis

In this chapter is discussed the performance metrics and studies used to assess the jet trigger system depicted in the previous chapter.

4.1 Event Selection

The 2013 p+Pb run is separated in two different periods, since 21^{st} of January until February 2^{nd} - denoted period A, and continued from the 2^{nd} to the 10^{th} of February 2013 - referred as period B. In the first period, $^{208}\mathrm{Pb}_{82}$ ions with an energy of 1.57 TeV/nucleon were injected in beam pipe 1, while in 4 TeV protons were injected in beam pipe 2. In period A, the lead remnants were detected on the $\eta > 0$, which is denoted as 'Pb going side', while 'p going side' is referred to $\eta < 0$. In period B, the beam types were inverted, i.e. the lead ions circulated on beam pipe 2 and the protons on beam pipe 1, maintaining the respective energies. Both periods had the same center of mass energy per nucleon pair of $\sqrt{s_{NN}} \approx 2\,E_p\sqrt{\frac{Z_{Pb}Z_p}{A_{Pb}A_p}} = 5.02$ TeV. Such an asymmetric collision system implies a rapidity shift of -0.465 (0.465) units relative to the ATLAS rest frame, in period A (B).

The cumulative luminosities as a function of time delivered by the LHC and recorded by ATLAS are shown in Fig. 4.1. A total integrated luminosity of 29.85 nb^{-1} was recorded by ATLAS while the LHC delivered 31.23 nb^{-1}. As consequence of the trigger evolution, for the optimal set of triggers, period B has approximately

twice as much data when compared to period A. A total of 17 μb^{-1} of data were recorded in the Minimum Bias data stream.

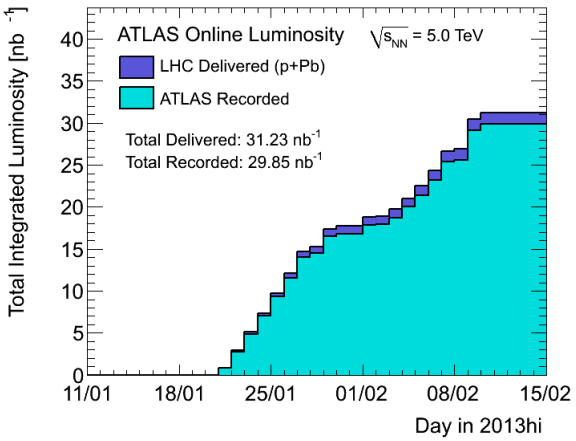

FIGURE 4.1: Integrated luminosity for the proton-lead run as a function of time.

The offline event selection is performed requiring that the whole detector worked in proper conditions. This task is accomplished with the beam conditions monitor[1] (BCM) along with the Data Quality (DQ) information, being the output result the Good Runs List (GRL). This list flags the status of the subdetectors of ATLAS for physics analysis by the unit of time for data-taking, the luminosity block.

In order to guarantee a physics signature consistent with inelastic p+Pb collisions, the following event selection was applied in the Minimum Bias data stream:

1. Official Good Runs List;
2. Two hits above a defined energy threshold, one on each side of the Minimum Bias Trigger Scintillator, selected by L1_MBTS_1_1 trigger;
3. A time requirement between hits on both sides of the MBTS of $|\Delta t_{MBTS}| < 10$ ns;
4. At least one reconstructed primary vertex by the Inner Detector, but no more than one with p_T sum of the tracks that define it greater than $\Sigma p_T^{trk} > 6$ GeV;

[1] An ATLAS subdetector that provides information about the instantaneous collision rate and sends information to the accelerator operators about conditions near the interaction point.

5. At least two tracks in the event which pass the Minimum Bias tracking cuts. These cuts are defined in Appendix C;

6. A η gap smaller than 2.0 measured on the lead going side, between the edge of the detector and the nearest particle with a $p_T > 200$ MeV.

These are the offline reference event selection cuts. They not only aim to reject non-collision background and cosmic events, but also multiple inelastic collisions in the same bunch crossing (cut number 4.), also known as in-time pile-up[2].

Event cuts	Event survival fraction
Raw	1
(1.) GRL	0.94106
(2.) MBTS_1_1	0.44122
(3.) $\lvert\Delta t_{MBTS}\rvert < 10$ ns	0.43989
(4.) Vertex cuts	0.43409
(5.) Tracking cuts	0.43390
(6.) η gap	0.43389

TABLE 4.1: The six event selection cuts that aim to reject bad events from the Minimum Bias data stream. The column *event survival fraction* represents the summed fraction of events that passed the previous cuts with respect to the Minimum Bias data stream, which is represented by *Raw*.

Tab. 4.1 shows the summed event survival fraction with respect to the minimum bias data stream. The event cut number 5 *tracking cuts* consists on the fraction of events that passed the event cuts 1-5 with respect to the MB stream. The event cut number 2 `MBTS_1_1` is the most significant cut.

4.1.1 Centrality definition

The variable used to characterize the centrality of a collision is the summed forward calorimeter transverse energy on the Pb going side, calibrated at the hadronic scale, and is represented by $\Sigma E_T^{Fcal,Pb}$. The purpose in choosing this variable, restricted to the forward calorimeter, is to avoid biasing the measurement with

[2]In the 2013 data taking conditions, the expected pile up amounts to $\mu \approx 10^{-1}$.

the transverse energy of jets which are higher at central η. The selection of the Pb going side is most sensitive to the nuclear geometry of the collision.

In addition to the total inelastic cross-section of p+Pb collisions, diffractive events also contribute to the total cross-section. Diffractive events involve no colour flow between partons, but there is a colour singlet exchange, described in Regge theory as a Pomeron[20]. The diffractive dissociation measured in these collisions can be of the nucleus, the proton and other rare events. The diffractive dissociation of the proton is identified with a large η gap in the nucleus going direction. This pseudorapidity gap is measured between the edge of the detector and the nearest particle with a $p_T > 200$ MeV. This type of events does not deposit any energy on the FCal Pb going side and therefore cannot be mapped to a particular N_{part} value. A centrality class cannot be attributed to these events. For this reason, these events are not considered (cut number 6 in the offline selection).

The measured energy on $\Sigma E_T^{Fcal,Pb}$ is corrected offline for: the underlying electronic pedestal and noise which are measured from empty events; the energy scale difference measured between Period A and B; the vertex-dependence of the $\Sigma E_T^{Fcal,Pb}$ (the mean of this value was observed to decrease when the vertex position was closer to the FCal Pb going side, due to the overall scale of the $\Sigma E_T^{Fcal,Pb}$). There is also an energy contribution from jets to the measured FCal Pb going side energy which can bias the centrality class. In this analysis, this contribution is subtracted from the energy of $\Sigma E_T^{Fcal,Pb}$ by selecting $E_T^{EM} > 8$ GeV jets of R=0.6 with underlying event subtraction and removing the electromagnetic calibrated energy of the towers which overlap to those of the FCal calorimeter Pb going side. This procedure is executed before the energy corrections that were mentioned previously. All the procedures and corrections to the centrality determination are presented in [8].

The distributions of $\Sigma E_T^{Fcal,Pb}$ with and without the offline event selection are presented in Fig. 4.2. The raw logarithmic distribution with no offline selection cuts shows a bump near $\Sigma E_T^{Fcal} \approx 90$ GeV which is caused by the `L1_TE90` trigger. The offline event selection, described in Sec. 4.1, removes this effect providing $\Sigma E_T^{Fcal,Pb}$ event distribution that will be mapped to the N_{part} distribution of the Glauber Monte Carlo Model. The N_{part} distribution is fitted to data considering a 98% of total efficiency of the Glauber inelastic events[8].

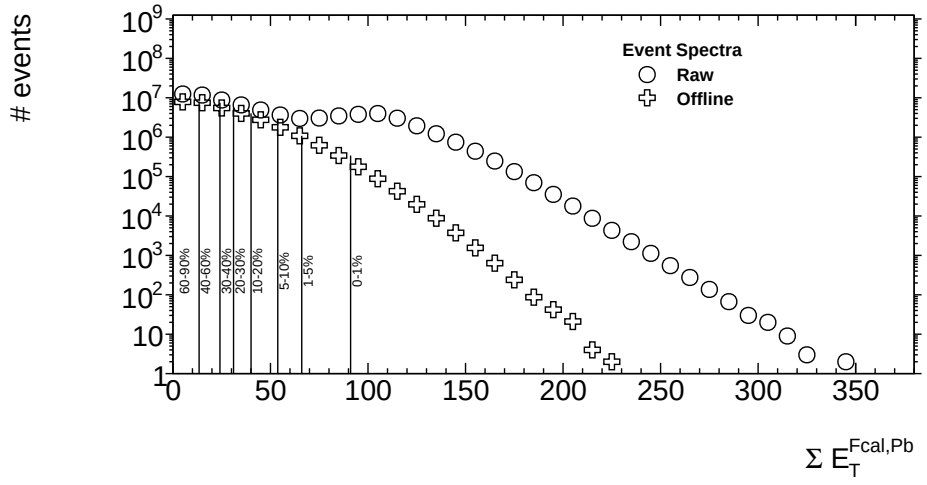

FIGURE 4.2: The $\Sigma E_T^{Fcal,Pb}$ event distribution is presented without (*Raw*) and with (*Offline*) the offline event selection. The vertical lines define different centrality classes.

The most peripheral centile considered is the 90% and there are two reasons to support this decision. The determination of their N_{part} values suffers from a large systematic uncertainty due to the uncertainty in the total efficiency. Also selecting such low $\Sigma E_T^{Fcal,Pb}$ events preferentially selects p+p like events but with a suppressed multiplicity of produced particles and soft underlying event, which biases the events. The vertical lines in Fig. 4.2 separate the $\Sigma E_T^{Fcal,Pb}$distribution in different classes of centrality. Tab. 4.2 shows the definition of centrality ranges using the Glauber Monte Carlo model described in Sec. 1.3.2 for the p+Pb collision type. For more information regarding the centrality determination see [8].

4.2 Offline jet selection

Not all offline jets are considered for the physics analysis. Jets can be classified in three categories: the good, the bad and the ugly. Ugly jets are characterized by being reconstructed in parts of the calorimeter that don't perform as expected (e.g. dead cells and the transition region between the hadronic barrel and the hadronic end-cap). Bad jets are those not associated with real energy deposits in the calorimeter, but commonly associated with out-of-time background events (e.g. non-collision backgrounds or cosmic-ray showers, energy spikes in the hadronic end-caps or coherent noise from the electromagnetic calorimeter). Good jets are those which are not ugly neither bad. These are the jets used in physics analysis

Centrality class	high E_T edge (GeV)	low E_T edge (GeV)	N_{part} (low)
00-01%	∞	91.08	$18.3\ ^{+18.8\%}_{-8.3\%}$
01-05%	91.08	66.03	$16.6\ ^{+14.1\%}_{-8.7\%}$
05-10%	66.03	53.74	$15.6\ ^{+12.5\%}_{-8.8\%}$
10-20%	53.74	40.04	$15.6\ ^{+9.5\%}_{-9.1\%}$
20-30%	40.04	31.07	$11.4\ ^{+9.1\%}_{-9.1\%}$
30-40%	31.07	24.10	$9.79\ ^{+8.9\%}_{-9.4\%}$
40-60%	24.10	13.41	$7.42\ ^{+8.6\%}_{-10.1\%}$
60-90%	13.41	2.555	$4.06\ ^{+6.4\%}_{-9.9\%}$

TABLE 4.2: Definition of the centrality classes. The summed energy of the lead going side in the forward calorimeter, $\Sigma E_T^{Fcal,Pb}$, is the value which is used to define the centrality class of a collision. If an event has $\Sigma E_T^{Fcal,Pb}$= 60 GeV, its centrality class is the 05-10%.

and to make performance studies. Appendix C shows the selection cuts to discard bad and ugly jets.

The bidimensional spectra of jets as a function of the E_T and η with offline event selection and jet quality cuts for the most 0-10% central collision events are shown in Fig. 4.3(a) and 4.3(c) for period A and B, respectively. The most peripheral collision events, with a centrality class of 60-90%, are displayed in Fig. 4.3(b) and 4.3(d) for period A and B.

These distributions are dependent on pseudorapidity, on transverse energy and in period. Most of the jets are detected in the η-central part of the detector, and the transverse energy is itself a function of the jet pseudorapidity. The difference from period A and B reflects only the shift of the asymmetric collision.

4.3 Performance Metrics

To perform an evaluation of the different triggers chains that define the jet trigger menu, several performance metrics must be defined. These performance metrics are defined relatively to specific criteria: the selection of events, the object selection and the matching criterion, defined hereafter.

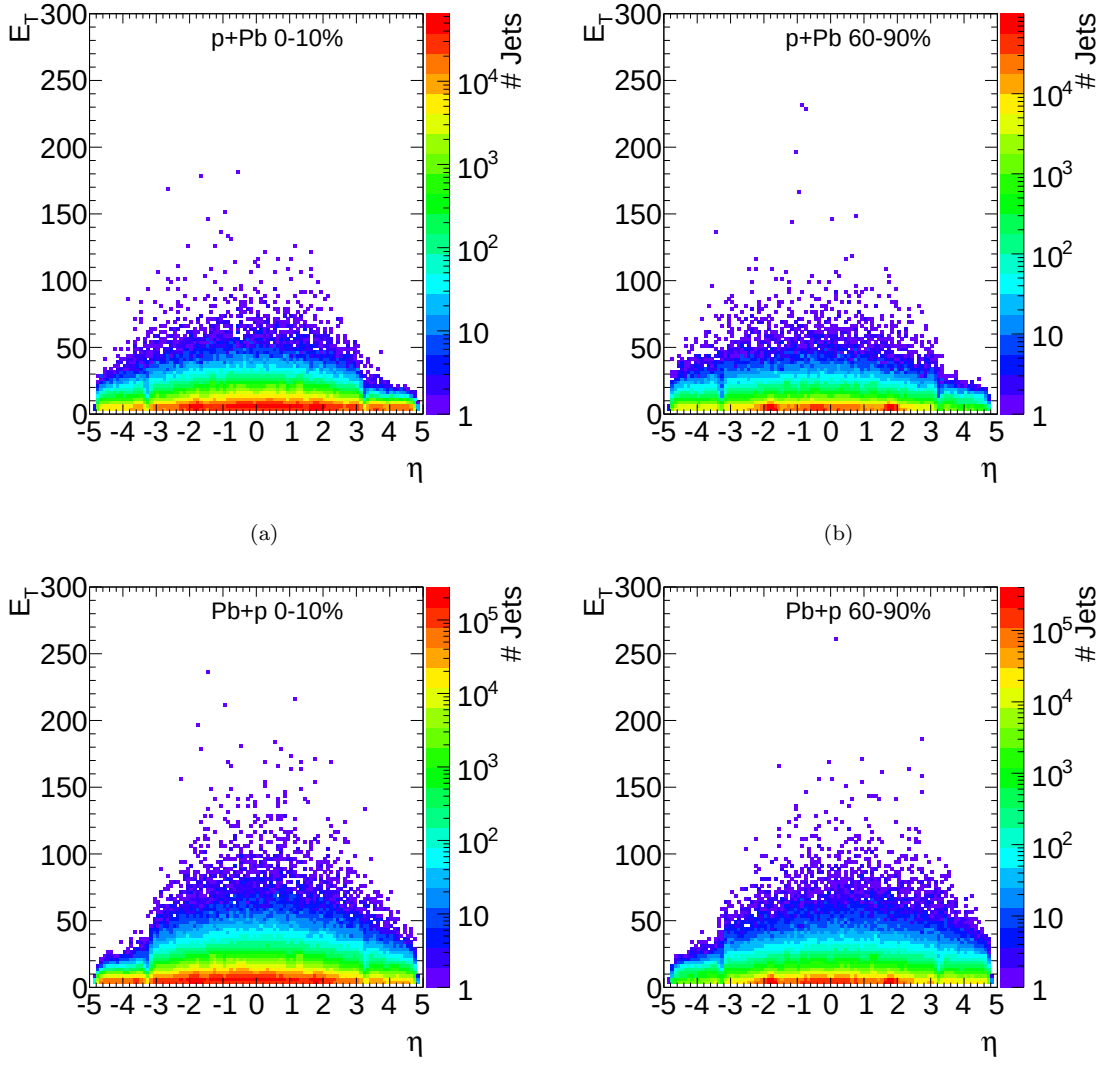

(a) (b)

(c) (d)

FIGURE 4.3: The bi-dimensional spectra of jets as a function of the transverse energy (y-axis) and pseudorapidity (x-axis) with offline event selection and jet quality cuts. Jets produced in the most 0-10% central collision events are shown in Fig. 4.3(a) and in the most 60-90% peripheral collision events are displayed in Fig. 4.3(b) for period A (p+Pb). The same jet spectra is also presented for period B (Pb+p) in Fig. 4.3(c) and 4.3(b) for the same centrality classes.

The reference sample of events is obtained using the event selection defined in Sec. 4.1 from the Minimum Bias data stream. The objects of reference for jet trigger assessments are the offline jets. These are defined as jets reconstructed by the anti-k$_T$ algorithm with an R parameter of 0.4, with underlying event subtraction and calibrated at the hadronic scale. These jets are also required not to be identified as being neither bad nor ugly. Online jets are L1 jets reconstructed by the L1 trigger system (see Sec. 3.3.1) or jets identified by the Event Filter Jet Trigger system. The later uses the same algorithm as offline jets (Sec. 3.3.3).

Offline jets match online jets if the following requirements are fulfilled:

- The online jet has a transverse energy greater than the corresponding threshold of the assessed trigger defined in the jet trigger menu;
- A distance $\Delta R \equiv \sqrt{(\eta_{online} - \eta_{offline})^2 + (\phi_{online} - \phi_{offline})^2}$ less than 0.4 is measured between the two jets;

η_{online} ($\eta_{offline}$) is the η coordinate of the online (offline) jet. ϕ_{online} and $\phi_{offline}$ stands for the ϕ coordinate of the online and offline jets, respectively. If more than one online jet have these required properties, the closest one to the offline jet is selected.

For assessing the performance of the Level 1 trigger, the offline jets are separated in two groups; central jets characterized by $|\eta_{offline}| < 3.2$, and forward jets measured in the $3.2 \leq |\eta_{offline}| < 4.9$. In the central region the standard matching cut described above is used, while in the forward region the matching criteria is $\Delta R \equiv |\phi_{online} - \phi_{offline}| < 0.4$. This separation is motivated by the different η segmentation at L1 (see Sec. 3.3.1).

Several distributions of the ΔR variable between an offline jet and the closest online jet are depicted in Fig. 4.4(a), 4.4(b) and 4.4(c). All distributions are normalized to the total number of jets. Fig 4.4(a) shows the ΔR distribution between the offline jets and online jets, for the `L1J10`, `L1J15` and `L1FJ0` jet triggers. The ΔR distributions for the `L1J10` and `L1J15` triggers show a maximum value close to 0.1 and a minimum close to 0.25. ΔR is a radial quantity with non-zero resolution, hence the maximum at 0.1. On the other hand, the ΔR distribution of `L1FJ0` trigger shows a different behaviour from the other two, which is explained by the different matching criteria applied and calorimeter segmentation at L1.

Fig. 4.4(b) presents the ΔR distribution between the offline jets and EF jets using the orthogonal `L2_mbMBTS` trigger as seed for the `EF_j20_a4hi_EFFS_L2mbMBTS`, `EF_j40_a4hi_EFFS_L2mbMBTS` and the `EF_fj15_a4hi_EFFS_L1FJ0` trigger chains. On contrary to L1, the η segmentation in the EF is the same as offline. The ΔR distributions that use `L2_mbMBTS` as seed follow a same pattern at $\Delta R \approx 0$ and $\Delta R \geq 0.3$. At ΔR close to zero the jets are reconstructed closely to each other which is expected given the similar jet reconstruction algorithm and calibration, hence the maximum close to zero. One can also notice that the distributions are steeper for the higher energy threshold trigger. The second pattern of this distribution, $\Delta R \geq 0.3$, suggests that it was detected an online jet close to the offline but may not be related. The ΔR distribution of the `EF_fj15_a4hi_EFFS_L1FJ0` trigger chain follows the same pattern at low ΔR, similar to the patterns described. At high ΔR this distribution is different due to the limited region of the offline jet phase space considered ($\eta^{offline} > 3.2$).

Fig 4.4(c) depicts the ΔR distribution between the offline jets and EF jets using the triggers `L1J10` and `L1J15` as a 'bootstrap' method to the higher threshold triggers `EF_j50_a4hi_EFFS_L1J10`, `EF_j75_a4hi_EFFS_L1J15` and `EF_j90_a4hi_EFFS_L1J15`. The same patterns that are observed in Fig. 4.4(b) are also observed in Fig 4.4(c).

As expected the ΔR distributions between the EF and offline jets have a closer relation when compared to the ones involving L1 jets. The simplicity of the L1 jet reconstruction algorithm when compared to the EF algorithm is the main reason of this discrepancy. The latency of the EF is high enough to process an event which allow a jet reconstruction algorithm closely related to the one used offline.

All jets that define the distributions shown in these figures within $|\Delta R| < 0.4$ are the ones which will be selected to study these triggers.

The jet trigger efficiency (ϵ_{trig}) is defined as:

$$\epsilon_{\text{trig}} = \frac{\#\text{ jets passing(offline selection } \wedge \texttt{triggerselection})}{\#\text{ jets passing (offline selection)}} \tag{4.1}$$

where '# jets passing (offline selection)' is the set of offline jets that survive the reference event selection. '# jets passing(offline selection $\wedge$ `triggerselection`)' is the collection of offline jets that match an online jet fulfilling the requirements of the two matching criteria. Jet trigger efficiencies are studied as a function of the

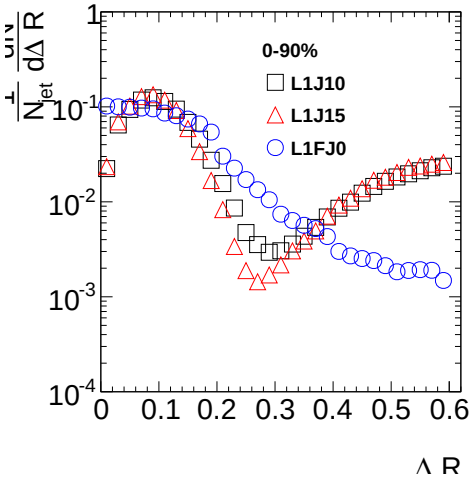

(a)

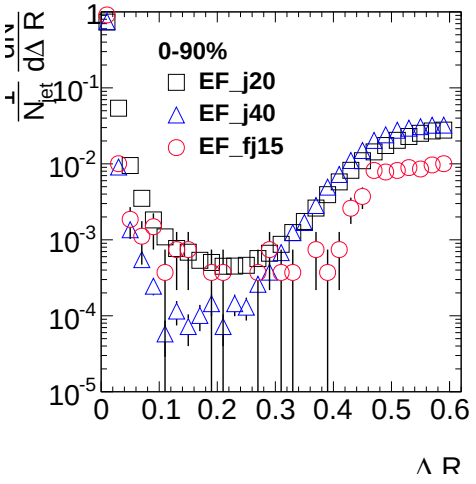

(b)

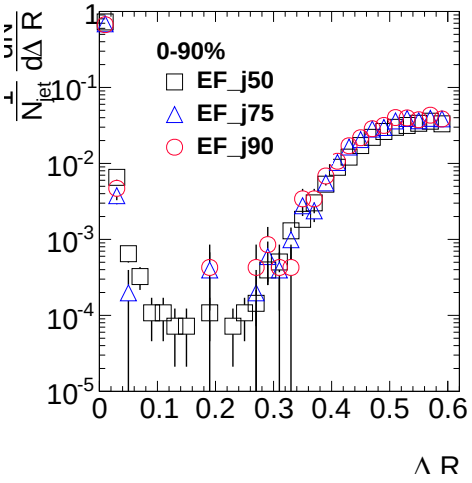

(c)

FIGURE 4.4: ΔR distributions for the 0-90% centrality class. Fig. 4.4(a) shows the ΔR distribution between offline jets and L1 jets `L1J10`, `L1J15` and `L1FJ0`. The same distributions between the offline jets and EF jets selected by the `EF_j20_a4hi_EFFS_L2mbMBTS` (`EF_j20`), `EF_j40_a4hi_EFFS_L2mbMBTS` (`EF_j40`) and `EF_fj15_a4hi_EFFS_L1FJ0` (EF_fj15) trigger chains are presented in Fig. 4.4(b). Fig. 4.4(c) depicts the ΔR distributions between the offline jets and EF jets triggered by the `EF_j50_a4hi_EFFS_L1J10` (`EF_j50`), `EF_j75_a4hi_EFFS_L1J15` (`EF_j75`) and `EF_j90_a4hi_EFFS_L1J15` (`EF_j90`) trigger chains.

offline jet E_T. One can perceive the efficiency variable as a quantitative measurement of the trigger reconstruction algorithm to correctly identify and reconstruct the required object. With perfect and same reconstruction conditions at both online and offline, one would expect the jet trigger efficiency as a function of the offline jet E_T to be a step function with the same transition point as the trigger

threshold considered.

The jet trigger purity (P_{trig}) is defined as:

$$P_{\text{trig}} = \frac{\#\text{ jets passing}(\texttt{triggerselection} \wedge \text{ offline selection})}{\#\text{ jets passing }(\texttt{triggerselection})} \tag{4.2}$$

where '# jets passing (`triggerselection`)' is the collection of online jets that fulfill the threshold condition of the assessed trigger, while '# jets passing (`triggerselection` $\wedge$ offline selection)' is the same collection of online jets that match an offline jet. Jet trigger purities are studied as a function of the online jet E_T. In some cases of the purity variable E_T is integrated. A trigger purity can be regarded as the rejection power of a given trigger chain by discarding events that do not meet the required properties. With perfect and same reconstruction conditions both online and offline, one would expect the jet trigger purity as a function of the online jet E_T to be a constant function at y = 1 starting from the threshold energy.

Both the efficiency and purity variables can be represented by a Binomial distribution. In some cases the statistical uncertainty of these distributions give unexpected results. In order to calculate correctly the statistical uncertainties of these variables it is used the Bayes theorem (see Appendix D).

The single inclusive jet trigger performance metrics are considered as per jet measurements. Multi-jet triggers and global event trigger chains are considered as per event measurements.

Other performance metrics used in the study of the ATLAS Jet Trigger for the p+Pb run include the relative jet transverse energy scale (JES), jet transverse energy resolution (JER), η and ϕ position resolutions. The JES is defined as the mean value of the $\frac{E_T^{\text{online}} - E_T^{\text{Offline}}}{E_T^{\text{Offline}}}$ distribution, whereas the JER is its RMS. Both JES and JER are studied as a function of transverse energy of the offline jet. The position resolution measurements are defined as $\Delta\eta \equiv \eta^{\text{offline}} - \eta^{\text{online}}$ and $\Delta\phi \equiv \phi^{\text{offline}} - \phi^{\text{online}}$ distributions.

4.4 Level 1 trigger performance

The performance of the L1 triggers used in the Jet Trigger menu is assessed. The L1 trigger chains defined in the trigger menu are the first to select the final state objects produced in p+Pb collisions that will be recorded ultimately by the TDAQ system. The next sections show studies on L1 global event triggers, the L1 Jet triggers and L1 Forward Jet triggers, followed by a more detailed performance study on L1 jet triggers with jet trigger efficiency, jet trigger purity, jet energy scale and resolution. For other performance studies on global event L1 triggers see [21]. Due to the Full Scan property of the EF, it is only required at L1 an accept decision to activate the jet trigger at the EF. For this reason the position resolution at L1 is not studied in this analysis.

4.4.1 Global event triggers

4.4.1.1 mbSpTrk trigger performance

The mbSpTrk trigger chain is used to study the performance of global event triggers such as the `L1_MBTS_1_1` or the `L1_TE90`. Its goal is to carry out unbiased performance studies to other trigger chains. The performance study of both triggers is presented in Ref. [21] and is exposed here due to their relevance in this analysis.

The mbSpTrk trigger chain is defined at L1 by a prescaled random trigger which selects randomly events from filled bunches, the `L1_RD0_FILLED` trigger chain. At L2 the mbSpTrk requires at least 2 pixel hits and 3 hits on the semi-conductor tracker at the Inner Detector. At the EF is required a track of $p_T > 200$ MeV.

Using the Minimum Bias data stream one can obtain an unbiased event sample with the `L1_RD0_FILLED` trigger. However about 95% of these events are empty events in which no inelastic interaction occurred. The mbSpTrk at HLT aims to discard part of the empty events which are of no use in performance studies. Knowing that this trigger chain is heavily prescaled at L1, with 95% of empty events results in an even smaller sample to assess.

The event sample of `L1_RD0_FILLED` is used to define the mbSpTrk trigger efficiency. The following conditions were used as the offline event selection:

- At least two 'loose' tracks (See Appendix C for definition of 'loose' track);
- A time requirement between hits on both sides of the MBTS of $|\Delta t_{MBTS}| <$ 10 ns, or between the two Liquid Argon calorimeter end caps, when the MBTS trigger is assessed.

The `mbSpTrk` trigger efficiency is defined as:

$$\epsilon_{\text{trig}} = \frac{\#\text{ events passing(offline selection } \wedge \texttt{ mbSpTrk})}{\#\text{ events passing (offline selection)}} \tag{4.3}$$

where 'events passing (offline selection)' is the sample of events that pass the offline event selection cuts defined in this section and 'events passing(offline selection $\wedge$ `mbSpTrk`)' requires the condition of the `mbSpTrk` trigger accept decision in the same event sample.

Fig 4.5 left side shows the trigger efficiency for the `mbSpTrk` trigger chain as a function of number of tracks that characterize the primary vertex (n_{trk}^{PV}) on the left. On the right side, Fig 4.5 depicts the `mbSpTrk` trigger efficiency as a function of the summed transverse energy on the forward calorimeter in the Pb going side, $\Sigma E_T^{Fcal,Pb}$. Notice that this is the same variable used to define the centrality class of a collision.

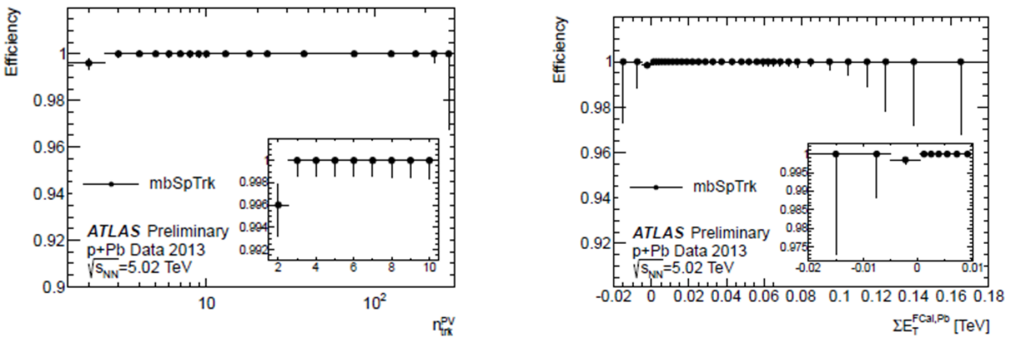

FIGURE 4.5: `mbSpTrk` trigger efficiency as a function of the number of reconstructed tracks in the left figure and as a function of the $\sum E_T^{Pb,Fcal}$ presented in the right figure. The insets show a zoom either into a low-track multiplicity or low $\sum E_T^{Pb,Fcal}$ [21].

The trigger mbSpTrk is 100% efficient for track multiplicity above 2 as can be seen in Fig 4.5 left plot. When considering the first two-track bin there is a

small inefficiency which is cleared if the MBTS timing cut is applied instead of the LAr timing cut. Fig 4.5 right plot shows the mbSpTrk trigger efficiency is 100% efficient for $\Sigma E_T^{Pb,Fcal} > 0$ TeV. The non-physical negative $\Sigma E_T^{Pb,Fcal}$ values are not considered for physics analysis and are caused by electronic noise and out-of-time pile-up [8].

The `mbSpTrk` trigger purity is defined as:

$$P_{\text{trig}} = \frac{\#\text{ events passing}(\texttt{mbSpTrk} \wedge \text{offline selection})}{\#\text{ events passing }(\texttt{mbSpTrk})} \tag{4.4}$$

The trigger purity of the `mbSpTrk` trigger chain is $(87.14 \pm 0.03)\%$[21]. The `L1_RD0_FILLED` trigger chain has a purity of about 3% [21].

4.4.1.2 L1_MBTS and L1_TE90 performance

To construct an unbiased efficiency study for the `L1_MBTS_1_1` the output sample of the mbSpTrk trigger is used. Using the same offline selection as in Sec. 4.4.1.1, the trigger efficiency of `L1_MBTS_1_1` is defined as:

$$\epsilon_{\text{trig}} = \frac{\#\text{ events passing}(\text{offline selection} \wedge \texttt{mbSpTrk} \wedge \texttt{L1\_MBTS\_1\_1})}{\#\text{ events passing }(\text{offline selection} \wedge \texttt{mbSpTrk})} \tag{4.5}$$

The efficiency of the `L1_MBTS_1_1` trigger is estimated as a function of $\Sigma E_T^{Fcal,Pb}$ and is shown in Fig. 4.6(a) for periods A and B. This trigger is fully efficient from $\Sigma E_T^{Fcal,Pb} > 0.03$ TeV. Consequently there is a small inefficiency in selecting events from a centrality class lower than 40%, as the accept decision of this trigger is one of the conditions of the referenced offline event cuts.

The trigger purity of `L1_MBTS_1_1` is defined as:

$$P_{\text{trig}} = \frac{\#\text{ events passing}(\texttt{L1\_MBTS\_1\_1} \wedge \texttt{mbSpTrk} \wedge \text{offline selection})}{\#\text{ events passing }(\texttt{L1\_MBTS\_1\_1} \wedge \texttt{mbSpTrk})} \tag{4.6}$$

where 'events passing (`L1_MBTS_1_1` $\wedge$ `mbSpTrk`)' refers the events that trigger the `L1_MBTS_1_1` and `mbSpTrk`, and '# events passing(`L1_MBTS_1_1` $\wedge$ `mbSpTrk` $\wedge$

offline selection)' also requires the offline selection described previously. The purity for the `L1_MBTS_1_1` trigger is $(38.51 \pm 0.07)\%$ [21]. There are negligible differences between periods A and B.

To summarize, the `L1_MBTS_1_1` trigger has a high efficiency but a low purity. The low purity of the MBTS trigger suggest that, inspite of many events recorded, 61% of those events do not meet the standard requirements of being considered a 'good' event, on the other hand, the high efficiency suggests that the trigger also selects most of the 'good' events. This result points out the *wasted* bandwidth on recording such *bad* events and enhances the importance of the offline event selection.

The `mbSpTrk` event sample and the event selection described in Sec. 4.4.1.1 were used to assess the `L1_TE90` trigger. The `L1_TE90` trigger efficiency is defined as:

$$\epsilon_{\text{trig}} = \frac{\#\text{ events passing(offline selection } \wedge \texttt{ mbSpTrk } \wedge \texttt{ L1\_TE90})}{\#\text{ events passing (offline selection } \wedge \texttt{ mbSpTrk})} \tag{4.7}$$

where 'events passing (offline selection $\wedge$ `mbSpTrk`)' is the sample of events selected by the `mbSpTrk` trigger combined with offline selection. 'events passing(offline selection $\wedge$ `mbSpTrk` $\wedge$ `L1_TE90`)' also requires the accept decision of the `L1_TE90`. This trigger efficiency is estimated as a function of $\Sigma E_T^{Fcal,Pb}$ and is presented in Fig. 4.6(b), separated in periods A (p+Pb) and B (Pb+p).

The turn-on curves start both close to the 90 GeV threshold and saturate near 120 GeV. This difference between the starting point and the saturation point is related to the energy resolution and calibration between offline and L1. This result also shows a slight difference between the two sides of the Forward Calorimeter which is caused by different calibrations at L1.

The trigger purity for the `L1_TE90` is $(100^{+0.0}_{-0.1})\%$. No differences were observed between the two periods [21].

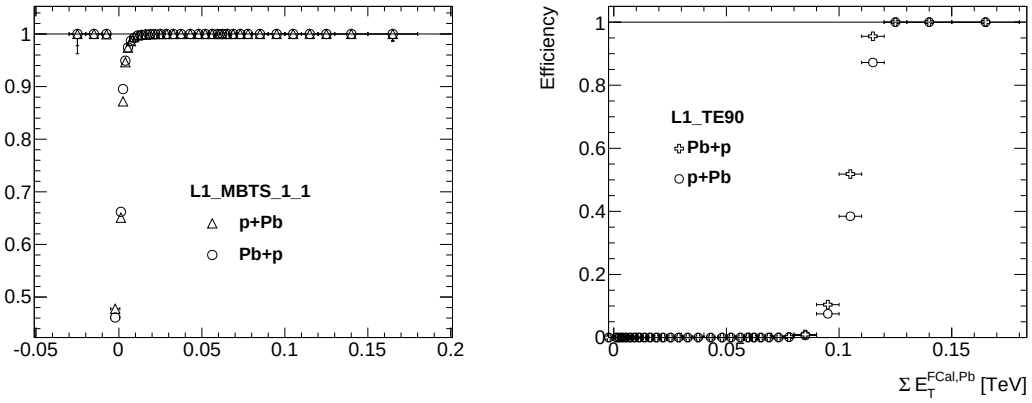

(a) (b)

FIGURE 4.6: Fig. 4.6(a) shows the efficiency of the `L1_MBTS_1_1` trigger as a function of the $\Sigma E_T^{Fcal,Pb}$ for the two periods p+Pb (A) and Pb+p (B). Fig.4.6(b) depicts the efficiency of the trigger `L1_TE90` as a function of the summed transverse energy on the Pb going side, for the two periods [21].

4.4.2 Single-inclusive L1 jet triggers

This section examines the L1 jet triggers used in the Jet Trigger Menu, `L1J10`, `L1J15` and `L1FJ0`. These L1 triggers will be used as seed in order to activate the EF trigger stage. The event sample used is the Minimum Bias data stream and selects events which fulfil the referenced event selection cuts depicted in Sec. 4.1.

As described in Ch. 3, the L1 Jet Trigger is a fast dedicated trigger used to identify jets within a predefined window in the $\eta \times \phi$ space that have a summed energy above a defined threshold. The window used to identify L1 jets is 8×8 with thresholds of 0 GeV, 10 GeV and 15 GeV for triggers `L1FJ0`, `L1J10` and `L1J15`, respectively.

4.4.2.1 Trigger performance of the L1 jet triggers on the η-central region

As mentioned before, in the central region ($|\eta| < 3.2$) there is segmentation both on η and ϕ at the L1 calorimeter trigger level, while in the forward η there is only segmentation on ϕ. This trigger specificity imposes a separate study between central ($|\eta^{offline}| < 3.2$) and forward η ($|\eta^{offline}| > 3.2$), which are defined by different matching criteria. This section will assess the `L1J10` and `L1J15` triggers which are reconstructed in $|\eta| < 3.2$.

The offline jet is matched to the closest L1 online jet that has a E_T above 10 or 15 GeV within the standard $\Delta R < 0.4$. The L1 jet trigger efficiency is defined as:

$$\epsilon_{\text{trig}} = \frac{\#\text{ jets passing(offline selection } \wedge \texttt{ jet E}_\texttt{T}^{\texttt{trig}} > \texttt{X})}{\#\text{ jets passing (offline selection)}} \tag{4.8}$$

where 'offline selection' concerns the referenced offline selection. '$\texttt{jet E}_\texttt{T}^{\texttt{trig}} > \texttt{X}$' selects the offline jets considering the usual matching criteria ensuring that the online jet has at least $X > 10$ or $X > 15$ GeV. The efficiency of `L1J10` and `L1J15` triggers are estimated as a function of the offline jet E_T and are shown separately for periods A and B in Fig. 4.7(a) and Fig. 4.7(b). The differences between the two periods are negligible. All efficiency curves reach the plateau (i.e. > 0.99) beyond some offline jet E_T value and stabilize around that y-value. The plateau is reached at ∼50 (60) GeV for the `L1J10` (`L1J15`) trigger chain. A systematic shift between the `L1J10` and `L1J15` trigger chains is observed. This is the result of requiring different online jet E_T thresholds for these triggers. The efficiency at mid point is not at ${E_T}^{offline}$ of 10 or 15 GeV, as one would expect, because the L1 jets are calibrated at the EM scale and the offline jets at the hadronic scale.

A comparison between the two centrality classes (0-10% and 60-90%) shows that L1 triggers in central collisions are more efficient at the beginning of the turn-on curve. The underlying event plays a role of adding more transverse energy to the jet reconstructed at L1. In peripheral collisions this effect is not visible as little underlying event is deposited in the calorimeter cells.

Focusing now on the Pb+p period, at offline jet E_T close to 75 GeV there is a small inefficiency in peripheral collisions. This feature is observed in one of the thirteen runs that compose period B. The jets that cause this inefficiency are distributed evenly in the $\eta \times \phi$ phase space. Additional jet cleaning cuts don't remove them.

The L1 jet trigger purity is estimated with respect to the offline event selection and is defined as:

$$P_{\text{trig}} = \frac{\#\text{ jets passing}(\texttt{jet E}_\texttt{T}^{\texttt{trig}} > \texttt{X} \wedge \text{ offline jets})}{\#\text{ jets passing } (\texttt{jet E}_\texttt{T}^{\texttt{trig}} > \texttt{X})} \tag{4.9}$$

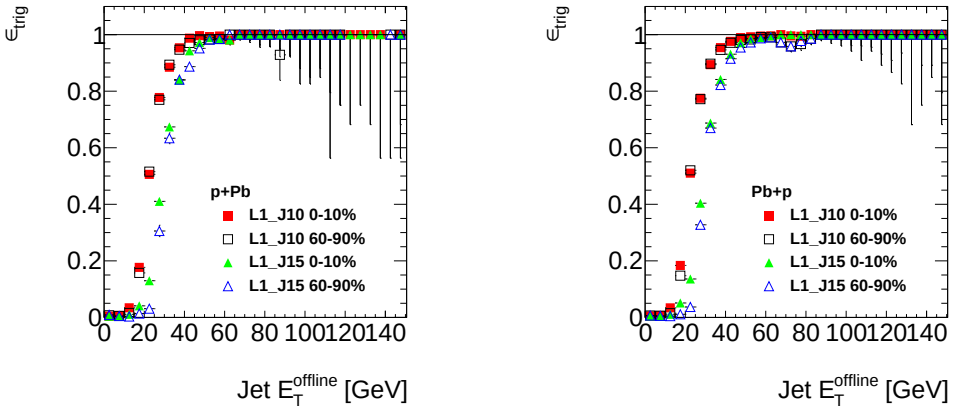

(a) (b)

FIGURE 4.7: The L1 Jet trigger efficiencies for `L1J10` and `L1J15` as a function of the offline jet E_T, are presented in Fig. 4.7(a) for period p+Pb (A) and in Fig. 4.7(b) for period Pb+p (B). Both figures show the two jet trigger efficiencies in different centrality classes, 0-10% and 60-90%.

The presented variables have the same meaning as in the definition of the jet trigger efficiency. The iteration is performed on the online jets that fulfil the E_T requirement of the assessed trigger, matching them to offline jets.

Table 4.3 shows the purity of the `L1J10` and `L1J15` jet triggers integrated in E_T.

Trigger chain	0-10% Purity [%]	60-90% Purity [%]
`L1J10` p+Pb	$98.3^{+0.1}_{-0.1}$	$96.1^{+0.2}_{-0.2}$
`L1J10` Pb+p	$98.22^{+0.05}_{-0.05}$	$96.4^{+0.1}_{-0.1}$
`L1J15` p+Pb	$98.7^{+0.2}_{-0.2}$	$97.1^{+0.3}_{-0.4}$
`L1J15` Pb+p	$98.67^{+0.08}_{-0.08}$	$97.6^{+0.2}_{-0.2}$

TABLE 4.3: Purity of L1 jet triggers presented in different centrality classes and for the two different periods.

The jet trigger purity of the L1 has a good rejection power. Less than 5% of the online jets considered are not identified with an offline jet. The larger E_T threshold required by the L1J15 adds an additional 0.5% of rejection power. A slight difference when comparing central to peripheral centrality class is observed, which suggest that the underlying event conceal fake jets. There is no difference between periods, within the statistical uncertainty.

Fig. 4.8(a) and Fig. 4.8(b) show the jet energy scale and the jet energy resolution for the `L1J10` and `L1J15` trigger chains in central and peripheral centrality classes. Period A and B have been merged has no significant difference between them was observed. The JES has an almost constant value of -0.5, which represent the differences between the L1 and offline calibrations. The JER distributions presented in Fig. 4.8(b) show that the relative energy resolution is at most 0.1. The JES mean result suggest that the E_T of the online jet at the EM scale accounts for half the total transverse energy of the jet.

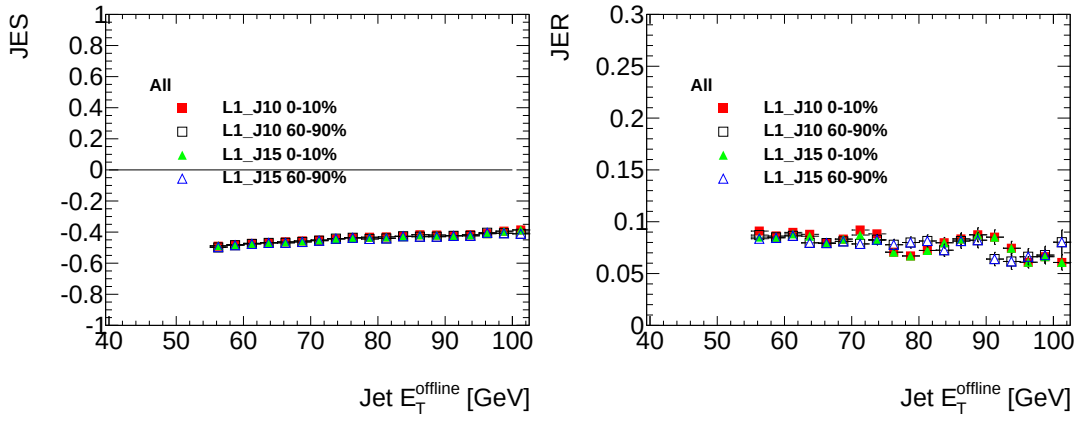

(a) (b)

FIGURE 4.8: Fig. 4.8(a) shows the jet E_T scale of the L1 jets compared to offline jets, while the E_T jet resolution is presented in Fig. 4.8(b).

4.4.2.2 Trigger performance of the L1 jet triggers in the η-forward region

The offline jets used in this performance study are the ones comprehended between $3.2 < |\eta| < 4.9$. As previously discussed, the matching between an offline jet and an L1 trigger jet in this region is modified to simply $\Delta\phi < 0.4$ and requiring that both jets have the same η sign. The jet trigger efficiency of the `L1FJ0` trigger is estimated as a function of the offline jet E_T and is defined as:

$$\epsilon_{\text{trig}} = \frac{\#\text{ jets passing(offline selection } \wedge \texttt{ jet}\,\texttt{E}_\texttt{T}^\texttt{trig} > 0)}{\#\text{ jets passing (offline selection)}} \tag{4.10}$$

The jet trigger efficiencies of the `L1FJ0` trigger chain are shown in Fig. 4.9(a) and Fig. 4.9(b) for periods A and B, respectively. The figures show the jet trigger

efficiency in the 0-10% and 60-90% centrality classes and also in proton going side versus lead going side, as the underlying event is dependent on centrality and pseudorapidity.

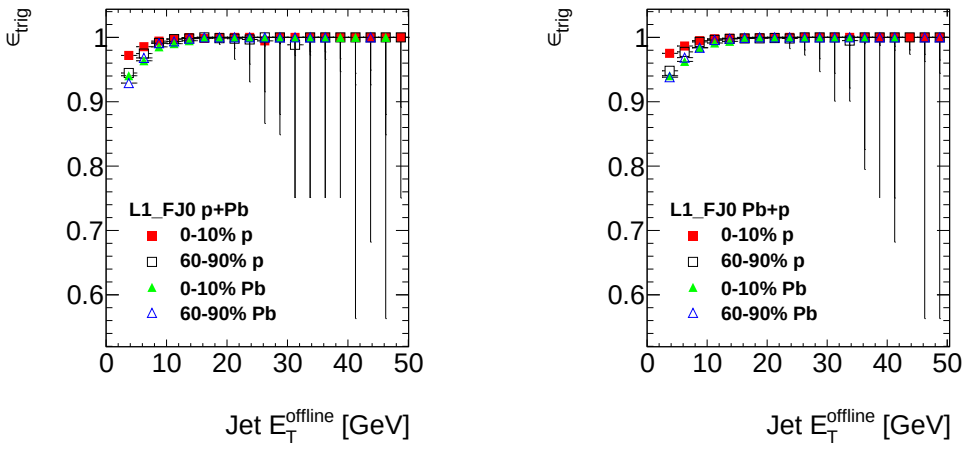

(a) (b)

FIGURE 4.9: The L1 Forward Jet trigger efficiency as a function of the offline jet E_T is shown for period p+Pb (A) in Fig. 4.9(a) and for period Pb+p (B) in Fig. 4.9(b). The jet trigger efficiencies in the 0-10% (60-90%) centrality class is represented by closed(open) markers and on proton (lead) going side by squared (triangular) markers.

All jet trigger efficiencies have always an efficiency above 0.9 and reach the plateau close to 15 GeV. The L1FJ0 expects an online jet with a minimum of 0 GeV while offline jets are selected if their E_T is greater than 4 GeV. There are some minor differences between the triggers turn on, in both periods. The turn on efficiency curve of the 0-10% centrality class in the lead going side is systematically below the other three, by 2% at most.

The jet trigger purity for the `L1FJ0` with the offline event selection is defined as:

$$P_{\text{trig}} = \frac{\#\text{ jets passing}(\texttt{jet}\,\mathrm{E_T^{trig}} > 0 \wedge \text{offline jets})}{\#\text{ jets passing }(\texttt{jet}\,\mathrm{E_T^{trig}} > 0)} \tag{4.11}$$

The jet trigger purity of `L1FJ0` as a function of the online jet E_T is depicted in Fig. 4.10(a) and Fig. 4.10(b) for periods A and B, respectively. Both figures are separated in different centrality classes and in the proton going side versus the lead going side. No significant differences are observed between periods. When comparing centrality classes it is observed significant differences, and even stronger

differences between the proton going side when compared to the lead-going side. This jet trigger has a 0 GeV threshold and not only jets from the hard scattering will trigger the L1FJ0, but also jets reconstructed from the underlying event. This effect is more pronounced when considering central events and the lead going side, which is strikingly more unpure than the other event configurations.

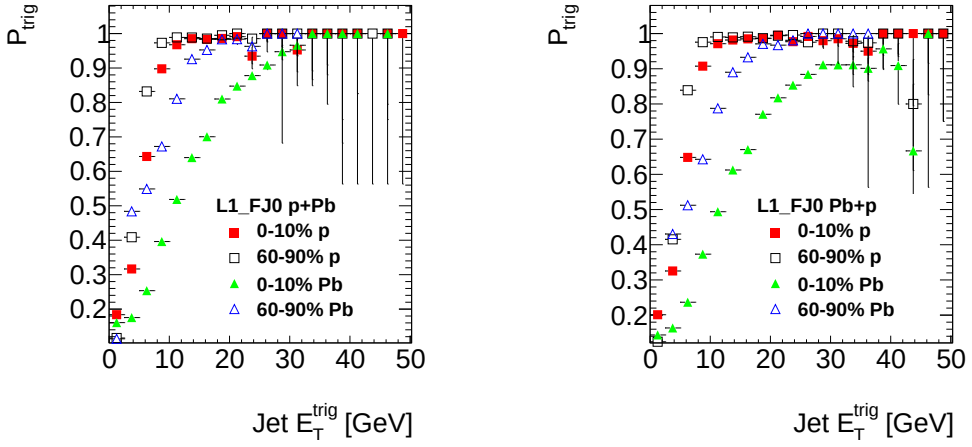

(a) (b)

FIGURE 4.10: The L1 Forward Jet trigger purity as a function of the online jet E_T is shown for period A (p+Pb) in Fig. 4.10(a) and for period B (Pb+p) in Fig. 4.10(b). The 0-10% (60-90%) centrality class is shown with closed(open) markers and on proton (lead) going side with squared (triangular) markers.

The relative JES and JER for this trigger chain are shown in Fig.4.11(a) and Fig. 4.11(b), respectively. To decrease the bias from the efficiency measurement, all of the JES and JER distributions are considered only when the trigger is saturated. There is a large difference between the lead going side in the 0-10% centrality class and other JES distributions. This is due to underlying event, which is not subtracted at L1 and is more pronounced at the lead going side. At high E_T, with the exception of the 0-10% centrality and lead going side, almost all JES distributions converge to a similar value of the η-central jets, -0.5. The JER of this trigger is also susceptible to event configuration. The UE degrades the energy resolution.

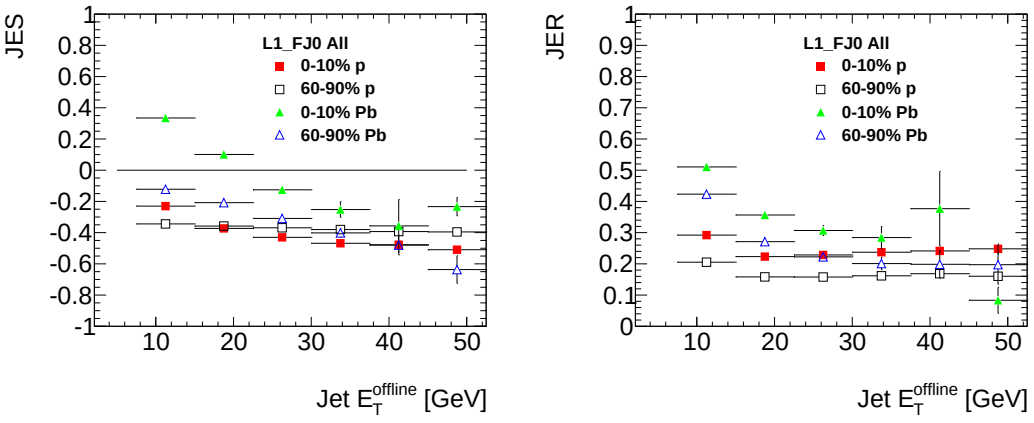

(a) (b)

FIGURE 4.11: Fig. 4.11(a) shows the JES of the `L1FJ0` jet trigger relatively to offline jets, while the JER is shown in Fig. 4.11(b). The squared (triangular) markers represent the proton - p (lead - Pb) going side. The open (closed) markers represent peripheral (central) collision events.

4.5 Event Filter jet trigger performance

In this section is assessed the Event Filter jet trigger which is paramount as this is the last stage before recording an event. First it is discussed the choice of the jet reconstruction algorithm. Follows performance studies on: jet energy scale, resolution in energy and position, efficiencies and purities for the inclusive-single jet and dijet trigger chains.

4.5.1 Comparison between different jet algorithms

In the beginning of the p+Pb run the beam was not always stable as the optimization of the whole LHC and ATLAS apparatus were in process. Only during this period both jet algorithms, with and without underlying event subtraction, were configured in the EF jet trigger system. Due to the beam instability the sets of data from these runs were not GRL approved and only the Express Stream data stream is available. By selecting the luminosity blocks correspondent to stable beam conditions one can perform studies to determine the best algorithm using the same data.

There are two algorithms used by both online and offline jet reconstruction (see Appendix B), one is underlying event subtracted and the other is not. Within each algorithm there are minor differences between online and offline jet reconstruction. For the algorithm without underlying event subtraction, the differences between the online and offline algorithms are the different calibrations that result from the evolution of the offline calibration (the online didn't evolve since its implementation) and the quicker topological cluster formation at online. For the algorithm that subtracts the underlying event contribution, the step 3 of the iteration described in Appendix B is not considered in the online jet reconstruction procedure.

The Express Stream of the first four runs was used with the following event selection:

- A time requirement between hits on both sides of the MBTS of $|\Delta t_{MBTS}| <$ 10 ns;
- Two hits above a defined energy threshold on one of the sides of the Minimum Bias Trigger Scintillator selected by L1_MBTS_2 trigger;

Due to the limited statistics in the sample only the efficiency study of the lowest EF jet triggers is presented. The matching between the offline and the online jet was performed considering the same algorithm. The comparisons of the jet trigger efficiencies between the two algorithms as a function of the offline jet E_T are presented in Fig. 4.12(a) and Fig. 4.12(b).

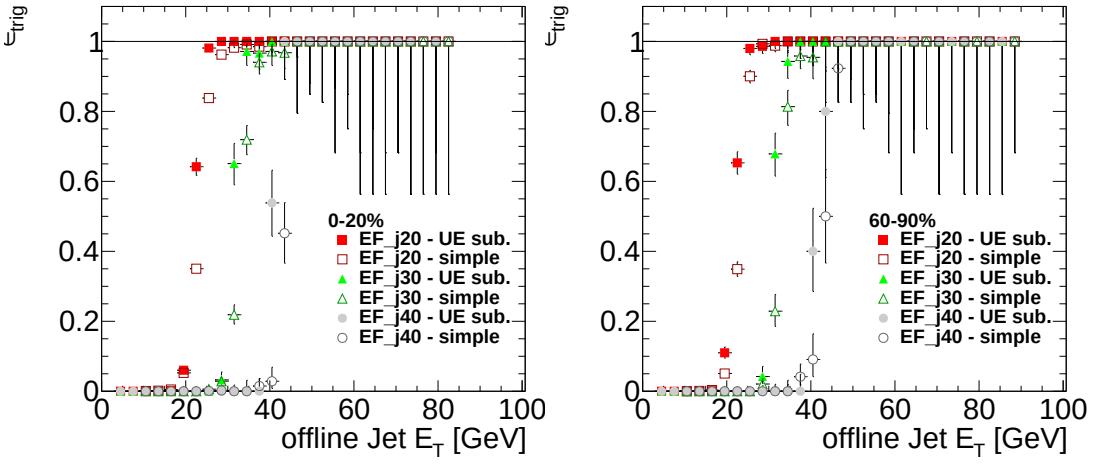

(a) (b)

FIGURE 4.12: Comparison of jet trigger efficiencies between the two jet reconstruction algorithms anti-k$_T$ with (UE sub.) and without (simple) underlying event subtraction, as a function of the offline jet E_T. Fig. 4.12(a) shows the results for the 0-20% centrality class, while Fig. 4.12(b) shows the jet trigger efficiency for the 60-90% centrality class.

Fig. 4.12(a) shows the jet trigger efficiency in the 0-20% centrality class for the `EF_jYY_a4XX_EFFS_L2mbMBTS` where YY stands for 20, 30 and 40 GeV thresholds and XX represents the simple or underlying event subtracted jet algorithm. Fig. 4.12(b) depicts the jet trigger efficiencies for the 60-90% centrality class.

The jet algorithm that performs better considering the same environment is the anti-k$_T$ with underlying event subtraction. The acknowledgement of the underlying event contribution to the jet E$_T$ and its subtraction is the main reason for the differences displayed in both figures despite the slight differences between both offline and online jet reconstructions algorithms. This result motivated a change on the menu from the initially configuration of the simple jet reconstruction algorithm to the underlying event subtracted one.

4.5.2 Transverse energy and angular resolutions and offsets

4.5.2.1 Jet energy scale mean offset and resolution

In this section is discussed the relative jet energy scale (JES) and jet energy resolution (JER) defined in Sec. 4.3. In order to avoid biases from trigger inneficiency the JES and JER are estimated only in the phase space corresponding to full efficiency of the trigger. Only the `EF_j20_a4hi_EFFS_L2mbMBTS` and `EF_fj15_a4hi_EFFS_L1FJ0` trigger chains are discussed as the JES and JER show no dependence on threshold.

Fig. 4.13(a) and 4.13(c) show the JES for the `EF_j20_a4hi_EFFS_L2mbMBTS` trigger for periods A and B. Each JES distribution is separated in two distinct centrality classes, 0-10% and 60-90%, and in three different regions of the η-phase space, $-2.8 < \eta < -0.8$, $|\eta| < 0.8$ and $0.8 < \eta < 2.8$. In period A the lead remnants are collected in $\eta > 0$. The JER is presented in Fig.4.13(b) for period A and in Fig.4.13(d) for period B.

The online jet E_T is observed to underestimate the offline jet E_T by 10% at most. Central collision events have the largest JES for all the η regions considered with mean values of 9(8)% in period A(B). For peripheral events the mean difference in energy between the offline and online jets reaches the lowest values for the central part of the detector. In this region of the η-phase space the energy measurements are better understood. In the $0.8 < |\eta| < 2.8$ region, there are cracks containing the cables to support the Inner Detector and the Central Magnet System. Here the energy loss is estimated by extrapolating the energy from the neighbouring calorimeter cells.

The JER ranges between the mean values of 10% and 6% in period A and from 6% to 8% in period B, for E_T less than 80 GeV. The relative energy resolution is larger for peripheral than for central events, while for the JES variable it is the opposite.

The transverse energy mean offset for the `EF_fj15_a4hi_EFFS_L1FJ0` trigger chain as a function of the offline jet E_T is presented in Fig. 4.14(a), and is separated in centrality class and particle going side. The JER is shown in Fig. 4.14(b). The relative jet energy scale shows no dependence on centrality for the proton going

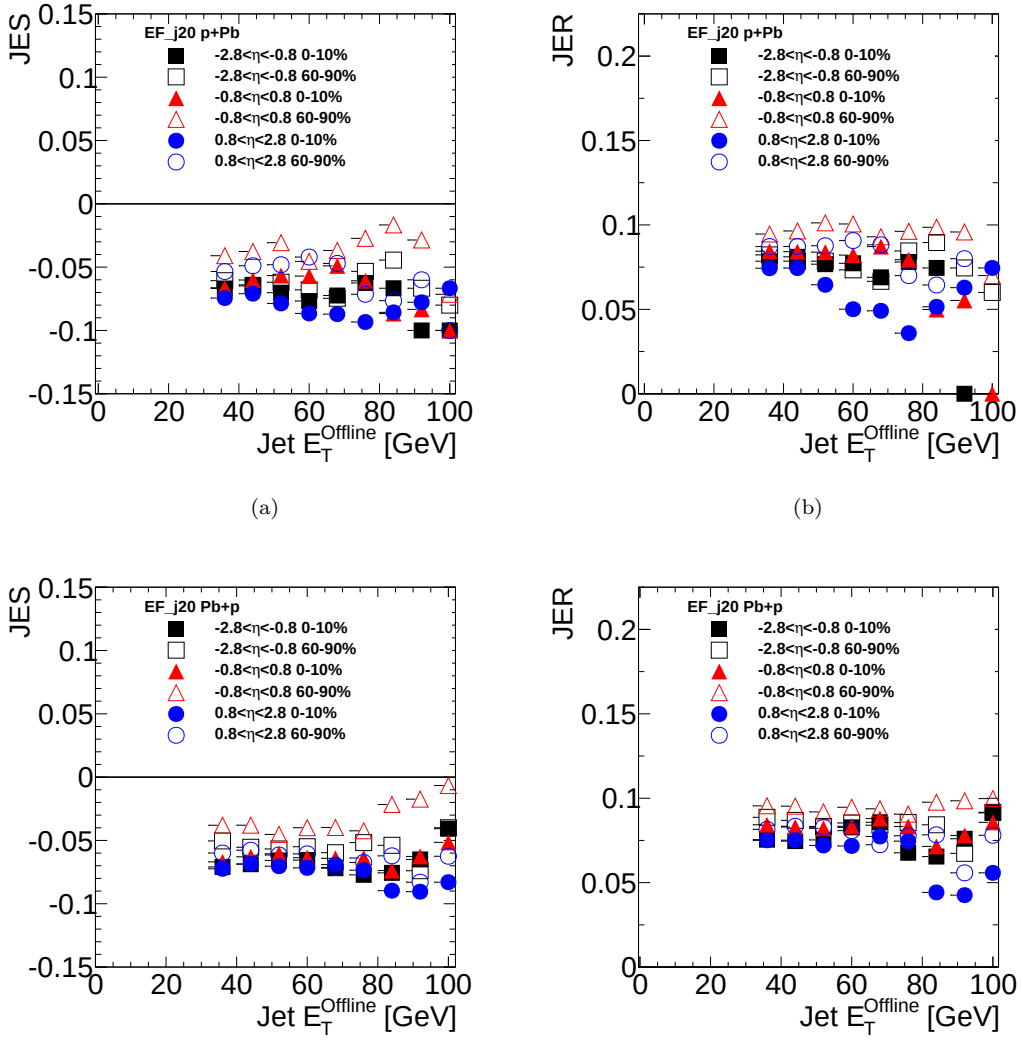

FIGURE 4.13: The relative JES (JER) for the `EF_j20_a4hi_EFFS_L2mbMBTS` trigger chain as a function of the offline jet E_T are presented in Fig. 4.13(a) (4.13(b)) and 4.13(c) (4.13(d)) for periods A (p+Pb) and B(Pb+p). The 0-10% (60-90%) centrality class is represented by the open (closed) markers, and the different η regions of the calorimeter are represented by the different style markers.

side. The online jet E_T is underestimated by 8% at most. In the lead going side there is a difference between the different centrality classes. The JES in peripheral centrality class rises with increasing E_T. Regarding the relative JER, in the proton going side there is no visible dependence on centrality and the resolution is bounded by 10%, while for the lead going side the resolution worsens with increasing centrality and transverse energy.

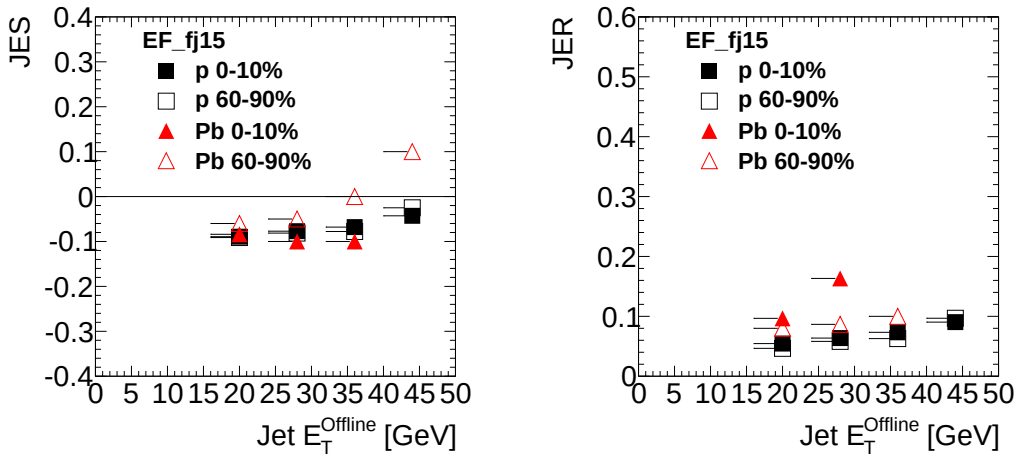

(a) (b)

FIGURE 4.14: The relative JES (JER) for the `EF_fj15_a4hi_EFFS_L1FJ0` trigger chain as a function of the offline jet E_T are presented in Fig. 4.14(a) and 4.14(a). The 0-10% (60-90%) centrality class is represented by the open (closed) markers, the different particle going side is represented by the different style markers.

4.5.2.2 $\Delta\phi$ mean offset and resolution

The $\Delta\phi$ mean offset and resolution between the matched online and offline jets are presented in Fig. 4.15(a) as a function of the offline jet E_T for central and peripheral collision events. The mean offset of $\Delta\phi$ for the `EF_j20_a4hi_EFFS_L2mbMBTS` trigger chain shows that the online and offline jets are very close in ϕ, smaller than 0.002 radians with an estimated resolution of 2%. This result is independent on the centrality class of the collision.

The $\Delta\phi$ mean offset and resolution of the `EF_fj15_a4hi_EFFS_L1FJ0` trigger chain is presented in Fig. 4.15(b). The resolution exhibited by this trigger chain is pretty similar to the one depicted by the `EF_j20_a4hi_EFFS_L2mbMBTS` trigger chain. The mean offset suggest a dependence on E_T ranging from $\Delta\phi \approx 0.0$ to $\Delta\phi \approx -0.01$ radians.

4.5.2.3 $\Delta\eta$ mean offset and resolution

Fig. 4.16(a) shows the $\Delta\eta$ mean offset and resolution as a function of the offline jet E_T for peripheral collision events and central collision events. The $\Delta\eta$ resolution result displayed is similar to the one observed for the $\Delta\phi$. When considering

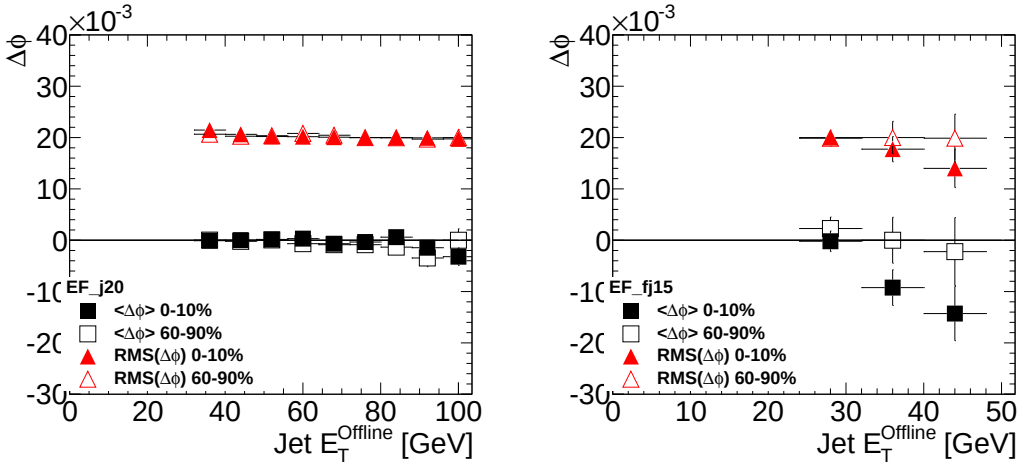

(a) (b)

FIGURE 4.15: $\Delta\phi$ mean offset (squared markers) and resolution (triangular markers) as a function of the offline jet E_T for the `EF_j20_a4hi_EFFS_L2mbMBTS` (`EF_j20`) and `EF_fj15_a4hi_EFFS_L1FJ0` (`EF_fj15`) trigger chains are shown in Figs. 4.15(a) and 4.15(b). Closed (open) markers represent the results of central (peripheral) collisions.

the $\Delta\eta$ mean offset one observes no dependence on the E_T. Also, no significant E_T dependence is observed in the `EF_fj15_a4hi_EFFS_L1FJ0` trigger in Fig. 4.16(b).

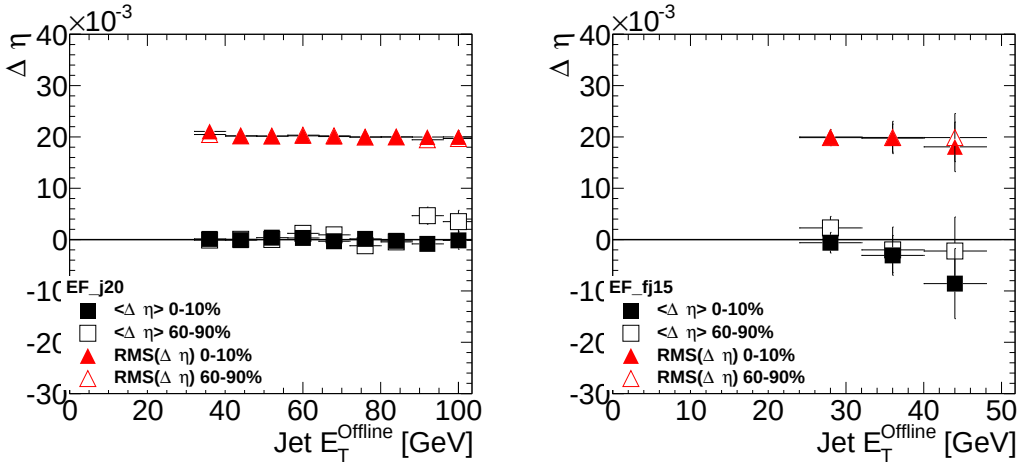

(a) (b)

FIGURE 4.16: $\Delta\eta$ mean offset (squared markers) and resolution (triangular markers) as a function of the offline jet E_T for the `EF_j20_a4hi_EFFS_L2mbMBTS` (`EF_j20`) and `EF_fj15_a4hi_EFFS_L1FJ0` (`EF_fj15`) trigger chains shown in Figs. 4.16(a) and 4.16(b). Closed (open) markers represent the results of central (peripheral) collisions.

4.5.3 Event Filter jet efficiency and purity

4.5.3.1 Single-inclusive jet triggers

In this section are assessed some of the EF inclusive single jet trigger chains defined in the jet trigger menu presented in Sec. 3.1. The EF_j75_a4hi_EFFS_L1J15 was the lowest unprescaled trigger. All events that have at least one jet with a E_T over 80 or 90 GeV were also selected by the EF_j75_a4hi_EFFS_L1J15 trigger chain.

The jet trigger efficiency and purity of each trigger is studied with respect to L1 triggers, requiring thus the event trigger decision. By estimating the EF efficiency and purity variables with respect to L1 in regions where the L1 jet trigger is already fully efficient, one is able study the EF trigger jet performance. The jet trigger efficiency is defined as:

$$\epsilon_{\text{trig}} = \frac{\#\text{ jets passing(offline selection } \wedge \texttt{ trigger L1\_X } \wedge \texttt{ jet } \texttt{E}_\texttt{T}^{\texttt{trig}} > \texttt{Y})}{\#\text{ jets passing (}\texttt{trigger L1\_X } \wedge \text{ offline selection)}} \quad (4.12)$$

where '`trigger L1_X`' stands for the L1 event trigger decision and represents the `L2mbMBTS`, `L1J10`, `L1J15` or `L1FJ0` triggers. '`jet` $\texttt{E}_\texttt{T}^{\texttt{trig}} >$ `Y`' stands for the matching between the offline jet and an online jet above the Y trigger threshold. The trigger efficiencies as a function of the offline jet E_T are presented in Fig. 4.17(a) and 4.17(b) for periods A and B.

Each trigger at its nominal value has an efficiency over 0.5 and all these jet trigger efficiencies reach the plateau close the threshold, demonstrating the good resolution of the EF jet trigger relatively to the offline jet. This is expected as the two reconstruction algorithms are similar. Central collision events are less efficient when compared to peripheral collision events. The underlying event deteriorates the trigger turn-on.

The jet trigger purities for the same jet trigger chains assessed in the efficiency performance are shown in Tab. 4.4. *Conf.* stands for the LHC fill configuration which can be p+Pb (period A) or Pb+p (period B). These results show that the EF jet trigger are over 95% pure. A small E_T threshold dependence in peripheral collisions is observed.

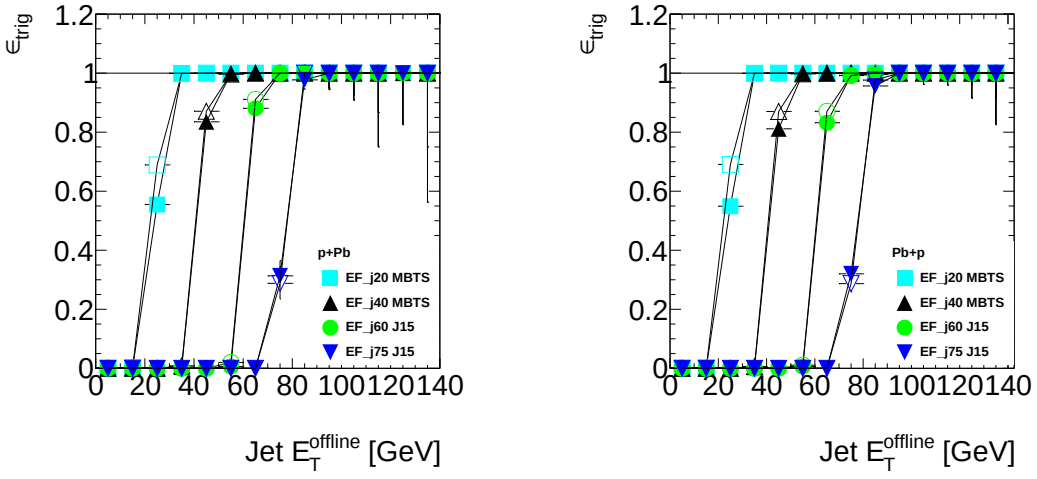

(a) (b)

FIGURE 4.17: Jet trigger efficiencies estimated as a function of the offline jet E_T. Fig. 4.17(a) shows period A (p+Pb) and Fig. 4.17(b) depicts period B (Pb+p). The `EF_j20_a4hi_EFFS_L2mbMBTS` (`EF_j20 MBTS`), the `EF_j40_a4hi_EFFS_L2mbMBTS` (`EF_j40 MBTS`), the `EF_j60_a4hi_EFFS_L1J15` (`EF_j60 J15`) and `EF_j75_a4hi_EFFS_L1J15` (`EF_j75 J15`) trigger chains are assessed. The 0-10% (60-90%) centrality class is depicted with closed (open) markers.

Trigger chain	Conf.	0-10% Purity [%]	60-90% Purity [%]
`EF_j20_a4hi_EFFS_L2mbMBTS`	p+Pb	$96.25^{+0.09}_{-0.1}$	$94.9^{+0.2}_{-0.2}$
	Pb+p	$96.26^{+0.05}_{-0.05}$	$94.74^{+0.08}_{-0.08}$
`EF_j30_a4hi_EFFS_L2mbMBTS`	p+Pb	$98.7^{+0.1}_{-0.1}$	$97.9^{+0.2}_{-0.2}$
	Pb+p	$98.55^{+0.07}_{-0.07}$	$98.2^{+0.1}_{-0.1}$
`EF_j40_a4hi_EFFS_L2mbMBTS`	p+Pb	$99.2^{+0.2}_{-0.2}$	$99.0^{+0.3}_{-0.3}$
	Pb+p	$99.21^{+0.09}_{-0.09}$	$98.8^{+0.1}_{-0.2}$
`EF_j50_a4hi_EFFS_L1J10`	p+Pb	$99.1^{+0.3}_{-0.4}$	$99.1^{+0.3}_{-0.5}$
	Pb+p	$99.2^{+0.1}_{-0.2}$	$99.1^{+0.2}_{-0.2}$
`EF_j60_a4hi_EFFS_L1J15`	p+Pb	$99.4^{+0.3}_{-0.5}$	$99.3^{+0.4}_{-0.7}$
	Pb+p	$99.1^{+0.2}_{-0.3}$	$99.1^{+0.3}_{-0.3}$
`EF_j75_a4hi_EFFS_L1J15`	p+Pb	$99.2^{+0.6}_{-1.0}$	$100^{+0.00}_{-1}$
	Pb+p	$98.7^{+0.4}_{-0.5}$	$98.9^{+0.5}_{-0.7}$

TABLE 4.4: Purity of EF jet triggers considering the different periods and distinct event topologies. The most 0-10% central and the 60-90% peripheral collisions are shown.

4.5.3.2 Forward jets: p going side versus Pb going side

The forward jet triggers take a special concern, as physics plays a different role in these domains as we already saw (see Fig. 1.5). The goal is to study the efficiency of the jet trigger in the forward region of the detector and compare with the performance reached in the central region.

Figs. 4.18(a) and 4.18(b) illustrate the `EF_fj15_a4hi_EFFS_L1FJ0` jet trigger efficiency as a function of the offline transverse energy for the two different periods and proton going side versus lead going side.

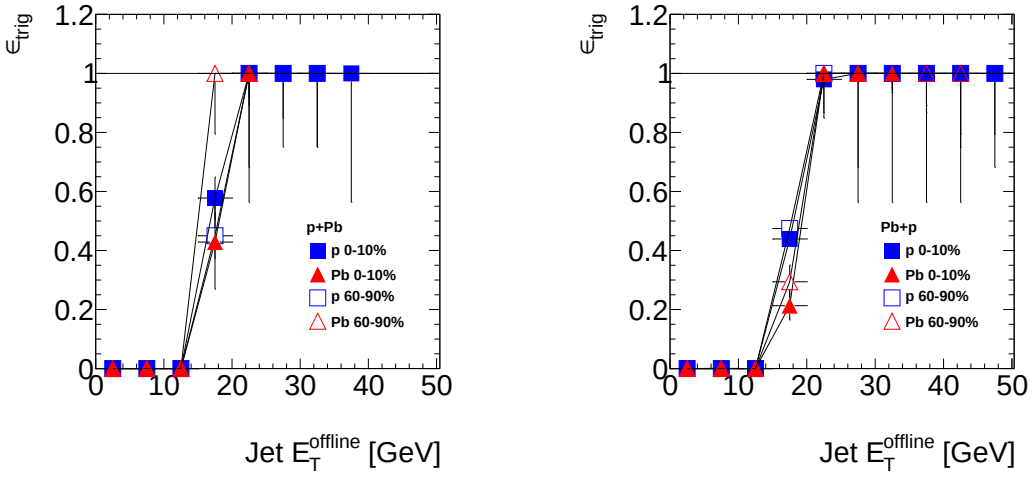

FIGURE 4.18: The jet trigger efficiency of `EF_fj15_a4hi_EFFS_L1FJ0` as a function of the jet E_T is shown. Fig. 4.18(a) shows period A (p+Pb) and Fig. 4.18(b) period B (Pb+p). $p(Pb)$ represents the proton(lead) going side and is displayed in squared (triangular) markers.

All jet trigger efficiencies reach full efficiency at approximately 20 GeV of transverse energy. The mid point of the turn on curves are at $E_T \approx 18$ GeV, except for period A in peripheral collisions and on the lead going side. In period B, the lead going side has a slower turn on curve when compared to the proton going side. In this period, when comparing results in different centralities, peripheral collisions have a slight larger efficiency when compared to the one in central collision events. In period A, one cannot observe the same behaviours as in period B.

The jet trigger purity for the `EF_fj15_a4hi_EFFS_L1FJ0` chain is not presented. The *bad* jet quality cut is only implemented for the $|\eta| < 2.8$ jets, thus making the sample of offline forward jets biased.

4.5.3.3 Jet isolation

In this section is assessed the performance of the jet trigger when one jet has another jet in its vicinity. A jet is considered close by if the distance between it and the closest one is less than DR=0.5, while an isolated jet has its closest neighbour jet beyond DR=1.0 in the $\eta \times \phi$ plane. A close by jet may lead to an overlap of cells with the jet of interest resulting in a higher jet energy which in turn leads to a bias in the efficiency.

Fig. 4.19(a) and Fig. 4.19(b) represent the jet trigger efficiency of the several triggers as a function of the jet E_T for the 0-10% and 60-90% centrality classes.

A slight systematic difference between the turn on curves for the isolated jet when compared to the close jet is observed. This difference decreases with increasing transverse energy.

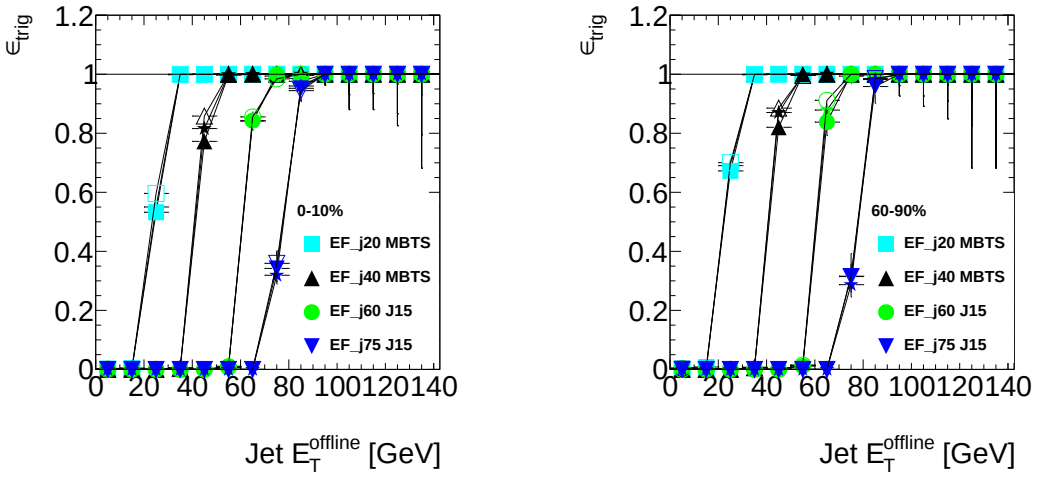

(a) (b)

FIGURE 4.19: The `EF_j20_a4hi_EFFS_L2mbMBTS`, `EF_j40_a4hi_EFFS_L2mbMBTS`, `EF_j60_a4hi_EFFS_L1J15` and `EF_j75_a4hi_EFFS_L1J15` trigger efficiency curves as a function of the offline jet E_T and their dependence on isolation are presented. Each marker style identifies a different trigger, open (closed) markers identify $DR > 1$ ($DR < 0.5$). The starred markers represent the jet trigger efficiency presented in Fig. 4.17. Fig. 4.19(a) shows the 0-10% centrality class while Fig. 4.19(b) presents the 60-90%.

4.5.4 Multi-jet triggers

In this section the per event efficiencies of the multi-jet trigger chains defined in Tab. 3.1 are analysed. A dijet event is triggered by the EF if two or more jets are reconstructed online with an energy of at least 20 GeV. The multi-jet trigger efficiency of the `EF_2j20_a4hi_EFFS_L2mbMBTS` trigger chain is defined as:

$$\epsilon_{\text{trig}} = \frac{\#\text{ events passing(offline selection } \wedge \texttt{ jet}\,\texttt{E}_\texttt{T}^{\texttt{trig,1}} > 20 \wedge \texttt{jet}\,\texttt{E}_\texttt{T}^{\texttt{trig,2}} > 20)}{\#\text{ events passing (offline selection)}} \tag{4.13}$$

It is required that at least two separate offline jets match a different online jet. As this is a per event variable one can represent this efficiency as a function of the two highest E_T jets, which are the ones that most likely triggered the event. Fig. 4.20(a) and 4.20(b) show the bi-dimensional efficiency as a function of the offline leading jet of the event in the x-axis and as a function of the offline sub-leading jet in the y-axis, for the 0-10% and 60-90% centrality classes. The jet trigger efficiency is represented in the z-axis. While there is a dependence on both jet E_T, the turn-on curve of the sub-leading (SL) offline jet starts earlier as this energy is at most as larger as the leading (L) offline jet one.

Fig. 4.20(c) and 4.20(d) depict the dijet trigger efficiency (DJT) as a function of the sub-leading offline jet for the 0-10% and the 60-90% centrality classes. Also shown is the single jet trigger efficiency (SJT) as a function of the sub-leading offline jet E_T. The single jet trigger efficiency is slightly larger (less than 1%) when compared to the dijet trigger. The difference is caused by the multiplicity requirement of the dijet trigger.

The next trigger chain which will be discussed is the `EF_2j10_a4hi_EFFS_L1TE90`. A reminder that this trigger selects events with at least two online jets with an E_T above 10 GeV and a collected electromagnetic energy in both sides of the FCal higher than 90 GeV. The efficiency for this trigger chain is defined as:

$$\epsilon_{\text{trig}} = \frac{\#\text{ events(offline selection} \wedge \texttt{jet}\,\texttt{E}_\texttt{T}^{\texttt{trig,1}} > 10 \wedge \texttt{jet}\,\texttt{E}_\texttt{T}^{\texttt{trig,2}} > 10 \wedge \text{L1TE90})}{\#\text{ events (offline selection)}} \tag{4.14}$$

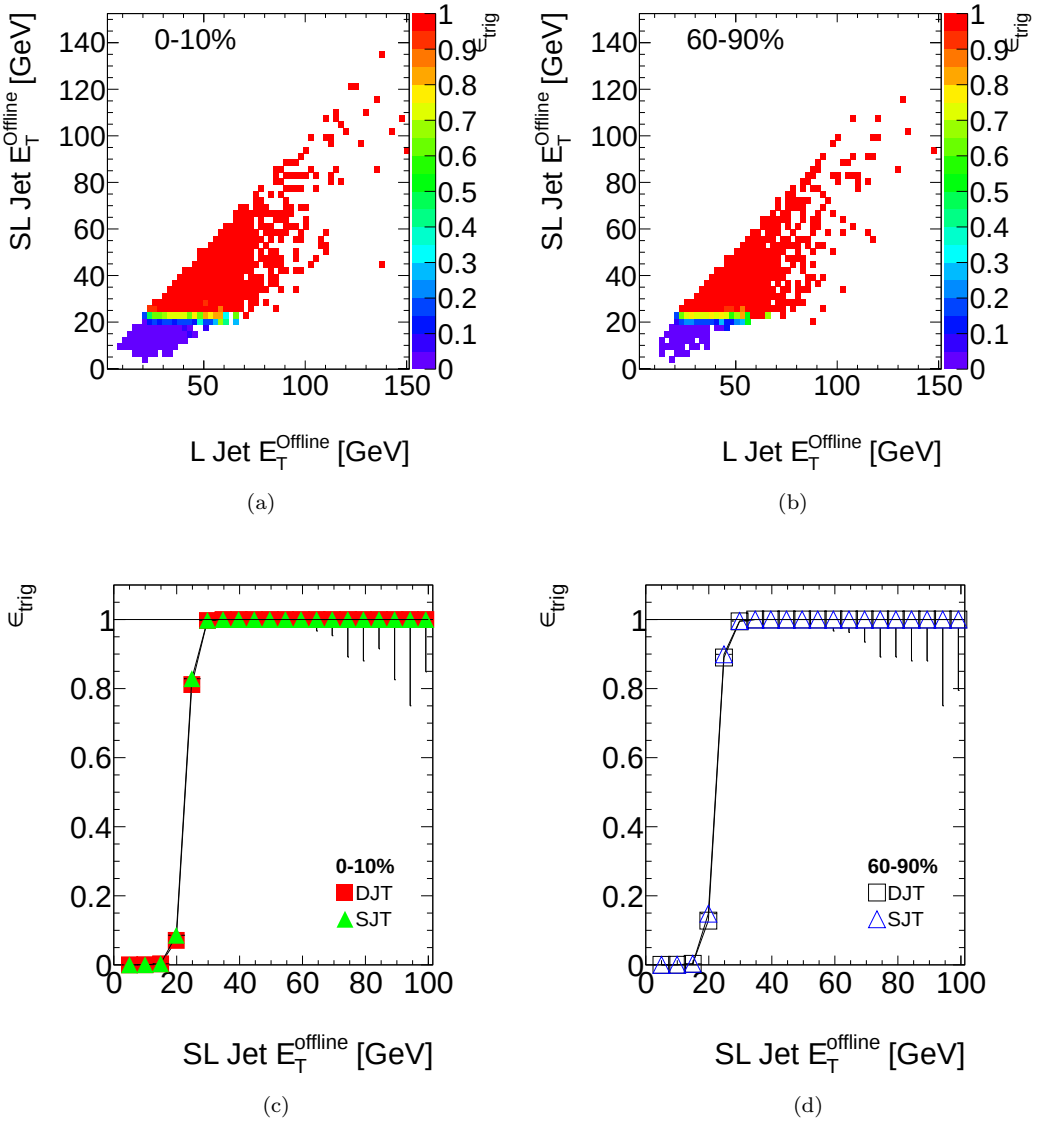

(a) (b)

(c) (d)

FIGURE 4.20: The dijet trigger efficiency for the `EF_2j20_a4hi_EFFS_L2mbMBTS` trigger chain is assessed. Fig. 4.20(a) and Fig. 4.20(b) show the dijet trigger efficiency for the 0-10% and 60-90% centrality classes as a function of the leading (L) and sub-leading (SL) offline jets. The efficiency parameter is represented in the z-axis. Fig. 4.20(c) and Fig. 4.20(d) present the same efficiency as a function of the sub-leading jet for the 0-10% and 60-90% centrality classes. The single jet trigger efficiency is also shown.

This efficiency is presented in Fig. 4.21 as a function of the ΣE_T^{FCal} (x-axis) and as a function of the sub-leading jet (y-axis). The jet trigger efficiency is represented in the z-axis. The ΣE_T^{FCal} is highly correlated to the $\Sigma E_T^{Fcal,Pb}$, which is used to define the centrality class of the collision, hence results in different centrality classes for this trigger chain are not presented. The ΣE_T^{FCal} and the E_T of a jet are shown to be orthogonal variables as presented in Fig. 4.21. Only when the two independent efficiencies pass the required energy thresholds is that when the efficiency reach the plateau, and those transition regions can be clearly seen at $E_T \approx 20$ GeV and $\Sigma E_T^{FCal} \approx 150$ GeV.

Fig.4.21(b) shows the trigger efficiency as a function of the ΣE_T^{FCal} when the sub leading jet has an E_T above 20 GeV. This allows the study of the ΣE_T^{FCal} dependence on the trigger efficiency of `EF_2j10_a4hi_EFFS_L1TE90` without biasing it due to the inefficiency on the jet E_T. The saturation is achieved at ΣE_T^{FCal} 150 GeV. On the other hand, Fig. 4.21(c) shows the same trigger efficiency as a function of the offline SL jet E_T, for events with ΣE_T^{FCal} greater than 150 GeV, the phase space where the `L1TE90` efficiency as a function of ΣE_T^{FCal} is "1". This trigger efficiency shows a turn on that starts at 5 GeV and saturates at 20 GeV.

The next two trigger chains, `EF_2j10_a4hi_deta40_L2mbMBTS` and the `EF_2j10_a4hi_deta40_eta50_L2mbMBTS`, require a pseudorapidity separation of 4.0 units between at least one pair of online jets, each with a E_T above 10 GeV. The second trigger considers the whole η-phase space (*_eta50_*), while the first considers the $|\eta^{offline}| < 3.2$ phase space. Fig. 4.22(a) and 4.22(b) show the dijet trigger efficiency for the `EF_2j10_a4hi_deta40_L2mbMBTS` trigger chain in the 0-10% and 60-90% centrality class, as a function of the 2^{nd} jet E_T and as a function of the $\Delta\eta^{offline} = |\eta_1^{offline} - \eta_2^{offline}|$. The subleading jet of the pair of offline jets that have a unique match to a pair of online jets of at least 10 GeV, with the greatest pseudorapidity separation in the event is chosen to study the dependence of the dijet trigger efficiency on the offline jet E_T. These pairs of offline jets are ordered in E_T. The good η resolution between online and offline jets allows a distinction between pairs of jets that don't have a 4.0 pseudorapidity difference, from those who have. The 2^{nd} jet E_T dependence is observed to be similar as in the `EF_2j10_a4hi_EFFS_L1TE90` trigger chain. The correlation between the 2^{nd} jet E_T and the $\Delta\eta^{offline}|$ is very small. Their relation is based on the η-position resolution between online and offline jets and a small dependence on E_T at low values is observed.

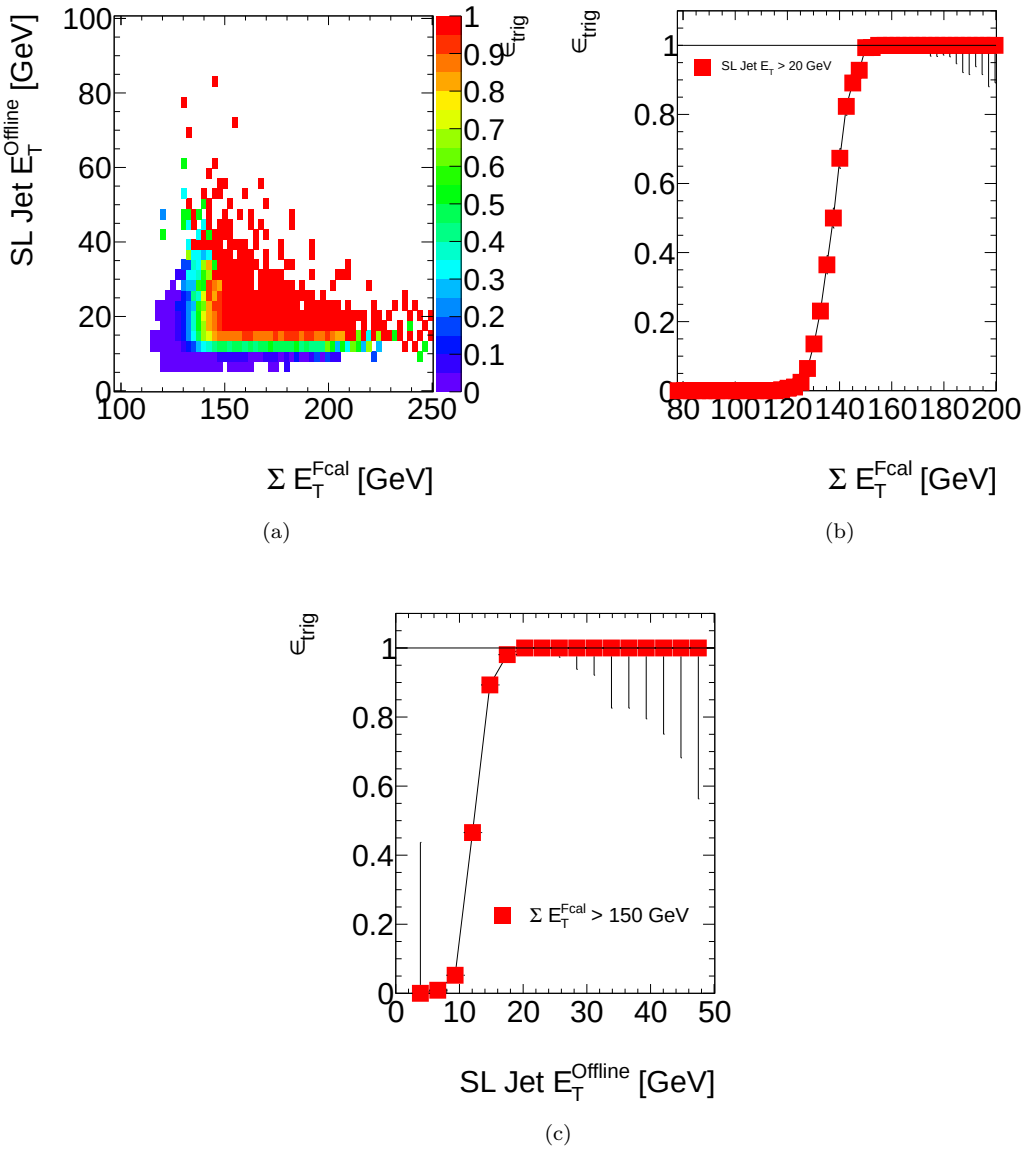

FIGURE 4.21: The bi-dimensional dijet trigger efficiency for the `EF_2j10_a4hi_EFFS_L1TE90` trigger chain as a function of the subleading jet (y-axis) and as a function of the $\Sigma\, E_T^{FCal}$ (x-axis) is shown in Fig. 4.21(a). The efficiency is represented in the z-axis. Fig. 4.21(b) and 4.21(c) shows the same trigger efficiency projected in the x and y axis.

The efficiency of the `EF_2j10_a4hi_deta40_eta50_L2mbMBTS` trigger chain is shown in Fig. 4.23(a) and 4.23(b) as a function of the 2^{nd} jet (y-axis) and as a function of the $\Delta\eta^{offline}$ (x-axis) for the 0-10% and 60-90% centrality classes. The same features discussed in Fig. 4.22(a) and 4.22(b) are observed.

To study the dependence of $|\Delta\eta|$ in the efficiency curve of this trigger chain, it is required that the 2^{nd} jet has an E_T of at least 20 GeV, to avoid biasing the efficiency curve. Fig. 4.24 show the trigger efficiencies as a function of $|\Delta\eta^{offline}|$

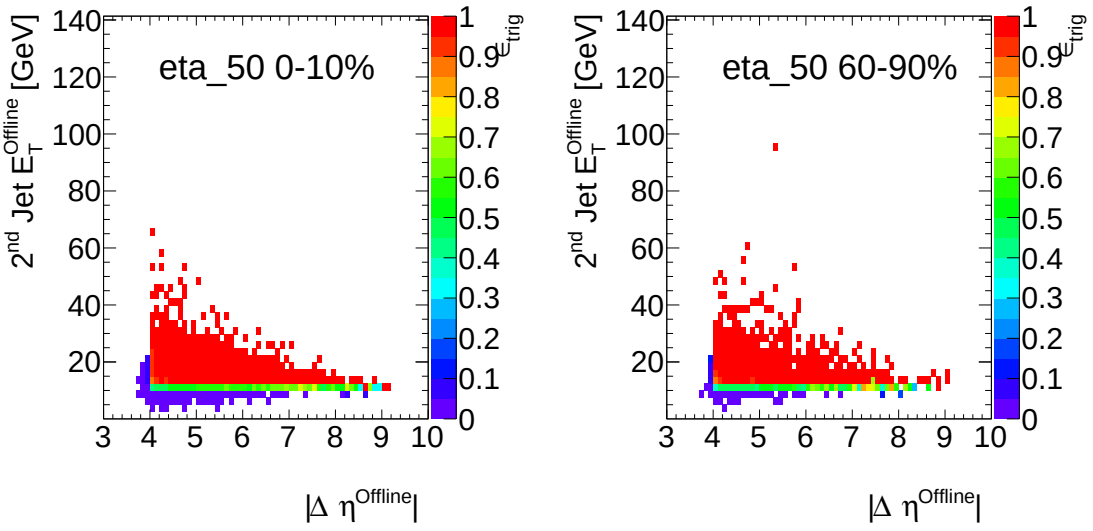

(a) (b)

FIGURE 4.22: Dijet trigger efficiency of `EF_2j10_a4hi_deta40_L2mbMBTS` trigger chain as a function of the 2^{nd} offline jet E_T and $|\Delta\eta^{offline}|$, for the 0-10% (Fig.4.22(a)) and 60-90% (Fig.4.22(b)) collision events. The trigger efficiency is shown in the z-axis.

of the both triggers that require the pseudorapidity separation between two online jets of 4.0 units. The trigger turn on is sharp, the saturation point of the efficiency curve is reached at 4.1 units.

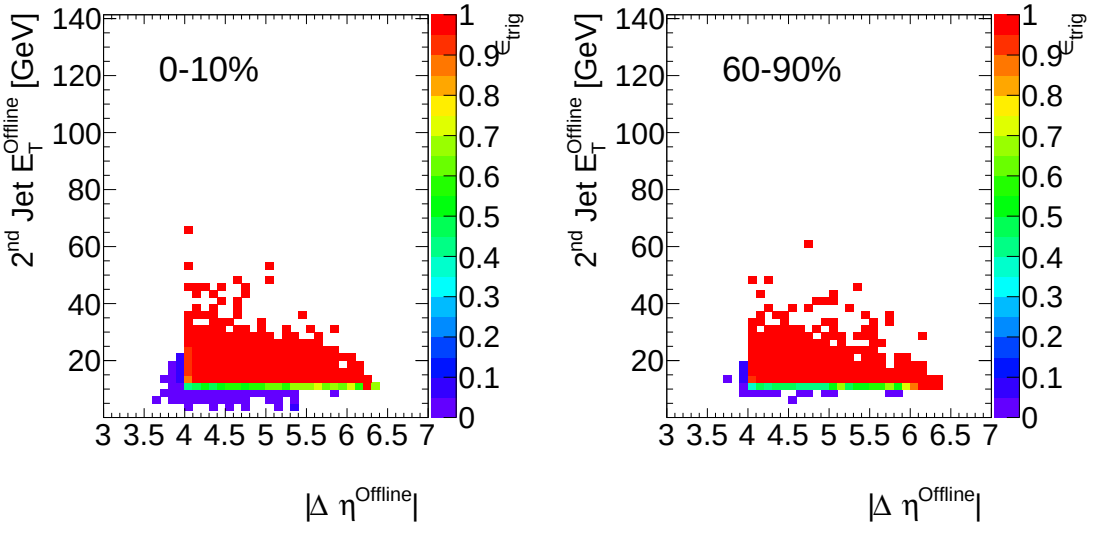

(a) (b)

FIGURE 4.23: Efficiency of `EF_2j10_a4hi_deta40_eta50_L2mbMBTS` dijet trigger chain as a function of $|\Delta\eta^{offline}|$ (x-axis) and 2^6nd jet E_T. The 0-10% centrality class is shown in Fig. 4.23(a) and in Fig. 4.23(b) the 60-90% centrality class. The trigger efficiency is represented in the z-axis.

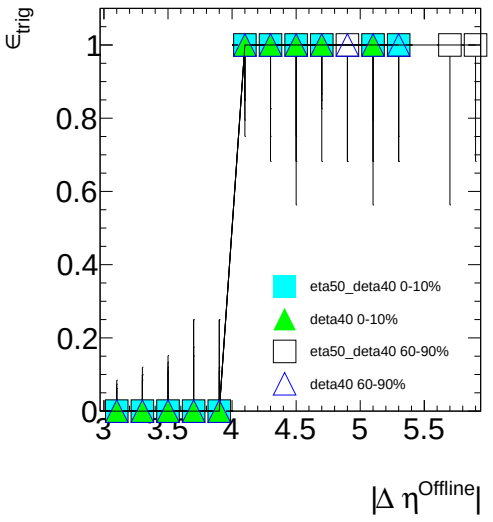

FIGURE 4.24: Efficiency of `EF_2j10_a4hi_deta40_eta50_L2mbMBTS` and `EF_2j10_a4hi_deta40_L2mbMBTS` dijet trigger chains as a function of $|\Delta\eta^{offline}|$. The 0-10% (60-90%) centrality class is represented with closed (open) markers.

Conclusions

The jet trigger system is crucial to select events that have jets that would allow the comparison of the experimental data to the theoretical predictions. The goals of the jet trigger menu included a flexible jet transverse energy spectra and events with certain jet specifications in order to pursue those predictions[6, 22]. The jet trigger system must have a high energy and position resolution and it is essential that it is unbiased in selecting different p+Pb physics events (e.g. in spite of event centrality class or jet pseudorapidity).

The ATLAS jet trigger system performance in a p+Pb environment has shown to be robust and efficient in selecting the required objects, despite the centrality class of the collision. The L1 and EF jet trigger stages were assessed with several metrics that included the efficiency, purity, transverse energy and angular mean offset and resolution results. In L1 and EF trigger levels the jet trigger performance is E_T threshold, centrality and particle going side dependent.

The L1 jet triggers `L1J10` and `L1J15` reach fully efficiency at 50 and 60 GeV, respectively. By studying the efficiency of the L1 triggers in separate centrality classes, it was shown that the underlying event affects the turn on curve as it adds more energy to the jet. The more central the collision is, the faster the turn on curve is.

At the EF jet trigger level, it was shown that the jet algorithm with underlying event subtraction, when compared to another algorithm that doesn't consider it, is more efficient in selecting the same online jets. The position deviation and resolution is different when one considers the central and forward jets. For central jets, the agreement is achieved by less than 5×10^{-4} units for both $\langle \Delta\phi \rangle$ and $\langle \Delta\eta \rangle$ with an associated resolution of 0.02 units for the same quantities. Relative jet energy scale and resolution are dependent on centrality and pseudorapidity. JES studies show that the online jet is systematically underestimated with respect to

the offline jet. This underestimation is slightly smaller in peripheral collisions. The relative energy resolution is observed to be at most 10%.

The centrality dependence of the jet trigger efficiency was shown to decrease with high energy threshold triggers. But, even at low E_T thresholds, the centrality class dependence of the efficiency turn on curve is small. For a trigger requiring an online jet of at least 20 GeV, the saturation point was observed to be at 27 GeV, while when requiring a transverse energy of at least 75 GeV in the online jet, the saturation point was at 82 GeV.

Isolated offline jets are slighly more efficient than jets that have a neighbour jet within a radius of 0.5.

When compared to single jet trigger efficiency, the dijet trigger efficiency as a function of the subleading jet E_T is only slightly affected by the different jet multiplicity requirement. A dijet trigger which also required a summed transverse energy measured in both sides of the Forward Calorimeter ($\sum E_T^{FCal}$) above 90 GeV and two jets with an online energy above 10 GeV was studied. The saturation region of the efficiency was observed to be $\sum E_T^{FCal} > 150$ GeV and the lowest jet $E_T > 20$ GeV. Another dijet trigger required not only two online jets of at least 10 GeV of transverse energy but also an online separation on pseudorapidity of 4.0 units. This trigger was shown to be fully efficient for pairs of jets with a pseudorapidity separation above 4.0 units and 20 GeV of transverse energy.

The ATLAS jet trigger system performance in a p+Pb environment has shown to be robust and highly efficient.

Appendices

Appendix A

Standard variables used in ATLAS detector

ATLAS employed a right-handed Cartesian coordinate system with the beam direction defining the z-axis. The x-y plane is called the transverse plane and y-z the longitudinal plane. While the x-axis points to the center of the LHC ring, the y-axis points towards the sky. The two beam lines cross at the $z = 0$ point which bisects the detector into side A ($z > 0$) and C ($z < 0$).

Useful quantities are the polar (θ) and azimuthal angles (ϕ), the pseudorapidity (η), the transverse momentum (p_T) and transverse energy (E_T):

- The polar angle (θ) is measured with respect to the x-axis and its zero is defined on the positive direction of the z-axis.
- The azimuthal angle (ϕ) is the angle in the plane perpendicular to the beam line and $\phi = 0$ is on the positive x-axis.
- The rapidity can be perceived as the angle in an hyperbolic rotation of the space-time coordination, and is defined as:

$$y = \tanh^{-1} \frac{p_z}{E} = \frac{1}{2} \ln(\frac{E + p_z}{E - p_z}) \tag{A.1}$$

  If the particle mass can be neglected when compared to the energy of the particle, the rapididity can be derived simply as function of the polar angle,

Eq. A.2. This relation is commonly called pseudo-rapidity (η), and is a Lorentz boost invariant along the z-axis. In Table A.1 some representative values of η are presented according to the corresponding polar angle.

- Pseudo-rapidity (η)

$$\eta = -\ln\tan\left(\frac{\theta}{2}\right) \tag{A.2}$$

θ (degrees)	η
0	$+\infty$
0.85	4.9
4.67	3.2
7.69	2.7
9.39	2.5
45	0.88
90	0

TABLE A.1: Representative values of pseudorapidity (η) for some polar angles (θ). $|\eta| = 4.9$, $|\eta| = 3.2$, $|\eta| = 2.7$ and $|\eta| = 2.5$ are the outter limit values of the hadronic calorimeter, the hadronic calorimeter end-cap, the muon spectrometer and the inner detector, respectively.

- The pseudorapidity and the azimuthal angle define a new coordinate space, the η-ϕ plane. The relative distance between two points (η_1, ϕ_1) and (η_2, ϕ_2) in this plane is commonly defined as:

$$\Delta R = \sqrt{(\Delta\phi)^2 + (\Delta\eta)^2} \tag{A.3}$$

$$\Delta\phi = \phi_2 - \phi_1 \tag{A.4}$$

$$\Delta\eta = \eta_2 - \eta_1 \tag{A.5}$$

- Transverse measurements such as transverse momentum (p_T), transverse energy (E_T) consist on the projection of the respective quantity on the x-y plane, the transverse plane.

$$E_T = \frac{E}{\cosh(\eta)} \tag{A.6}$$

$$p_T = |\mathbf{p}|\sin(\theta) \tag{A.7}$$

Appendix B

Jet reconstruction algorithms

A jet reconstruction algorithm is a software procedure that will assembles sets of energy cells in order to reconstruct the energy of the particle that originated those signals. The jet reconstruction algorithm used in this dissertation is the anti-k$_T$ [23]. This algorithm considers a list of preclusters formed from calorimeter towers arranged in decreasing order of relative transverse momentum (k$_T$). Each seed (precluster) as its four-momentum vector defined along with the quantities d_{ij} and d_{iB}, which are defined as:

$$d_{ij} = \min(k_{Ti}^{-2},\, k_{Tj}^{-2})\,\frac{(\Delta R_{ij}^2)}{R^2} \tag{B.1}$$

$$\Delta R_{ij}^2 \;=\; (\eta_i \,-\, \eta_j)^2 \,+\, (\phi_i \,-\, \phi_j)^2 \tag{B.2}$$

$$d_{iB} \;=\; k_{Ti}^{-2} \tag{B.3}$$

where the η_i and ϕ_i is the position of the i precluster in the (η,ϕ) space and R is a parameter of the algorithm. The jet algorithm considers the seed with the highest k$_T$, i, and proceeds recursively as follows:

1) Find the minimum d value in the list.

2.a) If the minimum d value is d_{ij}, merge preclusters j to i considering the four-momentum sum of the two items.

2.b) If the minimum d value is d_{iB}, no more preclusters will be added to precluster i. Remove precluster i from the list of preclusters and add it to the jet list.

3) Define new d_{ij} and d_{iB} quantities and go to step 1.

This process will continue until no more preclusters exist in the list. The R parameter represents the jet radius in the (η,ϕ) space. The most commonly used value is R = 0.4 representing a maximum jet radius of 0.4, which contain a typical jet produced with the LHC beam energies.

In a proton-proton environment, the preclusters used are topological cell clusters which can be interpreted as an attempt to assemble the three-dimensional cells that contain the particles signals. The clustering procedure is based on the signal significance compared to the electronic noise of the neighboring cells. A more detailed description of the algorithm used can be found in [18, 24].

In a lead-lead environment, due to the large underlying event processes additional steps are considered during the jet reconstruction procedure. These additional steps aim to subtract the underlying event contribution from the jet based on the premise that the energy measured in the cell is the energy sum from the underlying event and the jet energy. The energy contribution of the underlying event is η dependent. This algorithm considers the seeds as towers of cells grouped in $\eta \times \phi = 0.1 \times 0.1$ calibrated at the electromagnetic scale. To reconstruct jets in a heavy ion environment [14, 25] the following steps are followed:

1. Identification of 'pseudo-jets' using the anti-k$_T$ jet reconstruction algorithm with R = 0.2. The seeds are considered to be 'pseudo-jets' if:

$$D = \frac{\max(E_T^{EM})}{\langle E_T^{EM} \rangle} > 4 \tag{B.4}$$

2. The energy density is computed for each $\eta = 0.1$ strip and in each calorimeter layer. This energy density is estimated by:

$$\rho_{layer}(\eta) = \frac{1}{N} \sum_{i \epsilon M, j \epsilon N} \frac{E_{Tij}}{\Delta\eta\Delta\phi} \tag{B.5}$$

Not considering the tower cells belonging to 'pseudo-jets'. The underlying event contribution is then subtracted in each cell by:

$$E_T^{subtracted} = E_T^{total} - \rho_{layer}(\eta)\Delta\phi\Delta\eta \tag{B.6}$$

3. Steps # 1. and # 2. are performed again after subtracting the underlying event energy contribution from the jet energy. The condition to become a 'pseudo-jet' in step #1 is changed to $E_T^{EM} > 4$ GeV.

4. The 'pseudo-jets' from step #3 are used as seeds in the anti-k$_T$ jet reconstruction algorithm with R = 0.4, which finally defines the jet.

   There are other corrections to perform to these newly defined jets. In a subsequent step, a correction which considers misalignments between the seeds in step #4 and #3 and accounts for over-subtracted energies in jets below 15 GeV which produce minor effects. Finalizing with the hadronic calibration, which consists in a multiplicative correction for the detector response derived from Monte Carlo simulations[25].

Appendix C

Tracks and jet selection cuts

Track quality and Minimum Bias cuts

The Minimum Bias tracking cuts that were applied as offline event selection are the following:

- Track requirement that corresponds to inside-out tracking algorithms only;
- $|\eta^{trk}| < 2.5$;
- $p_T^{trk} > 100$ MeV;
- at least one pixel hit;
- one B-layer hit if one is expected;
- SCT hit requirements defined in C.1;
- transverse and longitudinal impact parameters $|d_0| < 1.5$ mm and $|z_0 \sin(\theta)| < 1.5$ mm evaluated with respect to the reconstructed primary vertex or with respect to the beam line otherwise;
- $\sigma_{d_0}/d_0| < 3$;
- $|\sigma_{z_0 \sin(\theta)}/z_0 \sin(\theta)| < 3$;

Loose track definition

A "loose" track quality requirement is defined for offline reconstructed tracks as:

- track pseudo-rapidity $|\eta_{trk}| < 2.5$;
- at least one pixel hit;
- one B-layer hit if one is expected;
- $Prob(\chi^2,\text{Ndof}) > 0.01$ for $p_T^{trk} > 10\ GeV/c$;
- transverse and longitudinal impact parameters $|d_0| < 1.5$ mm and $|z_0 \sin(\theta)| < 1.5$ mm evaluated with respect to the reconstructed primary vertex or with respect to the beam line otherwise;
- SCT hit requirement defined in table C.1;

$p_T^{trk}\,[MeV/c]$	# of minimum SCT hits
$100 < p_T < 200$	2
$200 < p_T < 300$	4
$300 < p_T$	6

TABLE C.1: SCT hit requirement for loose track definition.

The impact parameter variable in the Inner Detector context is the closest distance between the reconstructed track considering the reverse trajectory from the ID into the beam line or the reconstructed primary vertex.

Bad and ugly jets

To remove *ugly* jets one has to require that the reconstructed jets have the following properties:

- The energy fraction in the transition region between barrel and end-cap is below 0.5;
- The energy fraction in dead cells is less than 0.5;

- The fraction of the jet energy coming from the correction of a being a dead cell is below 0.5.

Bad jets are associated with errors in the calorimeter and jets that were formed in a non hard scatter process. To remove *bad* jets associated with hadronic end-caps (HEC) spikes, one of the following set of conditions must be fulfilled.

- HECf, is the energy fraction of the jet in the HEC, must be below 0.5;
- The cell Q-factor measures the difference between the measured signal shape and the expected signal shape that is used to reconstruct the cell energy. This variable is computed has $\Sigma(a_i^{expected} - a_i^{measured})^2$, where $a_i^{measured}$ ($a_i^{expected}$) represents the measured (expected) pulse shape. HECQ is the fraction of energy corresponding to HEC cells with a Q-factor greater than 4000, and if this fraction is above 0.5 the jet is considered bad;

Or,

- $HECf > 1 - HECQ$

Or,

- A measured jet energy below -60 GeV;

Bad jets can also be reconstructed with coherent EM noise. To reject this kind of incidents the following quality cuts are applied:

- The jet must be reconstructed at the EM scale within $|\eta| < 2.8$;
- The fraction of energy associated with Liquid Argon cells with a Q-factor greater than 4000 must be under 0.8;
- The energy fraction in the electromagnetic calorimeter must be under 0.9;

Non-collision background and cosmic events can also create bad jets. To identify and reject these jets one of the following set of conditions must be fulfilled:

- The energy squared cells mean time of the jet must be above 10 ns;

Or,

- The energy fraction in the electromagnetic calorimeter is below 0.05;
- The jet charged fraction, is defined as the ratio of the transverse momentum sum of tracks associated to the jets divided by the calibrated jet transverse momentum, is below 0.1;
- The jet at the EM scale is reconstructed within $|\eta| < 2$;

Or,

- The energy fraction in the electromagnetic calorimeter is above 0.95;
- The jet charged fraction, defined as the ratio of the transverse momentum sum of tracks associated to the jets divided by the calibrated jet transverse momentum, is below 0.05;
- The jet at the EM scale is reconstructed within $|\eta| < 2$;

Or,

- The energy fraction in the electromagnetic calorimeter is below 0.05;
- The jet at the EM scale is reconstructed within $|\eta| > 2$;

Or,

- The maximum energy fraction in one calorimeter layer is above 0.99;
- The jet at the EM scale is reconstructed within $|\eta| < 2$;

This quality selection of jets is also known as the *bad-medium* jet selection cut in ATLAS.

Appendix D

On the uncertainty of the expectation value

Considering two samples k and N, where k is a subset of N. k can be interpreted as the number of k successes in a sample N. The expectation value $\epsilon = k/N$ is clearly a value between $[0, 1]$ and is a good estimate to the *true* efficiency of the selecting criteria. To estimate correctly this *true* efficiency (ε) the binomial distribution is considered. This distribution have limitations which give unexpected results. These limitations are known. The binomial distribution gives unexpected results when we have only one sample and its result is $\epsilon \pm \delta\epsilon = 1 \pm 0$ or $\epsilon \pm \delta\epsilon = 0 \pm 0$. These are unexpected results because the expectation values are different from the true efficiency and both distributions can give results assuming a perfect certainty. In the dissertation's analysis, this limit is observed quite often in the efficiency and purity results, and so the Bayes theorem is mandatory to calculate more accurate uncertainties.

The Bayes Theorem is used to calculate $\mathrm{P}(\varepsilon \,|\, k\, N)$ given $\mathrm{P}(k \,|\, \varepsilon\, N)$. $\mathrm{P}(\varepsilon \,|\, k\, N)$ is the probability that the true efficiency is between ε and $\varepsilon + d\varepsilon$. $\mathrm{P}(k \,|\, \varepsilon\, N)$ is assumed to follow the binomial distribution. Thus, the Bayes theorem for the Binomial distribution is:

$$P(\varepsilon \,|\, k\, N) = \frac{P(k \,|\, \varepsilon\, N) P(\,\varepsilon \,|\, N\,)}{A} \tag{D.1}$$

where A is a normalization constant and $\mathrm{P}(\,\varepsilon\,|\,N\,)$ represent the possible values of the true efficiency before we analyse the data, which we consider to be any real number from 0 to 1 with equal probability. To determine the normalization constant we proceed as:

$$1 = \frac{1}{A}\int_{-\infty}^{+\infty} P(k\,|\,\varepsilon\,N)P(\,\varepsilon\,|\,N\,) \tag{D.2}$$

$$= \frac{1}{A}\frac{N!}{k!(N-k)!}\int_{0}^{1} \varepsilon^{k}(1-\varepsilon)^{N-k}d\varepsilon \tag{D.3}$$

The Beta distribution is defined as $\int_0^1 t^{\alpha-1}(1-t)^{\beta-1}dt$. The normalization constant is subject to N and k. In this case, $\alpha = k+1$ and $\beta = N-k+1$. The mode of the Beta distribution is defined as $\frac{\alpha-1}{\beta+\alpha-2}$, which in this case is simply k/N. The mode is the value which is presented in the dissertation as the true efficiency. Follows the calculation of the uncertainty interval around the mode. In the dissertation's analysis is used a confidence level of 68.3%, which is the equivalent of "1 σ" for the Gaussian distribution. We proceed to find the interval $[x, y]$ that:

$$\int_{x}^{y} P(\varepsilon\,|\,k\,N)d\varepsilon \;=\; 0.683 \tag{D.4}$$

In principle, there can be several values $[x, y]$ that can satisfy the above condition. The length of all possible intervals is minimized in order to find the shortest one. This procedure is achieved numerically using the Brent Method along with the cumulative distribution function of the Beta distribution. For more information on this procedure see Ref. [26] and references therein.

Bibliography

[1] Pavel Weber. ATLAS calorimetry: Trigger, simulation and jet calibration. 2008.

[2] F. Halzen and Alan D. Martin. QUARKS AND LEPTONS: AN INTRODUCTORY COURSE IN MODERN PARTICLE PHYSICS. 1984.

[3] A. van Hameren, P. Kotko, K. Kutak, C. Marquet, and S. Sapeta. Saturation effects in forward-forward dijet production in p+Pb collisions. 2014.

[4] H. Honkanen, M. Strikman, and V. Guzey. Modeling nuclear parton distribution functions. 2013.

[5] Catalin Ristea. High p(T) suppression at forward rapidities in D + Au and Au + Au at s(NN)**(1/2) = 200-GeV. 2005.

[6] C.A. Salgado, J. Alvarez-Muniz, F. Arleo, N. Armesto, M. Botje, et al. Proton-Nucleus Collisions at the LHC: Scientific Opportunities and Requirements. *J.Phys.*, G39:015010, 2012.

[7] Michael L. Miller, Klaus Reygers, Stephen J. Sanders, and Peter Steinberg. Glauber modeling in high energy nuclear collisions. *Ann.Rev.Nucl.Part.Sci.*, 57:205–243, 2007.

[8] D Perepelitsa, B Cole, and P Steinberg. Centrality Determination in the 2012 and 2013 p+Pb data in ATLAS. Technical Report ATL-COM-PHYS-2013-588, CERN, Geneva, May 2013.

[9] R J Glauber. Lectures in theoretical physics. *Interscience, New York*, 1:315, 1959.

[10] ATLAS Collaboration. Centrality determination in the 2010 pb+pb physics data. Technical Report ATL-COM-PHYS-2011-427, CERN, Geneva, Apr 2011.

[11] B Cole, A Angerami, D Perepelitsa, M Spousta, M Rybar, P Balek, T Kosek, H Santos, and A Lopes. Properties of dijet asymmetries measured with 2.76 TeV/nucleon Pb+Pb collisions in ATLAS at the LHC. Technical Report ATL-COM-PHYS-2012-1039, CERN, Geneva, Jul 2012.

[12] Georges Aad et al. Measurement of the jet radius and transverse momentum dependence of inclusive jet suppression in lead-lead collisions at $\sqrt{s_{NN}}$= 2.76 TeV with the ATLAS detector. *Phys.Lett.*, B719:220–241, 2013.

[13] D Perepelitsa. Measurement of the centrality-dependence of inclusive jet production in p+Pb data at $\sqrt{s_{\mathrm{NN}}}$ = 5.02 TeV with the ATLAS detector. Dec 2013.

[14] D Perepelitsa, A Angerami, B Cole, P Steinberg, T Kosek, M Rybar, M Spousta, and A Lopes. Measurement of the centrality-dependence of inclusive jet production in p+Pb data at $\sqrt{s_{NN}}$ = 5.02 TeV with the ATLAS detector. Technical Report ATL-COM-PHYS-2013-1369, CERN, Geneva, Sep 2013.

[15] J. Beringer et al. Review of Particle Physics (RPP). *Phys.Rev.*, D86:010001, 2012.

[16] Lyndon Evans and Philip Bryant. Lhc machine. *Journal of Instrumentation*, 3(08):S08001, 2008.

[17] G. Aad et al. The ATLAS Experiment at the CERN Large Hadron Collider. *JINST*, 3:S08003, 2008.

[18] G. Aad et al. Expected Performance of the ATLAS Experiment - Detector, Trigger and Physics. 2009.

[19] Georges Aad et al. Performance of the ATLAS Trigger System in 2010. *Eur.Phys.J.*, C72:1849, 2012.

[20] Leonid Frankfurt and Mark Strikman. Diffractive phenomena in high energy processes. 2013.

[21] ATLAS Collaboration. Performance of the atlas minimum bias and forward detector triggers in ppb collisions. Technical Report ATLAS-COM-CONF-2013-103, CERN, Geneva, Jul 2013. svn area: https://svnweb.cern.ch/cern/wsvn/atlasgroups/Trigger/TriggerNotes/MinBiasFD2013.

[22] Krzysztof Kutak and Sebastian Sapeta. Gluon saturation in dijet production in p-Pb collisions at Large Hadron Collider. *Phys.Rev.*, D86:094043, 2012.

[23] Matteo Cacciari, Gavin P. Salam, and Gregory Soyez. The Anti-k(t) jet clustering algorithm. *JHEP*, 0804:063, 2008.

[24] L Asquith, B Brelier, J M Butterworth, M Campanelli, T Carli, G Choudalakis, P A Delsart, S De Cecco, P O Deviveiros, M D'Onofrio, S Eckweiler, E Feng, P Francavilla, S Grinstein, I La Plante, J Huston, N Ghodbane, D Lopez Mateos, B Martin, N Makovec, S Majewsky, M Martinez, D W Miller, J Monk, K Perez, C Roda, J Robinson, A Schwartzmann, F Spano, K Terashi, F Vives, P Weber, and S Zenz. Performance of Jet Algorithms in the ATLAS Detector. Technical Report ATL-PHYS-INT-2010-129, CERN, Geneva, Dec 2010.

[25] B.Cole, A.Angerami, D.Perepelitsa, M.Spousta, M.Rybar, P.Balek, T.Kosek, H.Santos, A.Galan. Performance of jet reconstruction in heavy ion collisions. *ATL-COM-PHYS-2011-1733*, 2012.

[26] Rene Brun and Fons Rademakers. ROOT - An Object Oriented Data Analysis Framework. *Proceedings AIHENP'96 Workshop, Lausanne, Sep. 1996, Nucl. Inst. & Meth. in Phys. Res. A 389.* See http://root.cern.ch/ for more information.

Abbreviations

ALICE	**A** **L**arge **I**on **C**ollider **E**xperiment
ATLAS	**A** **T**oroidal **L**HC **A**pparatu**S**
CERN	European Organization for Nuclear Research
CMS	**C**ompact **M**uon **S**olenoid
COMPASS	**Co**mmon **M**uon and **P**roton **A**pparatus for **S**tructure and **S**pectroscopy
CTP	**C**entral **T**rigger **P**rocessor
DIS	**D**eep **I**nelastic **S**cattering
DQ	**D**ata **Q**uality
EF	**E**vent **F**ilter of ATLAS Trigger system
EFFS	**E**vent **F**ilter **F**ull **S**can
EM	**E**lectro**M**agnetic
EMB	**E**lectro**M**agnetic **B**arrel
EMEC	**E**lectro**M**agnetic **E**nd **C**aps
FCal	**F**orward **Cal**orimeter
GRL	**G**ood **R**un **L**ist
HB	**H**adronic **B**arrel
HEB	**H**adronic **E**xtended **B**arrel
HEC	**H**adronic **E**nd **C**ap
HERA	**Hadron**-**E**lectron **R**ing **A**ccelerator
HLT	**H**igh **L**evel **T**rigger
IP	**I**nteraction **P**oint
ISOLDE	Online Isotope Mass separator
JES	**J**et **E**nergy **S**cale
JER	**J**et **E**nergy **R**esolution

L1	**L**evel **1** of ATLAS Trigger system
L2	**L**evel **2** of ATLAS Trigger system
LB	**L**uminosity **B**lock
LHC	**L**arge **H**adron **C**ollider
LHCb	**L**arge **H**adron **C**ollider **b**eauty experiment
MB	**M**inimum **B**ias
MBTS	**M**inimum **B**ias **T**rigger **S**cintillator
MS	**M**uon **S**pectrometer
PDF	**P**arton **D**istribution **F**unction
nPDF	**n**uclear **P**arton **D**istribution **F**unction
QCD	**Q**uantum **C**hromo**D**ynamics
QGP	**Q**uark **G**luon **P**lasma
PDF	**P**arton **D**istribution **F**unction
ROB	**R**ead**o**ut **B**uffer
ROI	**R**egion **O**f **I**nterest
ROS	**R**ead**o**ut **S**ystem
RHIC	**R**elativistic **H**eavy **I**on **C**ollider
TDAQ	**T**rigger and **D**ata **A**c**Q**uisition system
TILECAL	**TILE Cal**orimeter
TRT	**T**ransition **R**adiation **T**racker
SM	**S**tandard **M**odel of Particle Physics
UE	**U**nderlying **E**vent